Czech Technical University in Prague

Faculty of Electrical Engineering

Doctoral Thesis

November 2023

Hana Šustková

Faculty of Electrical Engineering
Department of Microelectronics

Hana Šustková

Exploring the Potential of Quantum Simulation for Nanoscale Gas Sensing Development

Ph.D. programme: Electrical Engineering and Information Technology P2612
Branch of study: Electronic 2612V015
Supervisor: doc. RNDr. Jan Voves, CSc.

Doctoral thesis statement for obtaining the academic title of "Doctor", abbreviated to "Ph.D."

Prague 2023

The doctoral thesis was produced in combined manner

I dedicate this doctoral thesis to the most important people in my life: my beloved husband Ulf and our children. I thank you for being there and for your incredible patience with me during the long evenings in the Virtual NanoLab.

I wish to express my sincere gratitude to Dr. Jan Voves as well, my esteemed supervisor, for his guidance, mentorship, and expertise. Additionally, I am grateful for the support to balance my academic pursuits with raising our small children.

I extend my gratitude to the Czech Technical University in Prague with equal measure for the opportunity to study microelectronics and for the use of their modern software and experimental results that have made my research fundamentally possible.

This work was also supported by the Centre of the Advanced Applied Natural Sciences under Grant CZ.02.1.01/0.0/0.0/16_019/0000778 and by the Czech Technical University Student Grant No.SGS20/176/OHK3/3T/13.

Finally, I cannot thank Mrs. Cindy Austin enough for her invaluable assistance in reviewing and correcting my English, which has significantly improved the quality of this thesis.

I declare that I carried out this doctoral thesis independently, and only with the cited sources, literature and other professional sources. It has not been used to obtain another or the same degree.

In ..... date ....

Author's signature

Ph.D. study at the Department of Microelectronicsof the Faculty of Electrical Engineering of the CTU in Prague

Candidate: Hana Šustková
Department of Microelectronics
Faculty of Electrical Engineering of the CTU in Prague
Technická 2, 166 27 Prague 6

Supervisor: doc. RNDr. Jan Voves, CSc.
Department of Microelectronics
Faculty of Electrical Engineering of the CTU in Prague
Technická 2, 166 27 Prague 6

Anotace

Tato disertační práce představuje numerické atomistické modely struktur, konkrétně komponent pro detekci plynů, které využívají formalismus NEGF, tedy nerovnovážných Greenových funkcí. Výzkum se zaměřuje na různé materiály, jako jsou monokrystalické vrstvy oxidu zinečnatého, grafenové nanovrstvy a nanopásky a vícero molekul soli emeraldinu (polyanilin). Výsledky těchto modelů jsou porovnány s experimentálními údaji o detekci amoniaku, oxidu dusičitého a oxidu uhelnatého. Efektivní odpory $(R - R_0)/R_0$, vypočtené z I-V charakteristiky systému s adsorbovanými molekulami plynu a bez nich, pro více koncentrací plynu odpovídaly experimentálním výsledkům.

Bylo zjištěno, že nasimulovaná citlivost oxidu zinečnatého na amoniak je asi šestkrát nižší než při experimentu, což naznačuje, že citlivost může mít smíšený původ jen asi z jedné šestiny ovlivněné čistým monokrystalem ZnO.

Výsledky pro grafenové nanostruktury naznačují, že vodivost je spojena s poruchami, konkrétně s okrajem grafenové vrstvy. Vyšší odezva na poruchu byla pozorována u geometrie s řetězcem typu "armchair" než u geometrie typu "zig-zag". Nejvýraznější odezva na plyn byla pozorována u nejužšího nanopásku, kde se molekuly plynu usadily na okraji. Modelované senzory byly nejcitlivější na NO_2 a nejméně citlivé na CO.

Konečně jádro této práce, numerické zkoumání polyanilinu, dobře odpovídá naměřeným hodnotám. Polyanilin vykazuje dobré vlastnosti jako zařízení pro detekci plynů NH_3 a poměrně dobré pro detekci NO_2. Studie modelu polyanilinu kontaminovaného ionty kyseliny chlorovodíkové a kyseliny sírové ukázala, že přídavek ředidel zvyšuje odpor senzoru a způsobuje mírný pokles citlivosti, který je výraznější v případě kyseliny sírové. Na základě těchto zjištění je uvedeno doporučení pro výrobu plynových senzorů.

Klíčová slova:
sensor plynů, numerický model, polyanilin, oxid zinečnatý, grafén

Abstract

This thesis presents numerical models of atomistic devices, specifically gas sensing components, which employ the non-equilibrium Green's function formalism. The investigation focuses on various materials such as zinc oxide monocrystalline surfaces, graphene nanosheets, nanoribbon layers, and multiple molecules of emeraldine salt (polyaniline variety). The outcomes of these models are compared with experimental data of ammonia, nitrogen dioxide, and carbon monoxide detection. The effective resistances $(R - R_0)/R_0$, calculated from the I-V characteristic of the system with and without adsorbed gas molecules, for multiple gas concentrations corresponded with the experimental results.

It was found that the numerical zinc oxide sensibility to ammonia is about sixth times lower than in the experimentation, which suggests that the sensibility may have a mixed background of about one-sixth influenced by pure ZnO material (monocrystalline).

The results for graphene nanostructures indicate that the conductance is coupled with distortions, specifically the graphene layer edge. A higher response to disturbance was observed in the armchained geometry than in the zig-zag geometry. The most significant gas response was observed in the narrowest nanoribbon, where the gas molecules settled on the edge. The modeled sensors were most sensitive to NO_2 and the least sensitive to CO.

Finally, the core of this thesis, numerical polyaniline investigations, fit the measured values well and showed good properties as a gas sensor device for NH_3 detection and rather good for NO_2 detection. The study on the polyaniline model contaminated with hydrochloric acid and sulfuric acid ions revealed that the addition of dilutants increased the sensor's resistance, causing a slight decrease in sensitivity, which was more pronounced in the case of sulfuric acid. Based on these findings, a recommendation for gas sensor production is provided.

Keywords:
gas sensor, numerical model, polyaniline, zinc oxide, graphene

Contents

1. Introduction

This research focuses on numerically modeling the electrical properties of a select group of gas sensor materials, namely zinc oxide, graphene, and polyaniline (emeraldine salt variety). The research methodology will involve selecting an appropriate software tool, benchmark studies for these materials, and measuring I-V characteristics and resistance change. The main objective is to compare numerical results with experimental data to study these materials' prediction ability and sensing mechanisms. Ultimately, the goal is to identify the optimal conditions for physical experiments that will lead to the development of more effective gas sensors. This study aims to answer the question: How can numerical modeling contribute to developing modern gas sensors?

1.1 Motivation

Gas sensors are crucial in controlling environmental conditions, protecting human health, and ensuring product quality. They are essential in detecting hazardous substances like NH_3, CO_2, CO, NO_x, and SO_x groups. These sensors work by detecting the presence of targeted gases in the air and estimating their concentration. The device reacts to the chemical by changing its resistance, which can be measured and examined. There are several types of gas sensors, including optical, electrochemical, acoustic, capacitance, calorimetric-based, and others. Ammonia, NH_3, is a prevalent gas in industry and agriculture, and many sensors have been developed to detect it. However, detecting CO gas is difficult and dangerous, making it a focus of this study.

Recent advancements in physics have significantly expanded the range of materials used in gas sensors. Semiconductors, polymers, and 2D materials have opened new gas detection pathways. Solid-state sensing methods include metal oxide-based sensors like zinc oxide (ZnO), conducting polymers like polyaniline (PANI), and nanostructures like graphene structures. Optical methods utilizing diode laser spectroscopy, electrochemical methods, and acoustic or field effects are also used. Each method has its advantages and disadvantages, such as sensitivity, recovery time, stability, and price. However, an ideal sensor has yet to be found, and development is constantly progressing. Numerical models can help to understand sensing mechanisms, predict suitable materials or structures, and explain unexpected effects in experiments.

This thesis focuses on chemiresistive gas sensors, which can detect target gases in their environment and convert this information into an electrical signal (resistance change). The first chemiresistive gas sensor was presented in 1985 by Wohltjen et al. This sensor was a copper phthalocyanine device sensitive to ammonia. Due to their low production cost and ease of fabrication, chemiresistive sensors have received much attention. Today, there is a wide range of materials used for chemiresistive sensors, including semiconducting metal oxides (SMO), nanostructures (fibers, particles), and polymers [1]. This study aims to numerically model the electrical properties of a select group of gas sensor materials, including zinc oxide, graphene, and polyaniline (emeraldine salt variety). The research methodology will involve selecting an appropriate software tool, benchmark studies for these materials, measuring I-V characteristics and resistance change, and comparing numerical results with experimental data.

The present thesis focuses on the modeling of several promising gas sensor materials, namely:

- zinc oxide,
- graphene,
- and polyaniline.

These materials have been chosen due to their distinct basic properties, i.e., classical semiconductor, 2D-structure-semiconductor, and organic polymer. The study aims to comprehend the individual sensors' functionality through numerical analysis, evaluate their strengths and weaknesses, and predict their properties more accurately.

1.2 The current state of research in world literature

The topic of nanoscale gas sensors has been studied extensively since the 1990s [2], [3]. Polyaniline, zinc oxide, or graphene have been investigated for their potential use in detecting a wide range of gases, including NOx, CO, CO_2, and volatile organic compounds ($VOCs$) ([4], [5], [6]). Up today, the main attention was given to experimental studies of such sensors, including combination of these materials ([7], [8], [9], [10], [11]), but numerical approach has been studied as well ([12], [13], [14], [15]).

The main topic of this thesis is numerical study of gas sensor made of polyaniline (PANI). Research on this topic is currently very active in the experimental field ([16], [4]), here the latest research results also from the point of view of numerical modeling will be presented, of which there are significantly fewer.

In 2013, Ullah et al. ([13]) have evaluated the sensitivity and selectivity of polyaniline emeraldine salt as a sensor for NH_3, CO_2, and CO using density functional theory (DFT). The study found that PANI has greater response selectivity toward NH_3 compared to CO_2 and CO.

Then in 2018, Wei et al. ([17]) published strategy to fabricate Co_3O_4 hexagonal platelets and characterize the adsorption of ammonia using density functional theory as well. The plates exhibited high selectivity and sensitivity to NH_3 at room temperatures, with excellent reproducibility.

In 2019, Guo et al. ([18]) investigated the ammonia sensing mechanisms of polyaniline/graphene heterostructures through molecular dynamics. They revealed that graphene / PANI composites show higher sensitivity for detecting ammonia, with a larger band gap and a higher adsorption capacity. The large diffusion coefficient of ammonia in the polyaniline/graphene system should indicate easier gas diffusion.

Zhao et al. ([19]) published the same year a study demonstrating the high electrocatalytic sensitivity of polyaniline and metal carbides and nitrides (MXenes) nanocomposites, shortly as PANI/$Ti_3C_2T_x$, which was obtained using density functional theory simulations and bulk electrosensitive measurements. The synergistic properties of the nanocomposites and the high catalytic/absorption capacity of $Ti_3C_2T_x$ MXene should enable rapid detection sensitivity, rapid response/recovery rate, and mechanical stability at room temperature.

In 2021, Pang et al. ([20]) studied the properties of polyaniline (PANI) and aim gas in PANI-based gas sensors. They used molecular dynamics simulations to study the structural, morphological, and ammonia sensing properties of PA6/PANI nanofiber ammonia gas sensors. The sensors showed rapid response, ideal selectivity, and acceptable repeatability. The study also provided insights into the interaction between ammonia molecules and HCl-doped PANI chains.

Also in 2021, Korent et al. ([21]) presented new synthesis approach to create NH_3 PANI-based receptor elements. The PANI was electrochemically deposited on screen-printed electrodes (SPEs), and the morphology, composition, and surface were characterized. The PANI-Au-SPE gas-sensing ability was studied in the NH_3 range of 32–1100 parts per billion (ppb), showing good repeatability, reproducibility, and sensitivity.

Still in 2021, Liu et al. ([22]) studied PANI for NH_3 gas detection. A nanostructuralized PANI thin film was prepared using chemical oxidation polymerization and spinning coating. Etching via reactive ion etching increased the sensitive area and chemical diffusion pathway, introducing extra oxygen-containing functional groups to adsorb more NH_3 molecules. The nanostructuralized PANI sensor showed superior response, reproducibility, and selectivity to NH_3.

The same year, Scotland et al. ([23]) calculated band gaps of three forms of polyaniline using the DFT method. The calculations examined the effects of varying benzoid-quinoid structural units, increasing oligomer length, and incorporating Michael's addition structures (C-C bond formation processes include the nucleophilic addition of a carbanion or another nucleophile to an electron-withdrawing group-containing α,β -unsaturated carbonyl molecule, see [24]). The results were compared to the experimentally determined band gap of 1.5 eV. The Michael's addition structure was found to dominate the calculation.

In 2022, Oliveira et al. ([25]) published DFT study on the opto-electronic responses of Polyaniline (PANI) derivatives in relation to gaseous compounds revealed that side groups can modulate local reactivity and electronic properties, tuning their capability to detect chemical species. The study found higher reactivity on accessible side groups for PANI:
-C $\equiv$ CH, -C $\equiv$ N, and -NO_2, facilitating their interaction with analytes.

Also in 2022, Parangusan et al. ([26]) presented a new NH_3 gas sensor design made of PANI and two-dimensional transition-metal dichalcogenides (TMDs, mainly WS_2 and MoS_2). The composite material showed high sensitivity and response times, making it suitable for gas detection applications. The addition of MoS_2 and WS_2 decreased bandgap and improved structural, optical, and morphological properties.

Finally in 2023, Zhu et al. ([27]) focused on developing flexible gas sensors fabricated from multi-walled carbon nanotubes, grown on polydimethylsiloxane films and modified with polyaniline. The flexible sensor showed excellent NH_3 sensing performance, with a high response and low detection limit. The sensor also showed potential for monitoring NH_3 in human breath and food.

In this thesis, the topic of numerical modeling of sensors made of ZnO and graphene is further dealed. The latest research results in this area will now be presented.

In 2016, Hasanuddin et al. ([28]) studied a nondestructive fruit ripeness detection system using a finite element approach (software Comsol). They presented a 0.5 μm zinc oxide layer on a $LiNbO_3$ piezoelectric substrate for ethylene gas sensing, distinguishing fruit maturity levels and detecting ethylene gas release.

In 2018, Punetha et al. ([14]) presented a study on a zinc oxide thin film-based gas sensor, analyzing its conductance and sensitivity based on temperature and gas concentration changes. Simulation results were obtained by means of finite elements analysis (Comsol) applying adsorption theory and revealed changes in resistance and sensitivity with respect to temperature and different gas concentration.

In 2020, Arun et al. ([29]) developed a model of a meander-shaped micro-heater used for the ZnO sensor for acetone gas detection, with a spherical structure. Platinum was used as the heating material due to its high thermal conductivity and low power consumption. The temperature and resistance of the sensing layer are analyzed using finite elements (Comsol),

finding a decrease in resistance in Acetone gas presence.

In 2021, Marjunus et al. ([30]) simulated using their own mathematical approach sensor signal based on the ZnO for NO_2 gas detection, focusing on three reactions: adsorption-desorption of O_2, adsorption-desorption of NO_2, and the reaction of O_2 and NO_2 on ZnO. The simulation optimized 12 parameter values, but the final result still didn't perfectly fit the experiment results. However, it predicted coverage of O atoms, O_2 molecules, and NO_2 molecules.

In 2022, Chizhov et al. ([31]) examined the photostimulated processes of O_2 and NO_2 molecules with ZnO surface under UV radiation using in situ mass spectrometry. Synthesized nanocrystalline needle-like ZnO was characterized using various methods (SEM, Raman spectroscopy, etc.). Irradiation of samples with UV light caused the photoabsorption of both O_2 and NO_2. The photoadsorption properties of ZnO were compared with its defective structure and gas-sensitive properties to NO_2.

The same year investigated Lo Sciuto et al. ([32]) a chemiresistor sensor made of conductive polymer (regio-regular poly(3- hexyltiophene) and zinc oxide nanomaterial blend, testing its response characteristics, humidity, and temperature under nitrogen oxide exposure. An automated setup was used to interface the gas chamber with pipes, valves, and a mass flow controller. A 3D finite element model computed by Comsol was developed, observing rapid resistance changes during gas exposure.

Finally, Andre et al. ([33]) investigated in 2017 the combination of all three materials studied in this thesis - polyaniline, zinc oxide and graphene, and the developed highly sensitive and selective chemoresistive gas sensors. It exhibited high sensitivity and selectivity towards nitrogen dioxide gas. The sensor was able to detect NO_2 concentrations as low as 100 ppb and showed excellent stability and reproducibility.

1.3 Research Goals

The main research goals:

1. The analysis of the simulation models' ability to describe electrical characteristics of the resistive gas sensors based on the different nanostructures and detected gases.

2. The simulation results comparison with the experimental data for the suitable nanostructured material and the gas detected.

3. The model optimization for the selected sensor structure simulation and the sensing layer preparation process improvement.

1.4 Thesis Structure

The thesis begins with an overview of software tools, focusing on the Atomistic Toolkit (QuantumATK), chosen from a list of seven useful software tools. The chosen tool is then

introduced in detail, and its key features concerning the thesis are described precisely. The numerical background of the models depicted in this thesis is also introduced.

Following this, the materials zinc oxide, graphene, and polyaniline are thoroughly explained. The characteristics and important qualities of these materials are introduced, and the gases they interact with, including ammonia, nitrogen dioxide, and carbon oxide, are explained.

The core chapter of this thesis is gas sensor modeling, which involves detailed numerical simulation of zinc oxide, graphene, and polyaniline with the target gases mentioned above. The resulting data is then compared with physical experiments to answer the questions set by this work and discuss any discrepancies. This information can also help open new ways in numerical sensor modeling and the experimental preparation of sensing structures.

The main results of the thesis are then concluded in the last chapter. This includes the potential for future numerical sensor modeling and the experimental preparation of sensing structures. The research goals include understanding the targeted sensing mechanisms, improving physical experiments, and finding new paths for even better materials. The thesis also aims to improve the quality of sensors, especially those using polyaniline, and open the way for numerical modeling of similar gas sensor materials.

1.5 Outlook

After gaining numerical experiment data, looking for a match between the experiment and the numerical model is necessary. To look for clarity, if the numerical model can correctly encompass the desired sensor properties for a given material, it is furthermore possible to search for new paths for an even better material without the need for a laborious, often expensive experiment. Also, it is possible to discover where the key moments are in the case of an investigation, where to pay attention - for example, to the effect of material preparation on its detection quality, the choice of the working path, finding out what is important for a given material.

Based on known experiments, this thesis aims to help improve the preparation and quality of the sensors, especially the polyaniline (PANI) material used, and to open the way for numerical modeling for other similar gas sensor materials. It is worth noting that data displayed in this work were partially published in journals and conferences, as seen in the List of Author's Publications at the end of this thesis.

2. Software tools for nanostructure modeling

Foremost, this thesis presents an introduction to several software programs employed for nanostructure modeling. Nanostructure modeling refers to the computational determination of the positions and orbitals of atoms within arbitrary nanostructures, while the electronic structure is essential for comprehending material properties, including crystal structure, electrical resistivity, optical, or mechanical properties. Numerical techniques, namely Density Functional Theory (DFT), tight binding, or classical potentials, play a crucial role in this modeling process. As interest in this computational field continues to increase, the number of software applications developed for addressing physics or engineering issues also expands.

A short explanation will be given of software packages:

- QunatumATK (former Atomistix ToolKit)
- Quantum Dot Lab
- QuantumEspresso
- NEMO5
- SIESTA
- YASARA
- VASP

As the author of this text uses the software package QuantumATK [34] from Synopsys, the main interest will be held on this package; see this section's end.

2.1 Quantum Dot Lab

Quantum Dot Lab [35] is an education tool computing the eigenstates of a particle in a box. This software is available under a nanoHUB license for online simulation and was created by G. Klimeck, L. Bjaalie, S. Steiger, D. Ebert, T. C. Kubis, M. Mannino, M. McLennan, H.-H. Park, and M. Povolotsky.

The Quantum Dot Lab runs on a single- or two-band effective mass model and a ten-band sp3d5s* tight-binding model (with spin-orbit coupling). As an output, a 3-D visualization of the 7 3-D confined wave functions are generated; optical transitions and absorption curves are computed. Absorption curves are available for different polarizations and orientations. Parameters such as incident light angle and polarization, Fermi level, or temperature can be included to study the isotropic optical properties of the 3-D model. The simulation runs parallelized. The underlying engine for Quantum Dot Lab is NEMO 5 (see next chapters), software developed in the research group of G. Klimeck. This software is an open-source nanoelectronics device simulator can construct atomistic grids of varying crystal structures and compute multiband Schroedinger-Poisson problems. More about NEMO 5 in a separate paragraph.

2.2 QuantumEspresso

QuantumEspresso [36], in short QE, is a code for electronic-structure calculations and nanoscale materials modeling. Numerically, a density-functional theory, plane waves, and pseudopotentials are used. This software is Open-source, developed by many scientific groups, and managed by Quantum ESPRESSO Foundation.

QE is suitable for ground-state calculations, structural optimization, computation of transition states, molecular dynamics (ab initio), quantum transport, spectroscopical computations, or response properties. As for ground-state calculations, QE offers self-consistent total energies, forces, stresses computations, spin-orbit coupling, non-collinear magnetism, PAW (Projector Augmented Waves) method, DFT with Hubbard potential method, DFT with VdW corrections (nonlocal as well), computation of exchange-correlation functionals – LDA, generalized-gradient corrections, meta- GGA, exact exchange (HF), and hybrid functionals. For response properties calculation, the density- functional perturbation theory is used and can deliver phonon frequencies and eigenvectors at any wavevector, full phonon dispersions or inter-atomic force constants in real space, effective charges and dielectric tensors, further electron-phonon interactions, or infrared and Raman cross-sections. The software can be run on GPU via the QE-GPU add-on package.

2.3 NEMO5

NanoElectronics MOdeling Tools [37], called NEMO, in its 5th edition (NEMO-1D, NEMO-3D, NEMO-3D-Peta, OMEN, now NEMO5). This software package computes crystal structures, phonons and strain, electronic structure, and transport properties. The software was developed by the Klimeck group is available for educational use with free and commercial restrictions. NEMO5 is also distributed per nanoHUB.

NEMO5 offers atomic-resolution calculation of nanostructure properties, whose are electronic structures based on the tight-binding model, strain relaxation, phonon modes, self-consistent Schroedinger-Poisson calculations and quantum transport. Software is parallelizable per MPI. As for band structure computation, NEMO5 solves the Schrödinger equation for crystal structures: Zincblende, simple-cubic, wurtzite, trigonal, and graphene. The software computes with the orthogonal tight-binding model in the two-center approximation and can solve the Schrödinger equation in the effective mass approximation. The tight-binding models can include/exclude spin-orbit interaction, has strain effects on the electronic band structure, and offers passivation of the surfaces with hydrogen, avoiding producing dangling bonds in the center of the bandgap for semiconductor nanodevices.

Used tight-binding models are:

- s-band model, as an effective mass in a simple cubic crystal
- standard tight-binding models sp^3-, sp^3s^*- and $sp^3s^*d^5$
- $sp^3s^*d^5f^7$-model, e.g., for Lanthanides and Actinides
- pz-model usable, e.g., for Graphene
- p/d-model, a new model for advanced Graphene calculations

Nextly, the software NEMO5 supports the self-consistent solution of the Schrödinger and the Poisson equation. According to Schottky barriers and Ohmic leads, boundary conditions

can be set as Dirichlet and Neumann types. The charge density can be calculated from the Schrödinger equation or a semiclassical model.

NanoHUB projects like 1Dhetero or Quantum Dot Lab are using NEMO5. About Quantum Dot Lab, a separate paragraph was written in this text. About 1Dhetero, this program designs and simulates 1D heterostructures and explicitly calculates a self-consistent electron density and electrostatic potential solution. Numerical methods used are density models like semiclassical density, 1-band effective mass model or 10- and 20-band tight-binding models. 1Dhetero is a closed source.

2.4 SIESTA

SIESTA [38] states for Spanish Initiative for Electronic Simulations with Thousands of Atoms, and it is a method for computing electronic structure and ab initio molecular dynamics simulations of molecules and solids. SIESTA uses a density functional theory code and can compute Kohn–Sham band structures, electron density, and Mulliken populations. The accuracy and cost of the computation can be tuned in a wide range, from quick exploratory calculations to highly accurate simulations.

SIESTA is open-source and was developed by J. M. Soler, E. Artacho,J. D. Gale, A. García, J. Junquera, P. Ordejón, and D. Sánchez- Portal. SIESTA can study total and partial energies, atomic forces, stress tensors, electric dipole moment or atomic, orbital, and bond populations (Mulliken populations). Further, this software computes electron density, geometry relaxation for fixed or variable cells, constant-temperature molecular dynamics or variable cell dynamics, collinear/non-collinear spin-polarized models, k-sampling of the Brillouin zone, the local and orbital-projected density of states, dielectric polarization, then vibrations (phonons), and finally, band structure.

SIESTA is based on the standard Kohn-Sham self-consistent density functional method in the local density (LDA-LSD) or generalized gradient (GGA) approximations, recently with functional including van der Waals interactions. This software makes it possible to compute norm-conserving pseudopotentials in their fully nonlocal (Kleinman-Bylander) form. SIESTA calculates the Hamiltonian and overlap matrices based on the finite-support basis set for atomic orbitals. Nextly, SIESTA can compute the Hartree and exchange-correlation potentials, which is done by the electron wavefunctions and density computation onto a real-space grid. SIESTA is also available as a parallel program for MPI.

2.5 VASP

Vienna Ab initio Simulation Package [39], in short VASP, is a software designed for atomic-scale materials modeling – electronic structure calculations and quantum-mechanical molecular dynamics. This commercial software was developed by the University of Vienna, Austria, represented by Prof. Dr. G. Kresse.

The numerical method of VASP are DFT, Kohn-Sham equations, Hartree-Fock approximation, Roothaan equations or hybrid functionals co-using the Hartree-Fock approach with density functional theory, then Green's functions methods (GW quasiparticles and ACFDT-RPA) and many-body perturbation theory (2nd-order Møller-Plesset). VASP can compute LDA, GGAs, metaGGAs, Hartree-Fock, and Hartree-Fock/DFT hybrid functionals.

This software can be used for the study of dynamics and relaxation through the Born-Oppenheimer molecular dynamics, conjugate gradient, Quasi-Newton or damped molecular

dynamics, nudged elastic band methods, and climbing dimer method. VASP can study the magnetism of collinear and non-collinear systems, with spin-orbit coupling and others, and use a constrained magnetic moments approach. As for the linear response to electric fields, in VASP, a study of static dielectric properties, computing of Born effective charge tensors or piezoelectric tensors (including ionic contributions) is possible. Further, the study of phonons, calculating elastic constants (including ionic contributions), and internal strain tensors are supported. As for optical properties of the system, frequency-dependent dielectric tensors can be studied in the independent particle approximation, further frequency-dependent tensors by the RPA and TD-DFT method and Cassida's equation for TD-DFT and TD-Hartree-Fock methods. VASP can compute macroscopic polarization and finite electric fields as well.

In VASP software, a plane wave basis set is used to describe central quantities, like the one-electron orbitals, the electronic charge density, and the local potential. PAW method, norm-conserving, or ultrasoft pseudopotentials are used for electron-electron interactions. VASP can run in parallel mode.

2.6 YASARA

Yet Another Scientific Artificial Reality Application [40], in short YASARA, is a software dedicated to molecular graphics, modeling, and simulation. The basic version, YASARA View, is free, while higher stages (YASARA Model, YASARA Dynamics, YASARA Structure) are commercial software. Company YASARA Biosciences developed YASARA.

This software is delivered in versions called YASARA View (molecular graphics and analysis), YASARA Model (plus molecular modeling), YASARA Dynamics (plus molecular simulations), YASARA Structure (plus structure prediction and validation), YASARA NMR Module (NMR structure determination).

YASARA is parallelizable. It computes long-range electrostatic interactions with the Particle Mesh Ewald (PME) approach calculates energies, binding energies, and solvation energies using Poisson- Boltzmann or PME methods estimate the electrostatic potential using Poisson-Boltzmann or PME methods. YASARA can calculate semi-empirical quantum mechanical point charges using either AM1BCC or AutoSMILES and optimize the geometry with semi-empirical MNDO/AM1/PM3 quantum-chemistry using a customized MOPAC package. Finally, YASARA can analyze trajectories for conformational changes, calculate time averages, RMSDs, RMSFs, RDFs, and dynamic cross- correlation matrices.

2.7 QuantumATK

The essential software solution for this study is QuantumATK (Atomistix ToolKit) [34]. QuantumATK, in short ATK, is a commercial program for the simulation and modeling of nanostructures at the atomic scale, provided by Synopsys. As this software's website, thanks to its graphical user interface, ATK is also a tool for teaching basic concepts of nanotechnology, solid-state physics, and others.

ATK provides atomic-scale modeling tools which can handle classical force fields for large systems as well as ab initio tools for gaining highly accurate results for small systems. The main features of this software package are: the possibility of non-equilibrium Green's function (NEGF) simulations, which enables the study of transport properties (e.g., I-V characteristics of nanoelectronic devices), a combination of DFT, semi-empirical tight-binding (extended H

"uckel, DFTB, Slater-Koster), and classical potentials as a numerical method. This software can be used to calculate electronic structures, compute transport properties of nanoscale devices (through NEGF formulation), and calculate molecular dynamics. So the software is suitable for studying the electronic, magnetic, optical, mechanical, thermal, transport, and other properties of designed nanostructures.

ATK has its own GUI – called NanoLab - for building nanostructures to be studied, like interfaces and transport systems. Next, ATK supports implementing Python for scripting and interface with plugin-possibility for external codes: ATK can interact, for example, with VASP, ABINIT, or QuantumEspresso, users can develop their plugins, too. What is interesting about the ATK software package is the support of MPI parallelization, based on MPICH2, and OpenMP threading support by using Intel Math Kernel Library (MKL).

2.7.1 Computation ability

ATK offers computation of many physical quantities concerned with electronic structure. With ATK, calculating molecular spectra, band structure, or an effective mass analysis is possible. ATK can compute the density of states for the user-defined system, and this with projection onto atoms and angular momenta, then eigenfunctions like molecular orbitals or Bloch functions, forces and stress, total energy or polarization, and piezoelectric tensor. In 3D real space, ATK offers the possibility to compute and render orbitals, electron density, electron localization function, and proprietary effective, electrostatic, or exchange- correlation potential.

In ATK software, a computation of optical properties is possible as well. Supported are the estimation of linear optical properties using Kubo-Greenwood formalism, calculation of optical absorption, dielectric function, or refractive index. ATK fully supports ballistic coherent elastic tunneling transport analysis from electron transport analysis and can compute transmission spectrum (or related quantities). For example, the transmission coefficients for the probes, differential conductance, current and current densities or transmission eigenvalues, and eigenchannels and pathways. The density of states with projections on atoms and orbitals is also available for devices. The ATK software can compute the next thermionic emission's voltage drop or transistor characteristics. In ATK, molecular projected self-consistent Hamiltonian (MPSH) eigenvalues, the local density of states (LDOS – real-space projected), and complex band structure can be computed. As the following functionality of ATK, computation of ion dynamics is supported. It involves calculation of the dynamical matrix, phonon band structure, density of states, and thermal transport, further forces and stress computation using Quasi-Newton and FIRE methods or transition states, reaction pathways, and energies using nudged elastic bands (NEB) method. Finally, ATK supports molecular dynamics computation. Numerical methods like DFT, semi-empirical models, or classical potentials are used (see below). Through the software ATK, a stress-strain curve can be obtained.

2.7.2 Numerical methods

ATK offers more numerical methods suitable for various problems.

Methods for computing the electronic structure:

- LCAO-based density-functional theory (DFT) method

  This method includes numerical atomic orbital basis sets with controllable parameters, then indirect atom pairs or norm-conserving pseudopotentials of the Troullier-Martins

type. In the software, customized pseudopotentials are possible to select. ATK offers over 300 exchange-correlation functionals computed by LDA, GGA, and extra for Meta-GGA, for accurate band gaps of semiconductors. In both the LDA and GGA method, Hubbard corrected potential term can be calculated (LDA+U/GGA+U). The software package can also work with one van der Waals model, specifically the DFT-D2 method of Grimme. Non-collinear, restricted, and spin-polarized calculations can also be performed for molecules, bulk, or devices. For the computation, the user can define the initial orbital occupation.

- Plane-wave DFT method

  A parallel version of the software ABINIT is used for the plane-wave DFT method. This part is fully integrated into the ATK system.

- Semi-empirical tight-binding method

  For this method, a DFTB-type model with predefined parameter sets is available. Custom Slater-Koster parameters are natively supported. ATK has built-in models for group IV semiconductors and III-V binary alloys available. One can use an extended H "uckel model or Müller and Hoffmann model for molecular calculation. The software includes an additional Hartree term for the self-consistent response to the electrostatic environment and further support for model adaptation for self-consistent calculations.

- Classical potentials

  The EMT, Brenner, and Tersoff potentials are available for this method. In general, the system calls new calculations via the self-consistent density matrix of a converged one; further, a Kerker preconditioner is used. ATK disposes of a sparse matrix library for quick computation, complemented by Fermi-level smearing, achieving better convergence stability. Monkhorst-Pack k-point sampling grids and Brillouin zone symmetries are used in dual space.

Method for transport calculations:

- Extended TranSIESTA-based method

  This method bases on the self-energy coupling to semi-infinite leads and is used for two-probe systems. For this method, open boundary conditions are prescribed. For density or matrix elements, all spill-in contributions are enhanced. If the system is open, a fast contour integration by the scattering states method can be applied, and electric free energy is used (casually, the total energy is used).

- Non-equilibrium Green's function (NEGF)

  The electron distribution in the scattering region can be in ATK described by NEGF. In central the region, Green's function is prescribed.

- Recursion method, direct method, Krylov subspace method

  These methods apply to self-energy calculations.

- Scattering states method

  For fast contour integration in non-equilibrium, ATK offers a scattering states method as well.

- Surface Green's Function

  Surfaces are modeled beyond the slab approximation, and electrochemical reactions and surface states are computed. The Hamiltonian of the system is described through DFT-LCAO or the SemiEmpirical methods.

- ForceField

  For atomic-scale simulations (molecular dynamics and others), this technique uses classical potentials - bonded and reactive force fields, pair potentials, and other parameterized interaction models for atoms.

In general, ATK can treat systems with a different electrode material, geometry, spin, et cetera, and can perform fast transmission spectrum calculations in perfect periodic systems.

Methods for electrostatic models:

- Multi-grid or FFT

  ATK looks for a solution to the Poisson equation by multi-grid or Fast Fourier Transformation method, applying Dirichlet, von Neumann, or periodic boundary conditions. The system can be specified independently in each direction so that the model is as realistic as possible. Another method to solve the Poisson equation for transport is called FFT2D and concerns multi-grid in the transport direction and FFT in the transverse plane.

ATK can compute metallic gate electrodes and show dielectric screening regions, which allows the user to calculate gated structure as a transistor, further charge stability diagrams of a single-electron transistor, and others for more regions at user-specified positions. In ATK, a simulation of external fields can be achieved by the local atomic shift method. A doped system can also be calculated, utilizing charged systems with compensation charges.

NanoLab

ATK is delivered with its graphical user interface (GUI), containing many functionalities. This GUI is called NanoLab and consists of more parts. NanoLab allows users to build atomistic structures like nanotubes, graphene ribbons, and others, and generate Python input scripts for ATK (or write down their own), start and launch calculations, and post-process them. These functions are divided each to its underapplication: 3D Viewer (geometry visualization), Builder (molecules, periodic structure or transport systems from scratch, building), Script Generator (set up of the entire quantum-chemical model), nextly, Custom Builder (custom geometry generator as a Python script), Custom Analyzer (custom scripts to manipulate and visualize 2D data computed by ATK), Custom Scripter (creation of input files for external codes), then Database (thousands of structures for use in a calculation or as a template for a more complex geometry), Script Editor (transfer of scripts to any other instrument in VNL), important is Job Manager (launching of calculations directly from VNL), and VNL General (post-processing, 2D plotting of band structure, molecular spectra, DOS, et cetera).

2.8 QuantumATK for modeling of the sensing structures

Computation in this thesis was done by Synopsis QuantumATK (ver. 2018.06, later 2020.09) and using a benchmark, for polyaniline and graphene molecules using semi-empirical tight-binding methods, for ZnO within density functional theory (DFT), both using numerical LCAO basis sets (linear combination of atomic orbitals). From the semi-empirical tight-binding methods for PANI and graphene, the Extended Hückel Method [41] was chosen. Device systems and their I-V characteristics were then computed using non-equilibrium Green's functions formalism (NEGF), used in the Extended Hückel Method as well [34].

Extended Hückel method is based on the Hückel method but considering not only π-orbitals but also σ-orbitals. In this method, the electron-electron repulsions are not included explicitly; the total energy comes from the sum of every electron in the molecule [41].

As for the Extended Hückel Method used for bulk and molecule, the self-consistent and non-self-consistent part of the tight-binding Hamiltonian is characterized. The real-space electron density is determined from the density matrix gained from the self-consistent part computation, and from that, the Hartree potential is calculated - through Fast Fourier Transform (FFT) from the Poisson equation. The density matrix is calculated by diagonalizing the Hamiltonian [41].

The non-self-consistent part uses two-center approximation - the matrix depends only on the distance between two atoms (their overlap between Slater orbitals for both sites), while the distances of the other atoms do not influence them. The non-self-consistent part of Hamiltonian is expanded based on local atomic orbitals (LCAO) in spherical harmonics Y_{lm} and radial function R_{nl} [41]:

$$\psi_{nlm}(r) = R_{nl}(r)Y_{lm}(\hat{r}). \tag{2.1}$$

The Density functional theory method describes the many-body electronic structure of the system utilizing terms of the one-electron Kohn–Sham Hamiltonian [34]:

$$\hat{H}_{1el} = -\frac{\hbar^2}{2m}\nabla^2 + V_{eff}[n](r), \tag{2.2}$$

That means the sum of its kinetic energy and the effective potential - the potential energy of this electron, while moving in the mean field of the other electrons, described in terms of the total electron density, n=n(r), and all of them in any potential of external field (the electrostatic potential of ions, and others). The wave functions are covered by numerical LCAO basis sets, which state the expansion of the single-particle wave functions based on atomic orbitals.

For both approaches, semi-empirical and LCAO, the device system gains the density matrix using NEGF, as already mentioned. NEGF is also used for the transmission, thus for the I-V characteristics [34].

The occupied eigenstates of the Kohn calculate the electron density–Sham Hamiltonian, using the occupation f_α of the level α (Fermi-Dirac distribution) [34]:

$$n(r) = \sum_\alpha f_\alpha |\psi_\alpha(r)|^2 \tag{2.3}$$

This density is, for calculation purposes, divided into a "left" and a "right" contribution, defined in the model by cartesian coordinates, where z-axis states for the distance between

electrodes and direction z to $-\infty$ is defined as "left" while direction z to $+\infty$ as "right". Using the NEFG method, the left and right density matrix contributions are calculated [42]:

$$D^{left} = \int \rho^{left}(\epsilon) f(\frac{\epsilon - \mu_L}{k_B T_L}) d\epsilon \tag{2.4}$$

For the left contribution and, accordingly, for the right contribution. The Fermi function f ruled by the electron temperature T_L states for the electron distribution in the left (right) electrode, while the non-equilibrium electron distribution governs the central region. The function $\rho(\epsilon)$ is the spectral density matrix using the retarded Green's function G and broadening function Γ and is defined as [42]

$$\rho^{left}(\epsilon) = \frac{1}{2\pi} G(\epsilon) \Gamma^{left}(\epsilon) G^{\dagger}(\epsilon) \tag{2.5}$$

for Green's function and broadening function

$$G(\epsilon) = \frac{1}{(\epsilon + i\delta_+)S - H} \tag{2.6}$$

$$\Gamma^{left} = \frac{1}{i}(\Sigma^{left} - (\Sigma^{left})^{\dagger}) \tag{2.7}$$

using infinitesimal positive number δ_+, the Hamiltonian matrix H, and overlap matrix S, both the entire system and the left/right electrode self-energy Σ [42].

Finally, knowing the retarded Green's and broadening function for both electrodes, the transmission spectrum is computed as [42]

$$T(\epsilon) = G(\epsilon) \Gamma^{left}(\epsilon) G^{\dagger}(\epsilon) \Gamma^{right}(\epsilon) \tag{2.8}$$

There are no modeled metal contacts in the simulation of PANI or graphene. There are only polyaniline/graphene chain parts without perturbative potentials called in the QuantumATK software as the electrodes (they consist of polyaniline or graphene chain, respectively, without perturbation, benchmarked as a particular case). The boundary conditions are fully periodic for the electrode areas, computing them as bulk material. There are so-called electrode-extension areas between the electrode areas and the central part with the perturbation (for example, the ammonia gas molecule). These areas screen out the perturbation of the scattering region, such that the outermost part of the central region nearest the effective potential is similar to the bulk potential of the electrodes. As described here, this model relies on the so-called screening approximation: the properties of the left and right regions, in this software called the electrodes, can be characterized by solving a bulk problem for the fully periodic electrode cell. When the current through the system is small enough, the screening approximation will be held, and the electrode regions can be described by an equilibrium electron distribution [34].

3. Materials for sensor applications

Using numerical simulation in QuantumATK, the following materials were studied: zinc oxide, graphene, and polyaniline. All of these materials are promising in their ability to sense certain gases such as ammonia (NH_3), nitrogen dioxide (NO_2), carbon monoxide (CO), and others. Kwak et al. [43] published in 2019 a comprehensive overview of ammonia gas sensing materials including their key features like detection limit, response and recovery time, and operation temperature - experimental data. In that article, we can find all of the materials of our interest and their mixtures ($PANI$, $ZnO/PANI$, $PANI/graphene$, etc.) because their mixtures bring faster response or higher sensitivity in comparison to pure materials. Each of these materials has different gas-sensing properties coming from their different physical nature.

3.1 Zinc Oxide

Firstly, a promising pure metal oxide material for gas sensing may be zinc oxide. This material can act as a UV photodetector or in light-emitting diode, solar cells, or varistors, nextly, can be used in piezoelectric or surface acoustic wave devices. This n-type semiconductor can be used as a catalyst because of its extraordinary electrical, optical, and catalytic properties [5]. It has also high chemical and thermal stability, nextly, a wide band gap (3.00 eV–3.24 eV), its structure can be improved and it has interesting optical, electrical, and electronic properties. On the other hand, its difficulties include: the high working temperature of over 200 $°C$ (usually 300 to 500 $°C$), poor selectivity, and relatively low response [43]. To overcome these drawbacks, innovative geometries are proposed: thin-film, nanofibre, quantum-dot, or composite sensors, which may show better properties [44].

ZnO Gas sensing mechanism

Zinc oxide sensitivity is based on the grain boundary effect by varying electron depleted zone [8]. While ZnO can crystalline in many structures, let's assume the common Wurtzite structure. ZnO layers in hexagonal lattice involve two Zn^{2+} and O^{2-} hexagonal-close-packed (hcp) sub-lattices. Because of either one or another ion on the surface in the c-direction, these surfaces of the crystal grains are polar (also not stable). Therefore, these surfaces allow the adsorption of molecular or atomic oxygen which creates an electron-depleted zone - a depleted layer of appropriate thickness. Through this adsorption, the surface potential barrier height and surface charge are affected by the increase of depletion zone thickness, represented by Debye length.

While a gas molecule is resorbed into the structure, it may donate the resorbed oxygen and so alter the barrier height, the depleted layer, and consequently the electric resistance will change. Therefore, the eigen Debye length affects the gas sensitivity and selectivity; it means the ZnO gas sensor performance grows with a higher extent of oxygen vacancies and it is dependent on the crystal facilities - size, morphology, and layering.

The ZnO gas sensors were found to be selective toward NO_2, H_2S, or NH_3 gases [45].

3.2 Graphene

The next rather new gas sensor material is graphene, a variety of carbon discovered in 2004, characterized by a two-dimensional honeycomb-like structure, a single layer originating from the three-dimensional structure of graphite, concatenation of benzene rings in 2D. The sheet edge is passivated by another atomic group like hydrogen and this influences the graphene properties. This zero-gap, exposed to the air-building p-type, semiconductor is characterized by linear dispersion at Dirac points (six locations in momentum space) implying that the physical properties of pure graphene are rather unusual. This one carbon atom thick material has very high electrical current density and intrinsic mobility (electrons occupying these straight band feel to have zero mass) [46] and it is possible to turn it into a superconductor. Graphene is a very good isotropic thermal conductor and has a very high tensile strength ($>$ 1 Tpa) [47] and is very stretchable (up to 20 % of its initial length). Graphene is impermeable even for helium molecules, it is an inert material but can "absorb" different atoms and molecules. This can lead to changes in the electronic properties, and may also be used to make sensors or other applications.

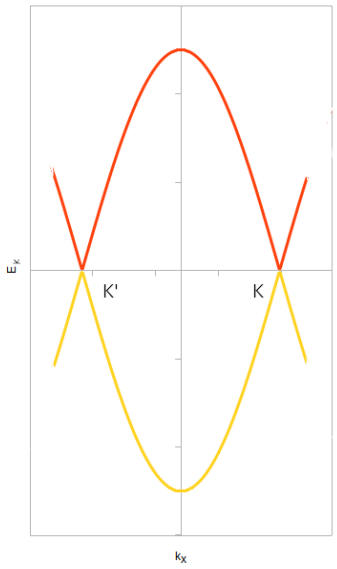

Figure 3.1: Valence and conductance band of graphene, at K, K' - Dirac points

While searching for suitable material for gas sensing, graphene seems also to be promising: from the characteristics above, large surface in comparison to volume, high carrier mobility, and adaptation of sensor physical properties based on the substrate or the presence of other chemical compounds, adapting the material for target gas are crucial properties for usable gas sensor. Nextly, graphene has a low environmental impact, is non-toxic, and is well preparable - concluding, this material can be interesting for real production as well. Its band structure described above is very sensitive to Fermi-level changes as well. This can be used to tune its conductivity and sensor usage; through doping or, when used as a field effect transistor (FET), by a back gate voltage [48].

Graphene sensing mechanism

Because of the 2D structure, graphene sensors can be prepared in several ways; as mass sensitive, chemiresistive, field-effect transistor (FET), and Schottky/heterojunction diode sensor [48]. For this text, let's assume the chemiresistive graphene sensor.

Under some circumstances, graphene can be considered a p-type semiconductor, characterized by many holes - this p-doping of graphene is caused by air exposure. The Fermi level energy sinks under the Dirac point energy and the holes are current charge carriers. Exposure of the sample to the measured gas can cause electron donation (i.e. by ammonia), or acceptation (i.e. by nitrogen dioxide) influencing thus the hole statistics. Electron donors lower the free charge carriers amount, turning the sensor into a more resistive one. On the opposite, the electron acceptor greater the hole amount which leads to better conductivity [49].

Wide attention to graphene as a sensor has been already made - today, the detection of various types of gases was demonstrated: NH_3, NO_2, CO, H_2S, H_2,O_2, CH_4, SO_2, etc. In 2007, Schedin et al. [50] detected a single NO_2 molecule, later, sensors with a limit under 500 parts-per-billion (ppb) for NO_2 and NH_3 were fabricated. But these promising results are hard to achieve in commercial life, because of material and environmental conditions. For example, clean graphene sensors need to be heated at 200 $°C$ in inert gases, they do not respond to NH_3 at room temperature at all [48]. Graphene ammonia sensor calculations were made as well [51], showing that gas molecules are attracted by the graphene defects and the graphene sensor response is driven by the dispersion velocity of these traveling molecules. Although some experiments may show that also pristine graphene may sense gas molecules [52], other results showed the opposite facility - the more defects, the better results (graphene irradiated by UV, warmed up, etc.). In this work, this topic will be studied.

3.3 Polyaniline

In this work, as the main theme, also macromolecular material polyaniline was chosen as an adept for gas sensors. In recent research, macromolecular material polyaniline (PANI), belonging to the class of current-conducting polymers, being used for energy storage devices or conductive adhesives, inks, polymer light-emitting diodes, and solar cells or capacitors [53], was studied for gas sensors applications as well [54], [55]. The choice of PANI for gas sensing comes from its low production and operation costs (can work on low voltage and current), good availability, and ecology - it is not a mixed material with recycling problems at the sensor life end. It is also a lightweight and flexible material with a large surface-to-volume ratio. PANI is likely long-term stable sensor material as well (remaining its properties for thousands of voltage cycles [56]). The stability of the sensor can be significantly improved especially by crosslinking its structure [57] or using a virtually unlimited spectrum of PANI-compounds and forms (PANI-TiO_2 nanocomposites [58], PANI-graphene nano-dots [59], SnO2/rGO/PANI nanocomposite [60] etc.), which can lead not only to stopping the degradation of the material, they can open a new sensor selectivity to target gases and tune their sensitivity.

For sensory usage, its electrical conductance source - caused by the π-conjugated bonds in aniline rings and NH-groups is important [61].

For gas sensor research, the emeraldine salt, a variation of PANI, is in focus. Polyaniline can namely exist in three ground oxidation states, and varieties, with very different electrical properties.

The fully reduced PANI variety, leucoemeraldin, is a transparent polymer, and namely an electrical insulator, like the other PANI variety, the partially oxidized blue polymer emeraldine (in the base form). Next, the fully oxidized, semi-conducting violet variety of PANI is called pernigraniline. Putting a defect into the chain of insulating/low conducting PANI, one or more polarons may appear. Thus through proton doping (of emeraldine base) or electron reducing (of leucoemeraldine base) of every second nitrogen atom - there will appear two polarons per one 4-benzene-unit - the green emeraldine salt can be produced from emeraldine base or leucoemeraldine base, reaching a conductivity of 400 S/m [62]. The properties of PANI are dependent on the way of polymerization as well [8], [63].

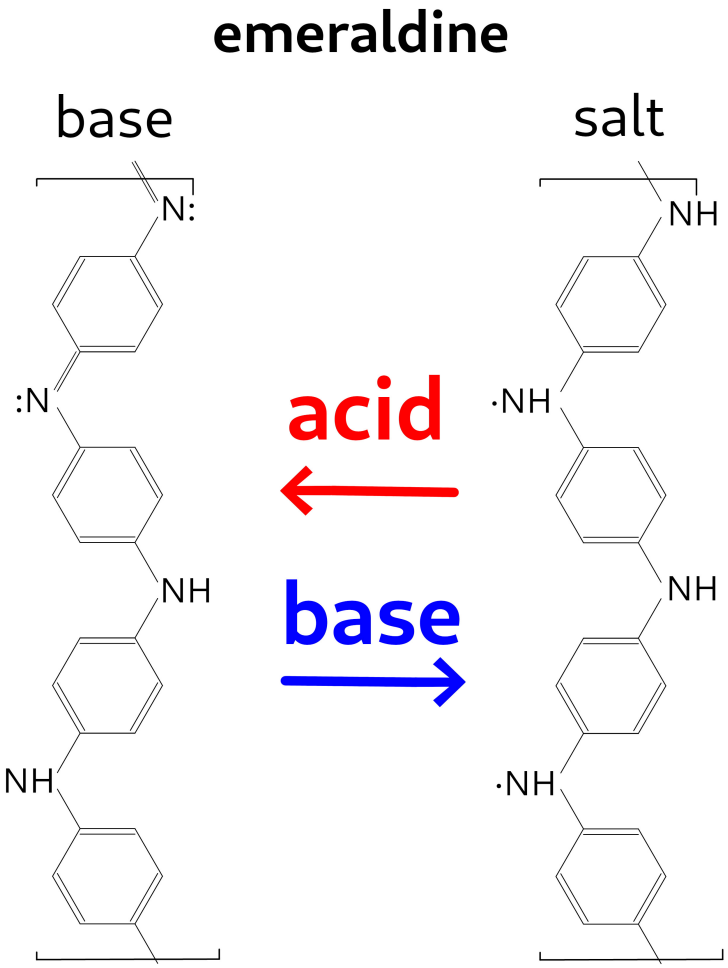

Figure 3.2: Polyaniline varieties emeraldine base and emeraldine salt.

PANI can be prepared either chemically or electrochemically, in many variations and with different electrical properties [64].

PANI gas sensing mechanism

According to previous research, the PANI in the form of emeraldine salt may react with a group of gas molecules, among others with NH_3 or NO_2 [65]. Let's describe the gas-sensing mechanism for ammonia molecules. When ammonia interacts with the PANI chain, a de-doping effect (acid-base reaction) occurs. The gas molecule will occupy one proton of doped

nitrogen atom from the PANI chain (bond as NH^+), building a NH_4^+ state and removing the polaron from the PANI chain. The PANI chain loses a significant amount of charge carriers, and its resistance rises. The increase in resistance depends on the number of doped nitrogen atoms in the chain and on the ability of ammonia gas to penetrate the PANI structure. But the resistance change is reversible. When the undoped PANI chain is exposed to air again, the ammonia gas molecule is desorbed, and the nitrogen atoms gain their proton back. For given ammonia concentration in air, the ammonia gas molecule adsorption and desorption from PANI lead to resistance changes [66]. Recently, experiments with flexible ammonia gas sensors based on polyaniline have shown such resistance changes as well [67].

In [68], the polyaniline gas sensor set-up was measured experimentally for several gases, including NH_3 and NO_2. In comparison to other gases, polyaniline should be especially sensitive to ammonia gas. The molecular and electronic properties of different forms of polyaniline were analyzed using quantum mechanical calculations in [62], [69]. Reis et al. [70] calculated band structure, charge density, transmittance, and electrical current of polyaniline using the Density Functional Theory (DFT), with the generalized gradient approximation (CGA) of Perdew–Burke–Ernzerhof (PBE), for the exchange-correlation energy. The adsorption energy of NH_3, NO, CO, and H_2 on graphene/PANI was recently investigated by DFT and molecular dynamics simulations [65]. Based on the obtained increase of the DOS above the Fermi level graphene/PANI they endorsed much higher sensitivity towards NH_3 gas than for the other three gases.

4. Gas sensor modeling

4.1 Zinc Oxide

Sensor based on a crystalline material is certainly the first choice regarding structure, stability, and repeatability. However, the long-interesting material ZnO holds many secrets, and although everyday electrical components such as varistors are based on it, the physical mechanisms that lead to its use are less obvious than one might assume.

This work aims to answer the question: Can a simplified numerical model of a small monocrystalline piece of zinc oxide give relevant data comparable with a real ZnO gas sensor? Alternatively, can such a model help to understand some part of the complex nature of this material?

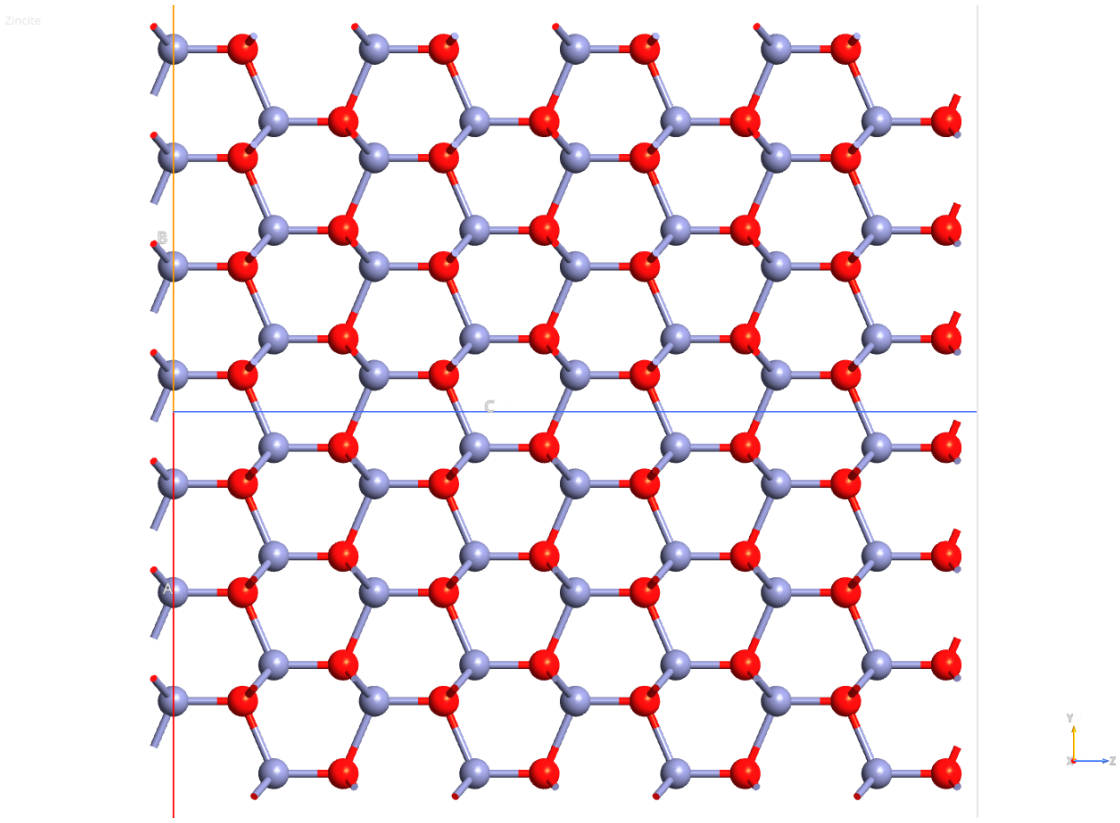

Figure 4.1: ZnO - Wurzite

To find answers to these questions, the first step for numerical studying a zinc oxide gas sensor is benchmark and numerical method choice. ZnO is not easy to get. For material characterization, bandstructure was chosen and compared with [71], [72], [73], [74]. This computation was done firstly using the semi-empirical Slater-Koster method, which can compute the same bandstructure as the experiment gives. Unfortunately, this method can't be used for further computation because of the lack of an appropriate parameter set for the pair zinc oxide - ammonia interaction.

To compute the gas sensor device in ATK, also LCAO method was chosen with exchange-correlation LDA, pseudopotential FHi basis set ZetaDoublePolarized. LCAO can't give the right bandgap; it underestimates it [75], but almost all the other physical observables are

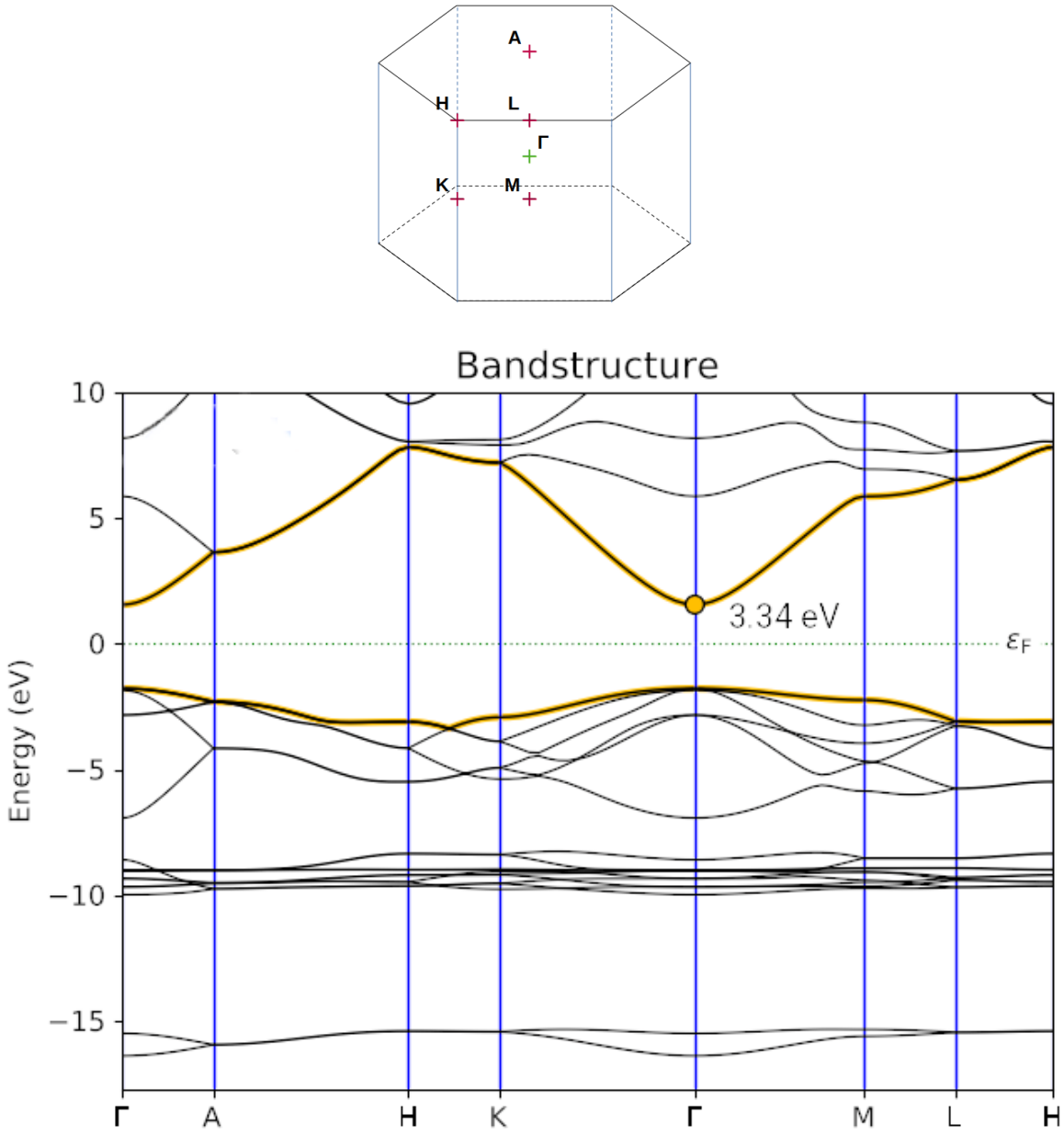

Figure 4.2: Computed electronic band structure for ZnO - wurtzite computed using the LCAO method (LDU + U scheme), describing the range of energies which an electron within the infinite ZnO crystal may have (so-called energy bands) and which ones it may not have (so-called band gaps). On the x-axis, paths between essential points in the k-space, 1st Brillouin zone (1BZ), are chosen. Γ point is the middle of the 1BZ, A, H, K, M, and L. See the picture above. Both energy bands above Fermi energy ϵ_F (zero energy level) and under it are emphasized, showing that there is a direct band gap at Γ point (the center of the 1st Brillouin zone) of 3.34 eV.

computed correctly (only physical property depending on bandgap, like refractive index, would be a problem). One of the possibilities to overcome this problem with bandgap is by introducing DFT+U schemes [76]. In this work, the journey using the LDA+U scheme was used, with Hubbard potential 8.53 eV for 2p orbital of oxygen and 10.5 eV for 3d orbital

of zinc. The resulting bandstructure is in good accordance with the literature cited above, estimating a direct bandgap of 3.34 eV, see 4.2.

The next complication is that QuantumATK uses a ballistic method, and a small piece of ZnO (used for computation) needs more free charge carriers. Therefore, a calculation of a ZnO piece without electrodes that can act as charge carrier donators are not reliable, see 4.4.

Because of that, the ZnO model was based on pure zinc electrodes with a zinc oxide sample sandwiched between them in the transition zone. The benchmark question was to find the electrodes' minimal size and the ZnO sample for which the current-voltage characteristic would be consistent with the evaluation data from [77]. The problem for ZnO is the effect of grain boundaries [78] - for which this model needs to be enhanced.

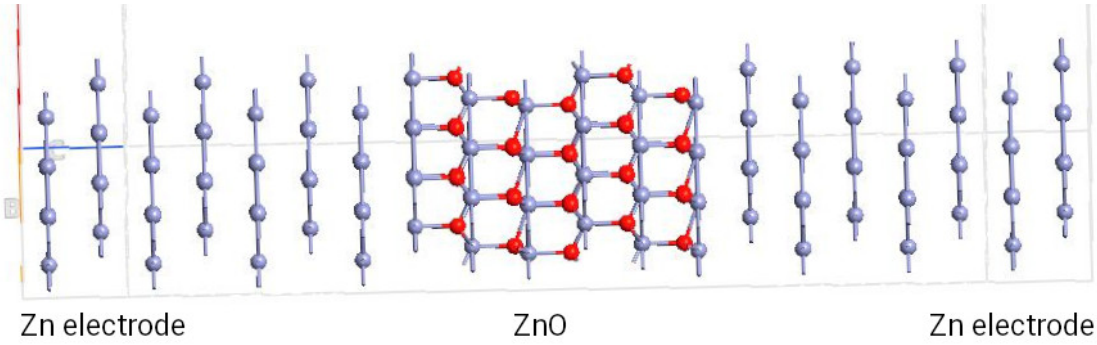

Figure 4.3: Numerical experiment geometry for zinc oxide: left and right pure zinc electrodes, in the middle zinc oxide in the transition zone.

From the benchmark, a device with a central region length (along primitive translation vector c) of 13.36 Å was chosen (see Fig. 4.3). In general, the ZnO-volume was formed by the composition of 2 x 3 x 3 (a x b x c) ZnO unit cells, volume 1972 Å^3. The current-to-voltage relation can be described as exponential

$$I = 6.26 \cdot 10^{-6} e^{1.96U} - 6.26 \cdot 10^{-6}, \tag{4.1}$$

as displayed in the form of I-V characteristic in Fig. 4.5.

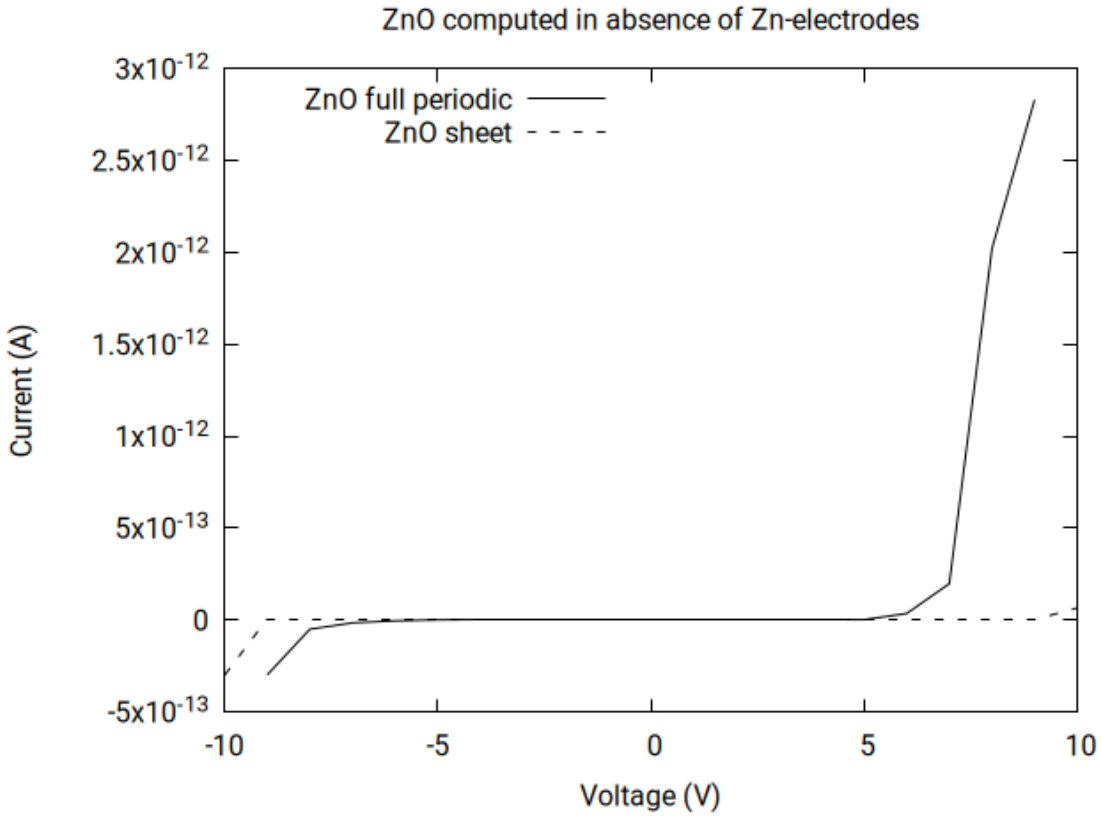

Figure 4.4: The current-voltage characteristic for ZnO computed using LCAO method without Zn-electrodes gives not reliable results.

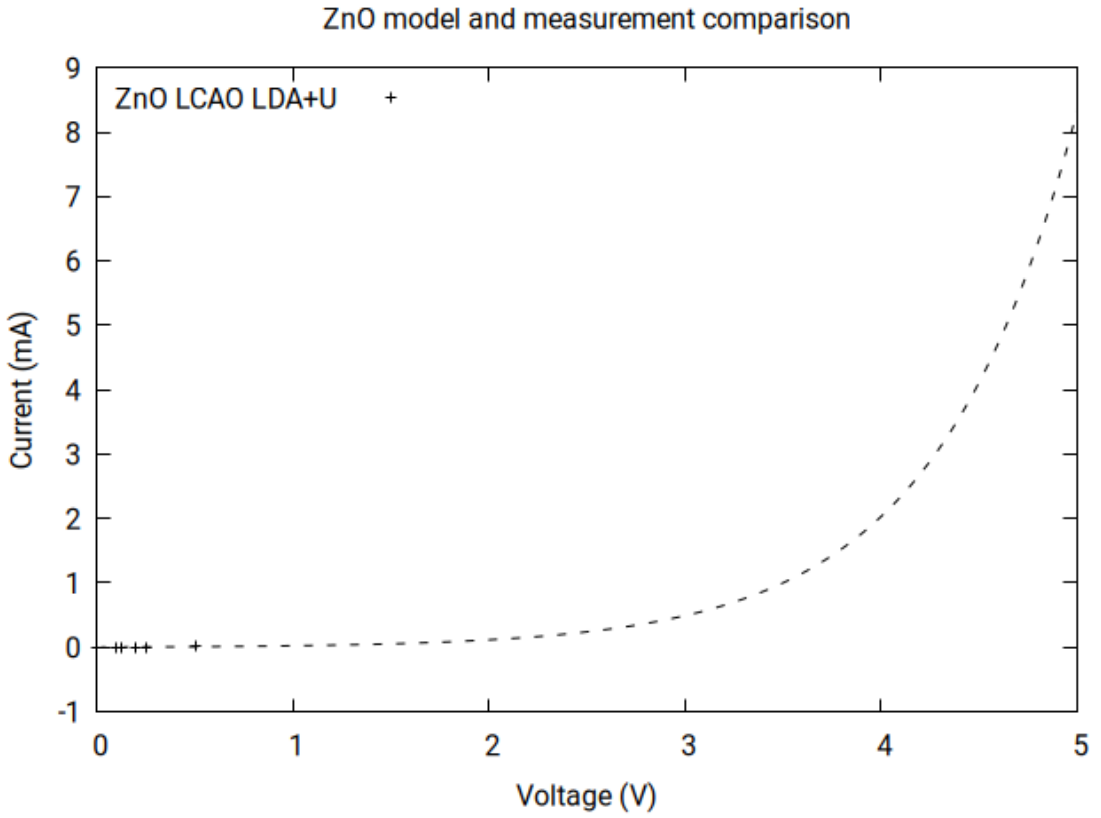

Figure 4.5: Sample data fitted via exponential function respond to the physical expectation of exponential current growth of milliampere range up to 5 V.

4.1.1 Effect of adsorbed ammonia molecules

In this constellation, the effect of one or more ammonia molecules on the device resistance was studied. To choose the position and orientation of the ammonia molecule, local energy minima using molecular dynamics were computed:

NH_3 amount pro device	distance of NH_3 to ZnO (Å)		
1	3.27	×	×
2	3.25	3.37	×
3	2.68	3.22	3.29

Table 4.1: Distances of ammonia molecules to zinc oxide surface.

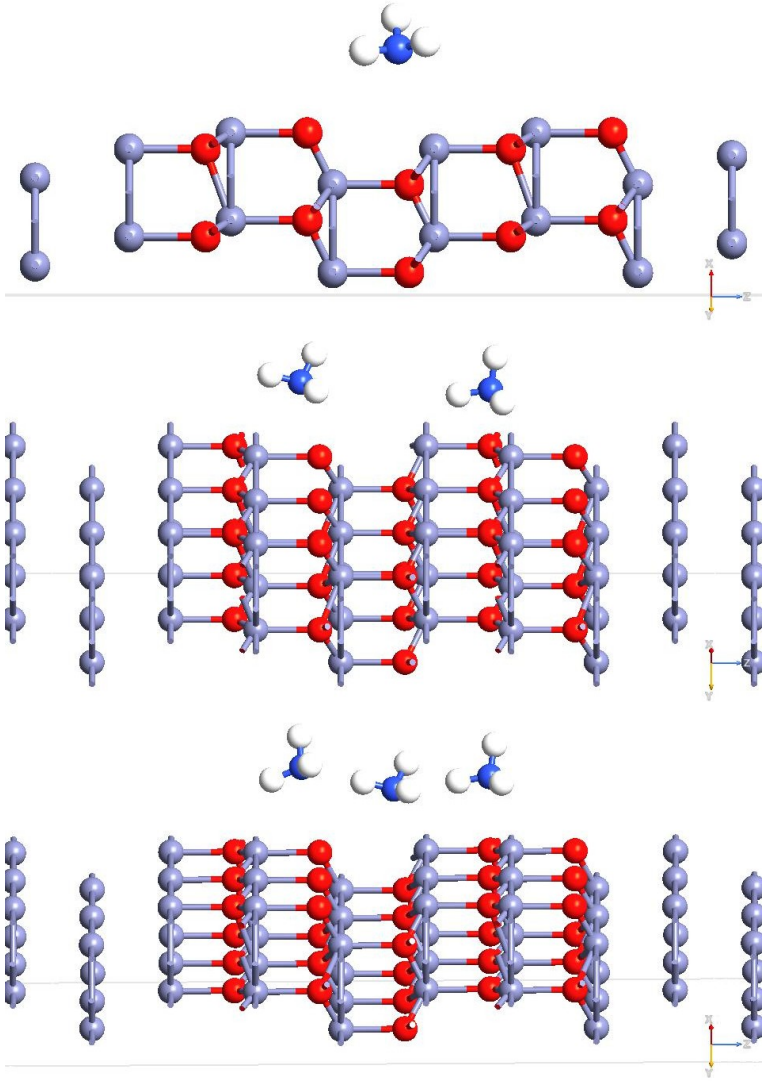

Figure 4.6: Device geometry with (a) 1 ammonia, (b) 2 ammonia, and (c) 3 ammonia gas molecules near to the zinc oxide surface - the distances ammonia - ZnO surface are displayed in Tab. 4.1.1.

In Fig. 4.7, the I-V characteristics for these constellations are displayed. The not natural current saturation of about 0.25 V is caused by the numerical model with a limited number of charge carriers. Therefore, the first part of the characteristic up to this voltage only was further examined in more detail; see Fig. 4.8. Data were fitted with a function

$$I = A \cdot e^{BU} + C, \tag{4.2}$$

yielding in $A \doteq 6.26 \cdot 10^{-6}$, $C \doteq -6.26 \cdot 10^{-6}$ and $B \doteq (1.76\ ,\ 1.95)$, see Tab. 4.1.1.

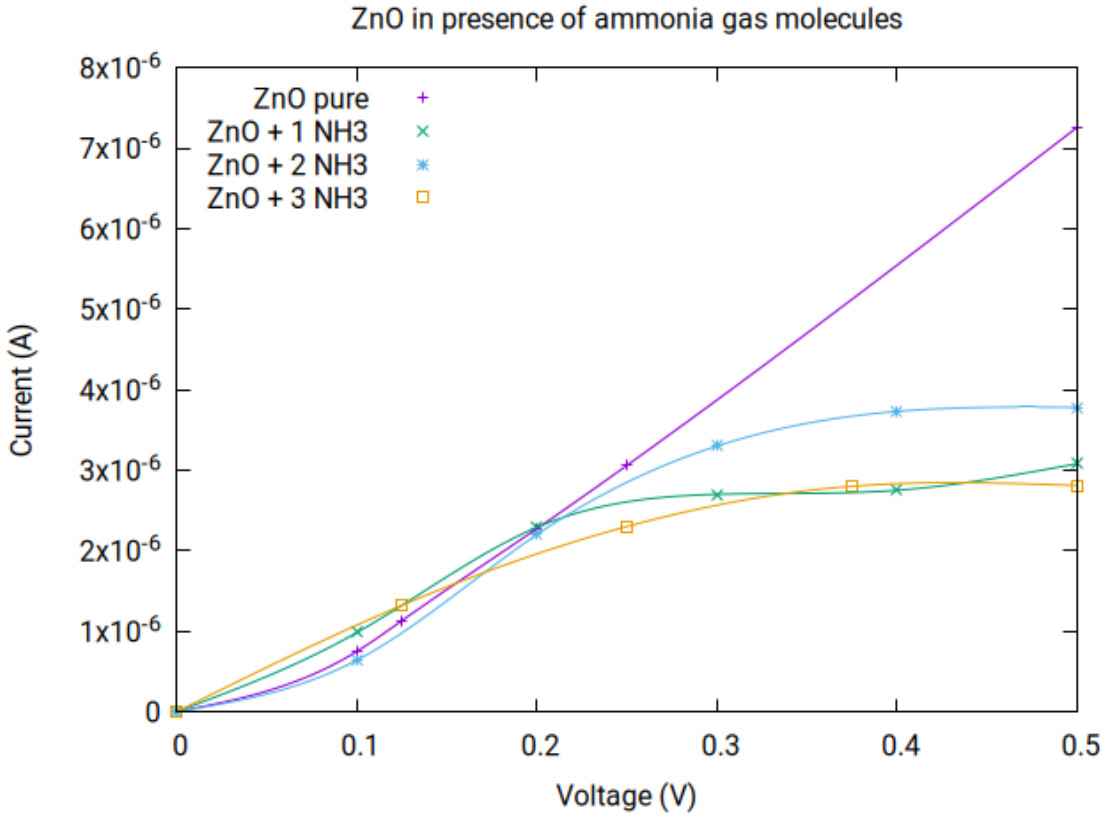

Figure 4.7: I-V characteristics for ZnO devices: pure (without any gas molecule) and with 1, 2, or 3 ammonia gas molecules, respectively.

NH_3 amount pro device	parameter B	$(R - R_0)/R_0$ (%)	gas concentration (ppm)
0	1.946		
1	1.827	6.48	34
2	1.755	10.84	68
3	1.462	33.05	102

Table 4.2: Relative resistance change and fitted exponent for different ammonia gas concentrations.

These data show that comparing the I-V characteristics of the ZnO device without gas molecules and with optimized position and orientation of one to three the gas molecule above

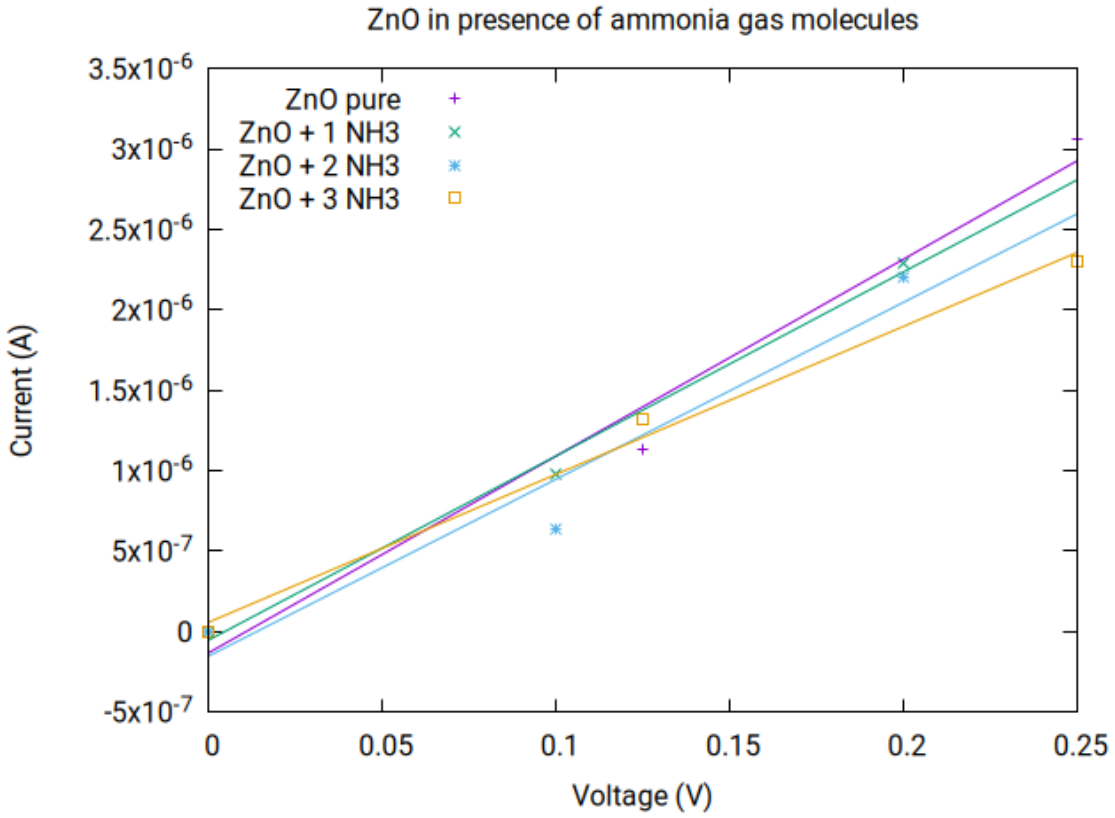

Figure 4.8: The I-V characteristics as in Fig. 4.7, focused on voltage range 0 - 0.25 V.

the zinc oxide surface, the current value while reaching saturating the voltage of about 0.25 V is for ZnO with 1 NH_3 more than 6% lower, with 3 NH_3 the resistance raised by 33%, see Tab. 4.1.1.

4.1.2 Comparison with experimental data

Virtual ammonia gas concentration through ppm (particle per million) was computed to compare this data with an experiment. Coming from the dimensions of the ZnO device part, in this case, the geometry with one ammonia molecule in the volume responds to the concentration of about 34 ppm, and so on, up to 102 ppm concentration for three ammonia gas molecules in the volume, see Tab. 4.1.1. These data were compared with experimental results of gas sensitivity of ZnO-based thick film sensor to NH_3 at room temperature from Rao et al. [79]. This comparison in Fig. 4.9 shows that the zinc oxide sensibility to ammonia is about six times lower yielding from the numerical model than in the experiment. The numerical computation does underestimate the material response.

It is necessary to mention that the real ZnO bulk would be different from the numerical device: The modeled was 'monocrystalline' material although, in real life, the ZnO is polycrystalline (so in Rao et al.), kinetic effects, inter-carrier influences, and other effects. It was mentioned that this numerical model does not include the grain boundary effect, which plays an important role in the current growth with growing voltage, see [80], which is a great area for improvement of this numerical model. But, on the other hand, this model shows that in the absence of these effects, the zinc oxide material still reacts on NH_3 gas molecules

stating: the zinc oxide sensibility to ammonia gas has a mixed background of about one-sixth influenced by pure ZnO material (monocrystalline), and five-sixths may be other effects like grain boundary conductance.

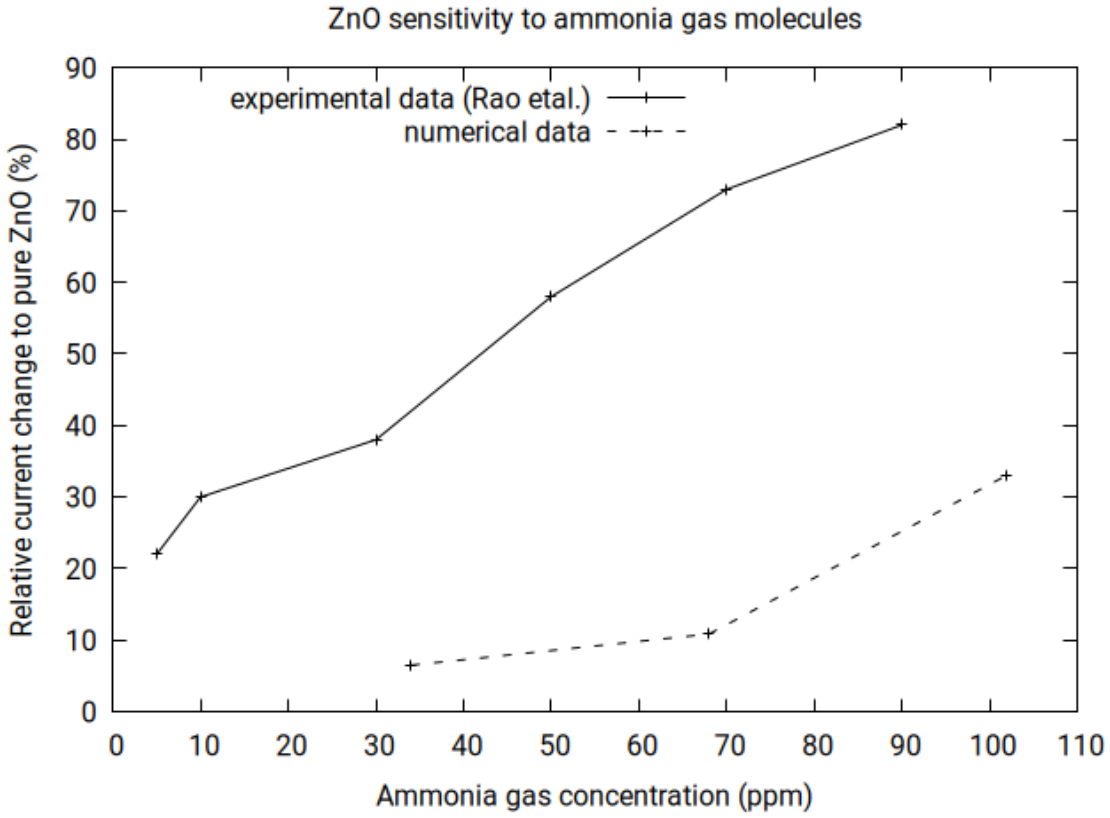

Figure 4.9: Computed relative current change of ZnO device concerning ammonia gas concentration (dashed line) compared with experimentally examined thick film ZnO device sensitivity by [79].

4.2 Graphene

Graphene is chosen to be studied as a gas sensor because it is in between semi-conductors like zinc oxide and conductors like polyaniline while based on non-crystalline stable material, which can adsorb/desorb gas molecules reversible, and due to its 2D-structure high surface-to-bulk ratio.

Numerical graphene methods in QuantumATK are well adapted, but the problem is that pristine graphene may be rather inert to gases ([48]). To establish charge transfer between the target gas molecule and the graphene layer, graphene has to be at some doping level; a defect is needed ([51]). Let us assume such a perturbation is also the graphene layer edge. The questions for this work are:

Does layer edge and how does it affect graphene's sensibility to gases? Can numerical experiment clearly distinguish between pristine layer and finite-width ribbon? Where does a gas molecule of NH_3, NO_2, CO settle?

For this work, graphene in the form of a single nanolayer and single nanoribbon was studied. The electrical properties of graphene were studied by Synopsis QuantumATK ver. 2020.09. To obtain the material characteristics for different configurations, a semi-empirical tight-binding method was chosen, specifically the Extended Hückel Method [41] using Cedra Hückel basis set for carbon because of perfect data accordance (bandstructure, density of states) to measured values of graphene, see below. For the Extended Hückel Method and the non-bulk, device computation, non-equilibrium Green's functions formalism (NEGF) was applied [34]. The band structure for the infinite graphene layer computed by this method is displayed in Fig. 4.10).

For this model, no metal contacts for the electrodes were considered. The device comprises one graphene nanosheet/nanoribbon, and the electrode parts are without perturbative potentials. The boundary conditions are fully periodic. The perturbation - a gas molecule or others - is placed in the central part of the device. The so-called electrode-extension area is placed between the electrodes and the central area. QuantumATK uses so-called screening approximation: the electrodes are solved as a bulk material. Therefore, assuming that the current flowing in the device is small enough, the screening approximation applies so that the electrode regions can be approximated by an equilibrium electron distribution [34].

The band structure and density of states (DOS) of all the considered geometries were computed and compared with available data for benchmark purposes. When the optimal numerical system was found (Extended Hückel Method, Cedra Hückel basis set for carbon, suitable density mesh cut-off, and k-point sampling), transmission spectra for such devices were computed. Nextly, the devices were perturbed by one gas molecule at a time, ammonia, nitrogen dioxide, and carbon oxide, and the new transmission spectra were calculated. From this, the effect of the graphene systems in the form of resistance change was obtained.

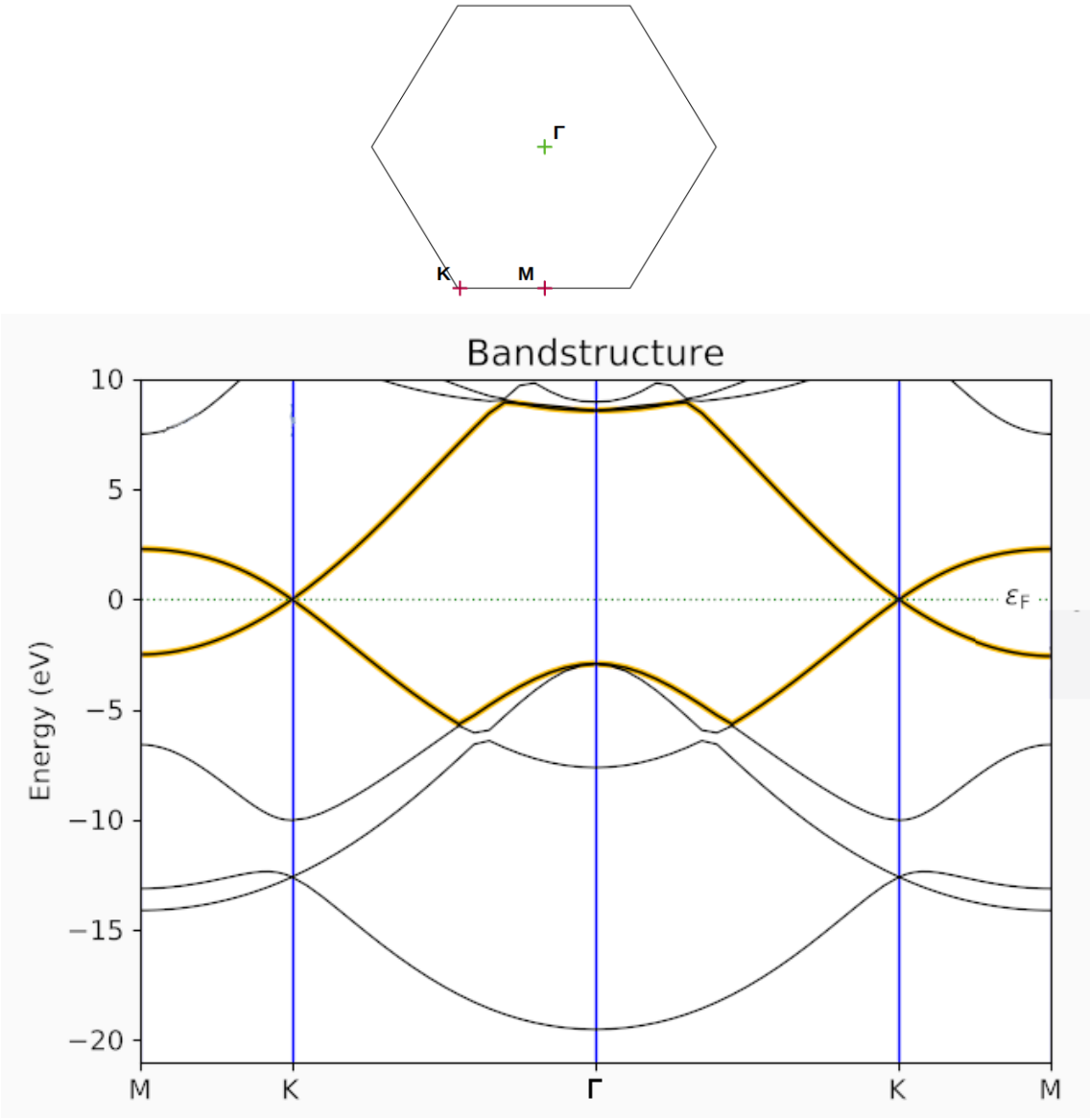

Figure 4.10: Computed electronic band structure for graphene. On the x-axis, paths between essential points in the k-space, 1st Brillouin zone (1BZ), are chosen. Γ point is the middle of the 1BZ, K and M see picture above. Both energy bands above Fermi energy ϵ_F and under it are emphasized, showing zero band gap at (every) K point.

4.2.1 Nanoribbon vs. Nanosheet

At first, I-V characteristics for these particular graphene geometries were compared:

		device active area length (Å)
nanoribbon Fig. 4.11	zig-zag W=4	12.31
nanoribbon Fig. 4.12	armchained W = 8	13.05
nanosheet Fig. 4.13	(4,1)	13.02

where W means width, also zig-zag W=4 is a nanoribbon of 4 carbon atoms width and one hydrogen passivation at every edge, armchained nanoribbon W=8 is of width eight

carbon atoms and two hydrogens at every border, nanosheet is infinite in the plane and thus not passivated.

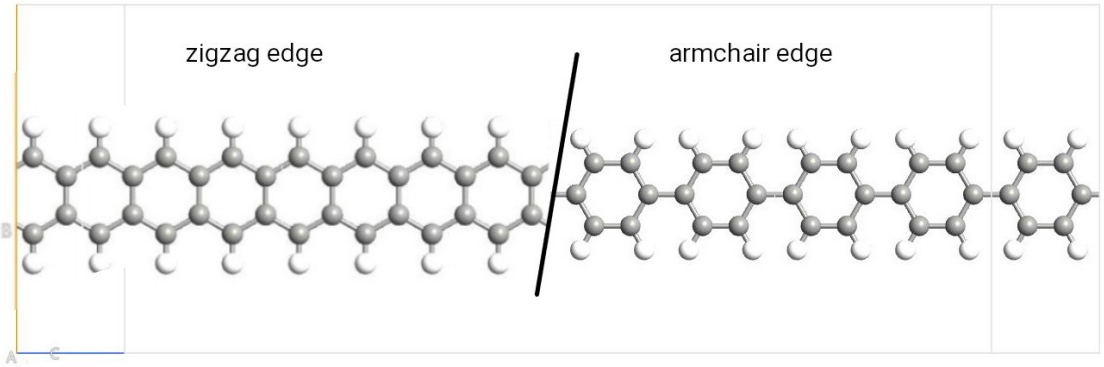

Figure 4.11: Graphene nanoribbon zig-zag W=4 (left) and armchain W=3 (right)

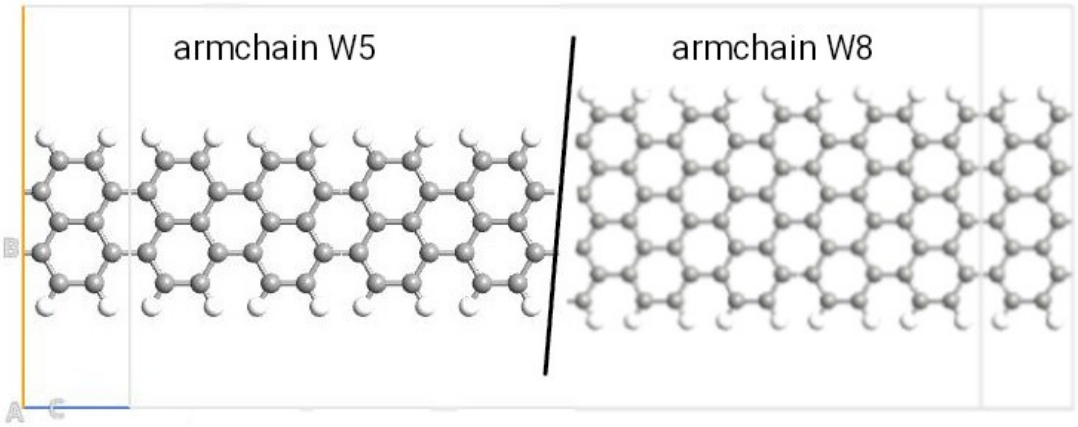

Figure 4.12: Armchained graphene nanoribbon W=5 and W=8

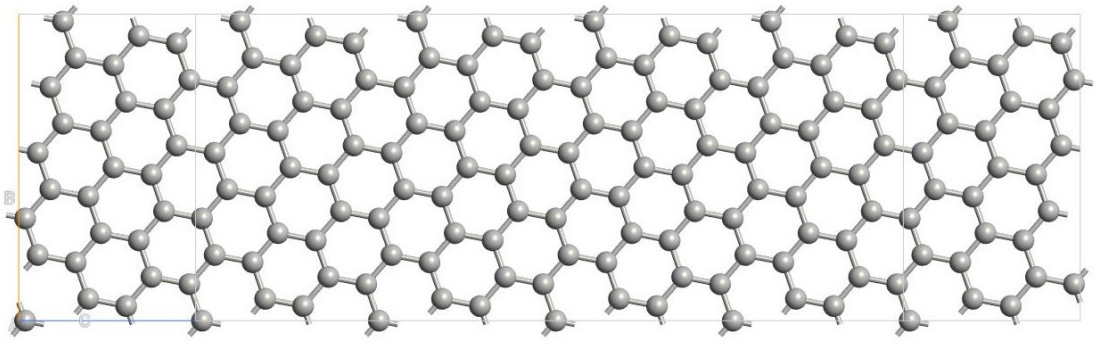

Figure 4.13: Graphene nanosheet (4,1)

The computation displayed in Fig. 4.14 showed that the highest current growth has

the tiniest graphene geometry - a geometry of only one benzene ring width, armchained nanoribbon W=3 and zig-zag nanoribbon W=4 (Fig. 4.11), the lowest current growth has the infinite nanolayer (4,1) (Fig. 4.13). Between I-V characteristics of armchained graphene W5 and W8 is rather no difference. These results comply with the abovementioned idea that the conductance is coupled with distortions (graphene layer edge). A higher response to disturbing gave the armchained geometry than the zig-zag geometry.

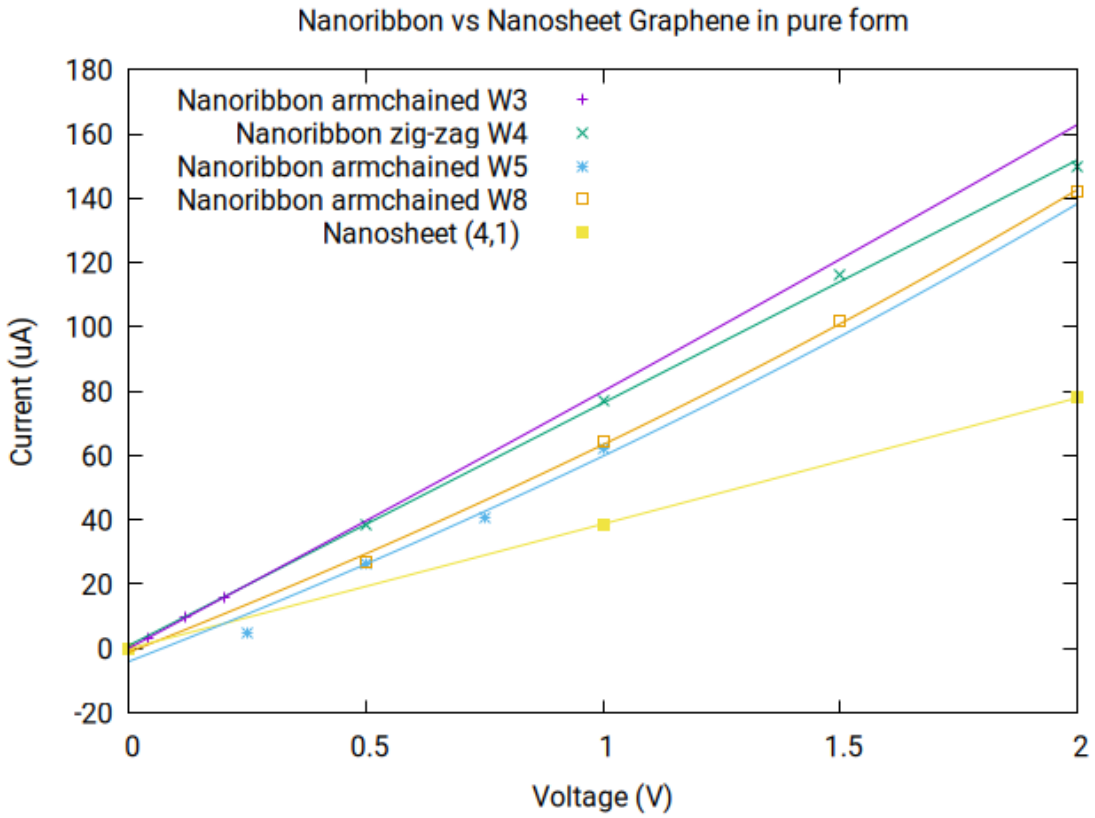

Figure 4.14: Nanoribbon zig-zag, armchained, and nanosheet graphene in comparison without any impurity/gas molecule, all data fitted with an exponential function.

For further investigation, geometries nanoribbon zig-zag W4, nanoribbon armchained W8, and nanosheet (4,1) were chosen, and their response to selected gases will be evaluated.

4.2.2 One NH_3, NO_2 and CO gas molecule adsorption

The sensibility to gases like ammonia, nitrogen dioxide, or carbon monoxide is expected to differ for different "pristine" graphene geometries where the chain edge is the only disorder.

Firstly, the most narrow geometry, armchained nanoribbon W=3, was examined: the effect of one ammonia, nitrogen dioxide, or carbon oxide molecule on the device resistance was studied. Local energy minima using molecular dynamics were computed for the position and orientation of the ammonia molecule.

The ammonia molecule was located over the nanoribbon, in between the central ribbon line and the passivated ribbon edge, see Fig. 4.15:

	distance between two nearest atom centres (Å)
N-C	3.53
N-H	3.67

The nitrogen dioxide molecule was located next to the nanoribbon, in the same plane as the ribbon line, see Fig. 4.16:

	distance between two nearest atom centres (Å)
O_1-H	2.46
O_2-H	2.54
N-H	2.49

The carbon oxide molecule was located similarly to nitrogen dioxide, next to the nanoribbon, but rotated from the ribbon plane of about 30 deg, see Fig. 4.17:

	distance between two nearest atom centres (Å)
O-H	2.52
C-H	3.28

In Fig. 4.18, the I-V characteristics for these constellations are displayed. These data were fitted with a function

$$I = A \cdot e^{BU} + C, \tag{4.3}$$

which $A \doteq 9 \cdot 10^{-3}$, $C \doteq -9 \cdot 10^{-3}$ and B see Tab. 4.2.2. The relative current change was computed, yielding about a six percent resistance rise for ammonia and nitrogen dioxide and only about 0.3 percent for carbon oxide, see Fig. 4.19 and Tab. 4.2.2.

	parameter B	relative current change tu pure W3
pure W3	$8.80 \cdot 10^{-3}$	
W3 + NH_3	$8.27 \cdot 10^{-3}$	6.0 %
W3 + NO_2	$8.26 \cdot 10^{-3}$	6.1 %
W3 + CO	$8.77 \cdot 10^{-3}$	0.3 %

Table 4.3: Relative resistance change for graphene armchained nanoribbon W=3 and fitted exponent for different ammonia gas concentrations.

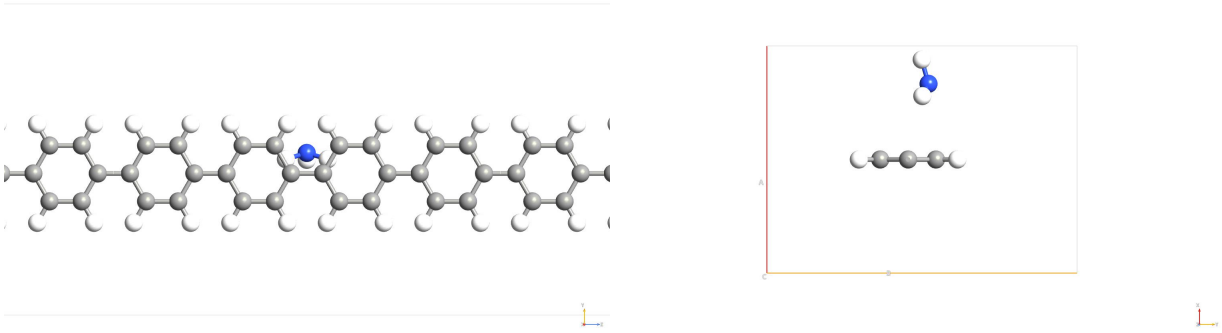

Figure 4.15: Armchained graphene nanoribbon W=3 and NH_3-molecule position

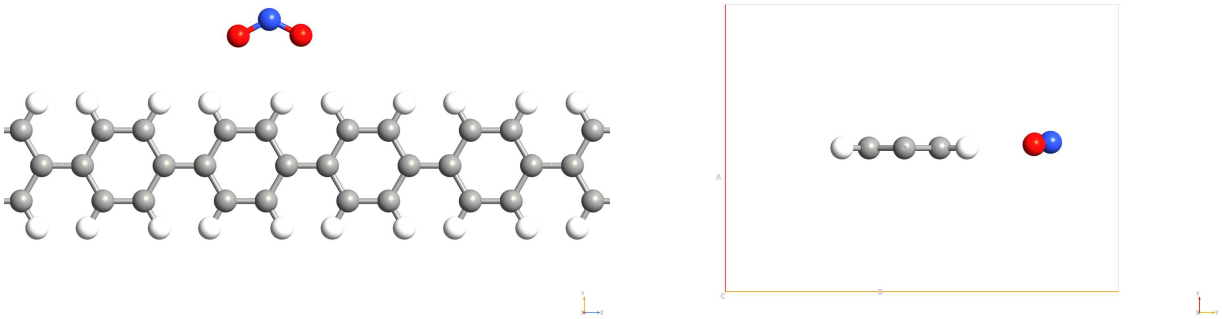

Figure 4.16: Armchained graphene nanoribbon W=3 and NO_2-molecule position

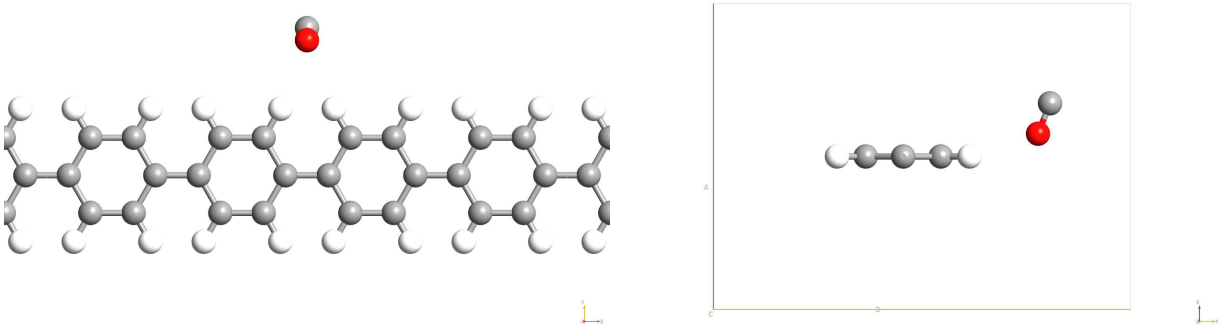

Figure 4.17: Armchained graphene nanoribbon W=3 and CO-molecule position

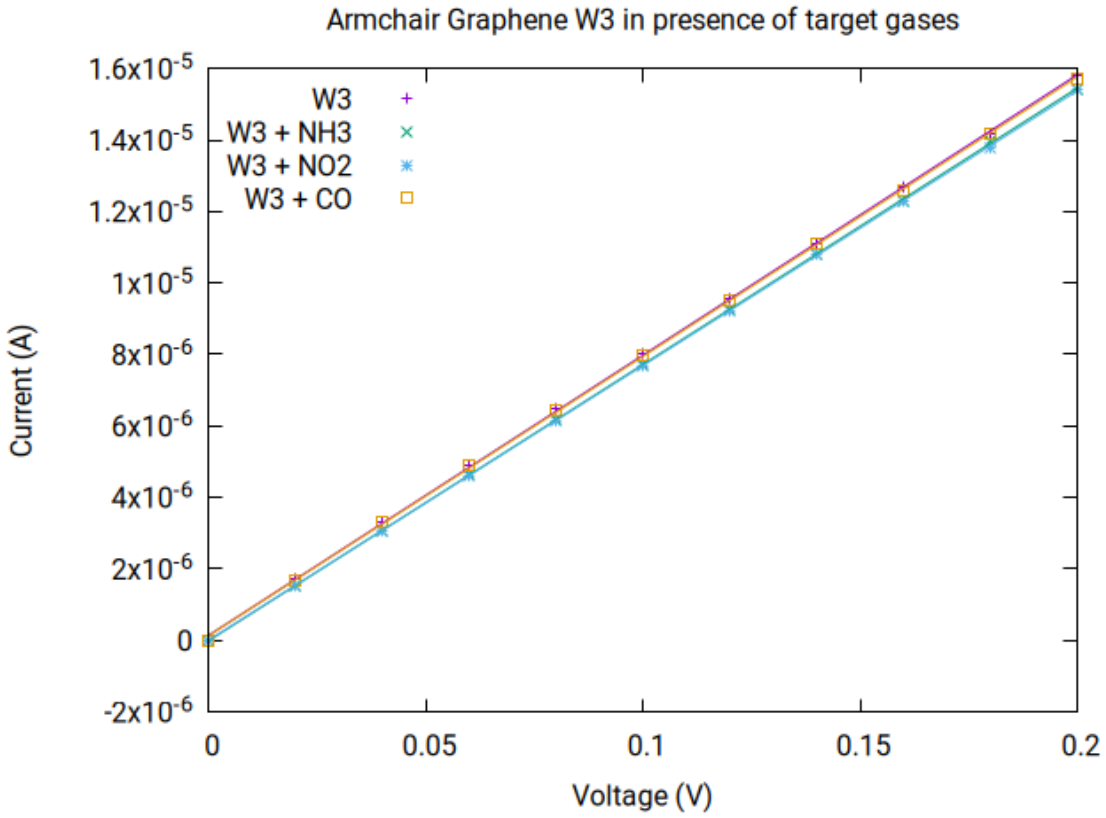

Figure 4.18: Armchained graphene W3 and gas response to CO, NH_3 and NO_2

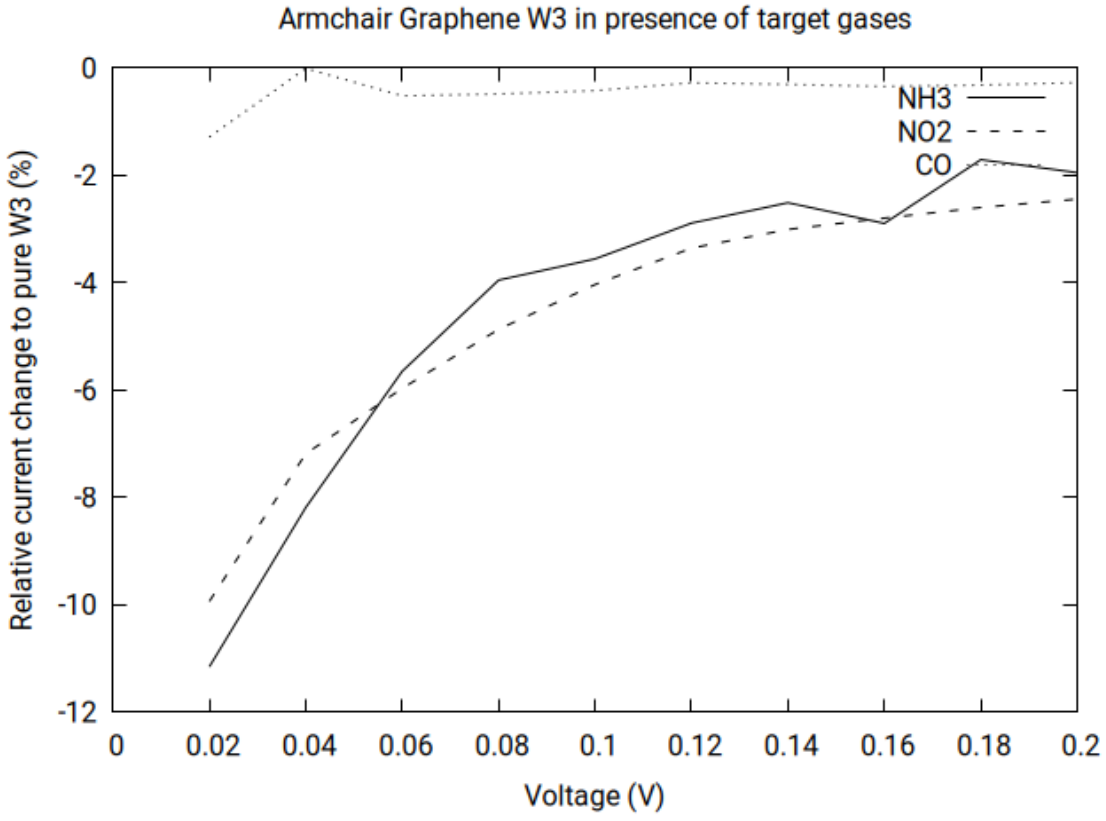

Figure 4.19: Armchained graphene W3 and gas response to CO, NH_3 and NO_2 - relative current change

Similarly, the target gas molecule position near the armchained graphene nanoribbon W8 was estimated, and their effect on I-V characteristics was measured. For this case, the target gas molecules were placed over the nanoribbon, where their position using minimal energy optimation was determined, see Fig. 4.20, 4.21, and 4.22.

	distance between two nearest atom centres (Å)
H-C	2.28
N-C	2.78

	distance between two nearest atom centres (Å)
O-C	1.34
N-C	2.52

	distance between two nearest atom centres (Å)
O-C	1.47
C-C	2.42

In Fig. 4.23, the I-V characteristics for these constellations are displayed. These data were fitted with a function

$$I = A \cdot e^{BU} + C, \tag{4.4}$$

which $A \doteq 1.7 \cdot 10^{-4}$, $C \doteq -1.7 \cdot 10^{-4}$ and B see Tab. 4.2.2. The relative current change was computed, yielding about ten percent resistance rise for nitrogen dioxide, four percent for carbon dioxide, and just no response for ammonia, see Fig. 4.24.

	parameter B	relative current change tu pure W8
pure W8	$3.01 \cdot 10^{-1}$	
W8 + NH_3	$3.01 \cdot 10^{-1}$	0 %
W8 + NO_2	$2.71 \cdot 10^{-1}$	10.0 %
W8 + CO	$2.89 \cdot 10^{-1}$	4.0 %

Table 4.4: Relative resistance change for graphene armchained nanoribbon W=8 and fitted exponent for different ammonia gas concentrations.

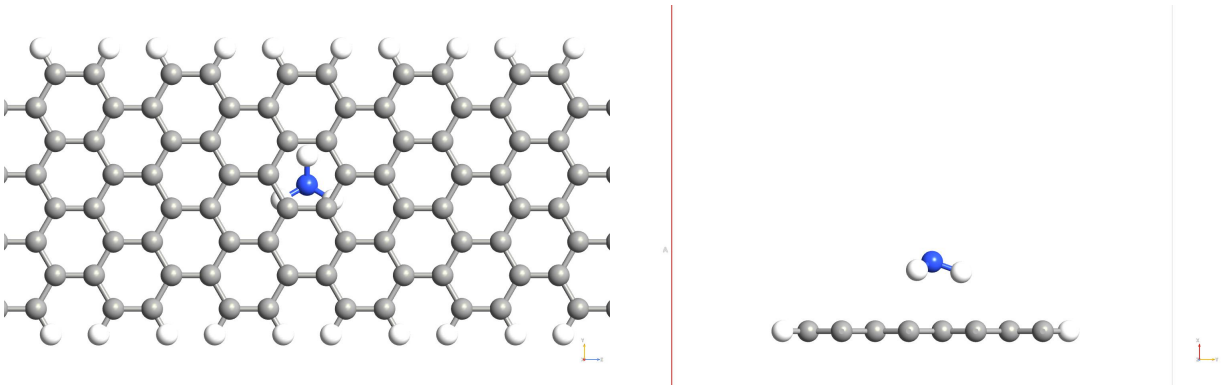

Figure 4.20: Armchained graphene nanoribbon W=8 and NH_3-molecule position

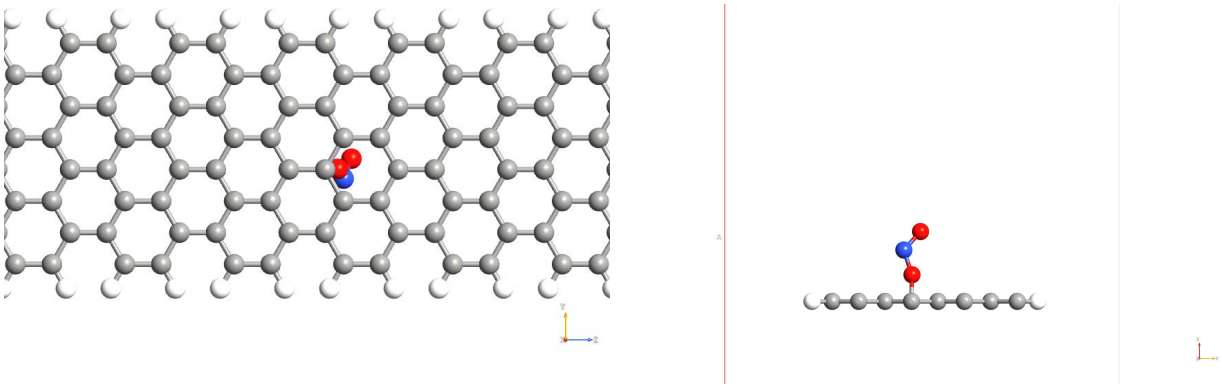

Figure 4.21: Armchained graphene nanoribbon W=8 and NO_2-molecule position

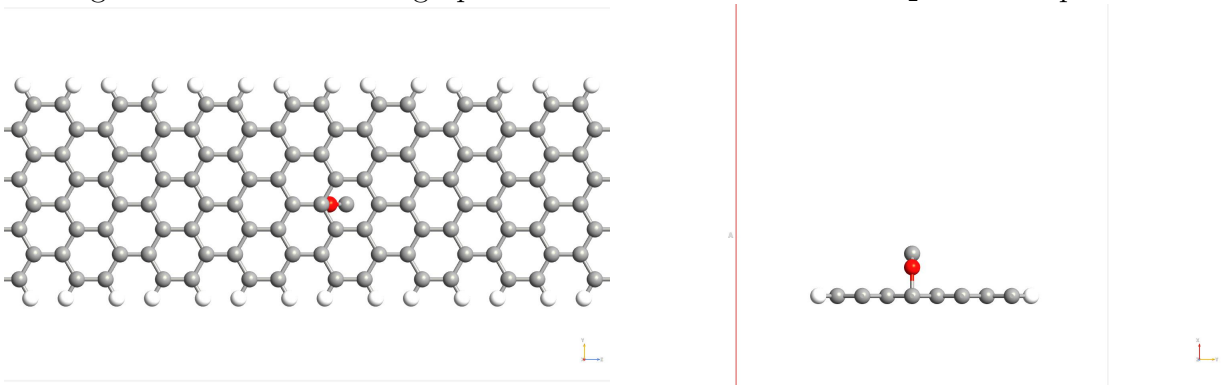

Figure 4.22: Armchained graphene nanoribbon W=8 and CO-molecule position

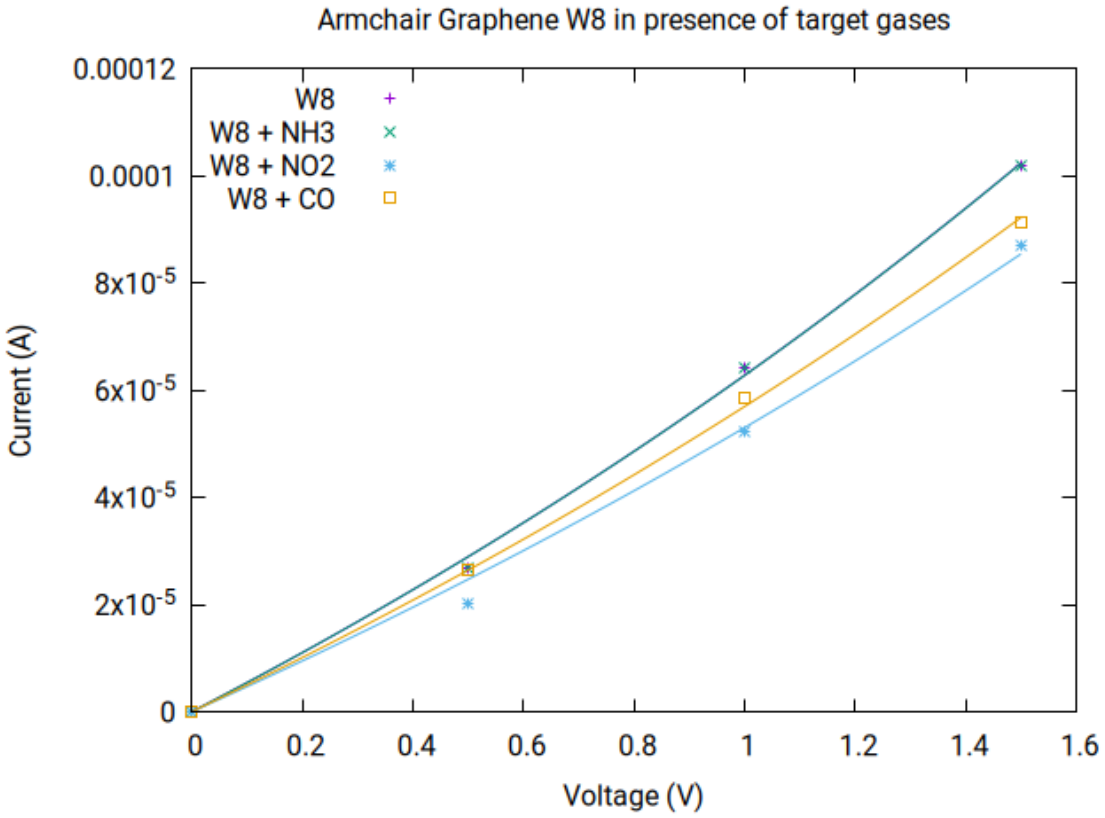

Figure 4.23: Armchained graphene W8 and gas response to CO, NH_3 and NO_2

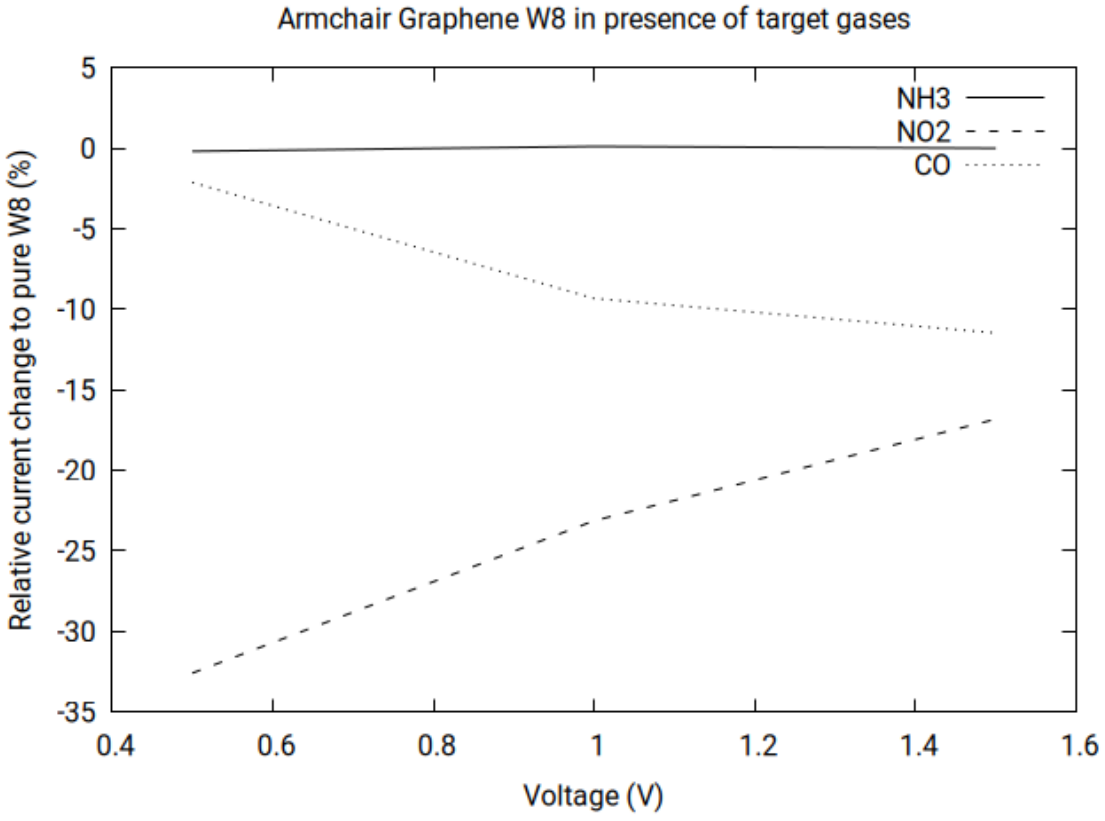

Figure 4.24: Armchained graphene W8 and gas response to CO, NH_3 and NO_2 - relative current change

Finally, the same numerical experiment was also driven for infinite graphene nanosheet (4,1) where target gases molecule were dropped over this sheet, and their position was estimated through energy minimum optimation, see Fig. 4.25, 4.26, and 4.27.

The position of target gas molecules was determined to be:

	distance between two nearest atom centres (Å)
H-C	2.36
N-C	2.89

	distance between two nearest atom centres (Å)
O-C	2.59
N-C	2.88

	distance between two nearest atom centres (Å)
O-C	3.07

In Fig. 4.23, the I-V characteristics for these constellations are displayed. These data were fitted with a function

$$I = AU + B, \tag{4.5}$$

where $B \doteq 0$ and slope A see Tab. 4.2.2. The relative current change was computed, yielding about 1.5 percent resistance rise for nitrogen dioxide, less than half percent resistance lowering for ammonia, and only about 0.03 percent for carbon oxide, see Fig. 4.25 - 4.27.

	parameter A	relative current change to pure nanosheet (4,1)
pure NS	$3.878 \cdot 10^{-5}$	
NS + NH_3	$3.894 \cdot 10^{-5}$	-0.41 %
NS + NO_2	$3.820 \cdot 10^{-5}$	1.50 %
NS + CO	$3.877 \cdot 10^{-5}$	0.03 %

Table 4.5: Relative resistance change for graphene nanosheet (4,1) and fitted exponent for different ammonia gas concentrations.

Comparing results for armchained nanoribbon W3, W8, and nanosheet (4,1) in Tab. 4.2.2, the most gas response does the W3 nanoribbon, where the gas molecules were positioned on edge. The W8 nanoribbon showed high sensibility for gases that were settled near its surface (NO_2 and CO) compared to NH_3, being positioned higher over the surface and with just no effect on the current change. As expected, the pristine infinite graphene nanosheet showed no sensibility to the gases near its surface. For all the graphene sensor devices states that the most sensibility was proven for NO_2 and the lowest for CO, see Fig. 4.30.

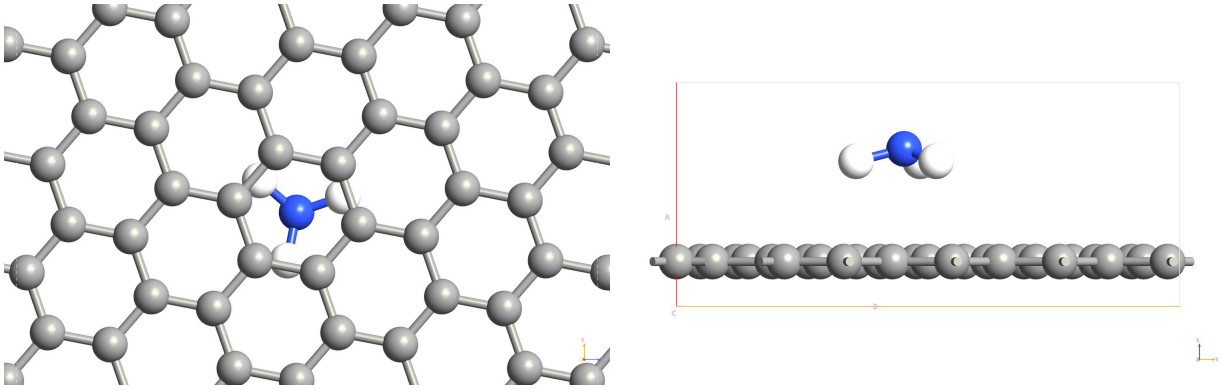

Figure 4.25: Armchained graphene nanosheet (4,1) and NH_3-molecule position

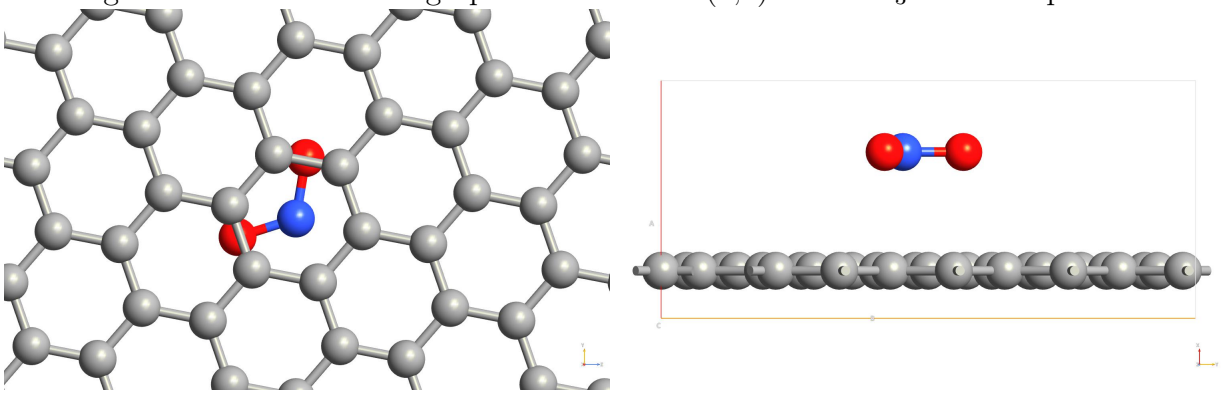

Figure 4.26: Armchained graphene nanosheet (4,1) and NO_2-molecule position

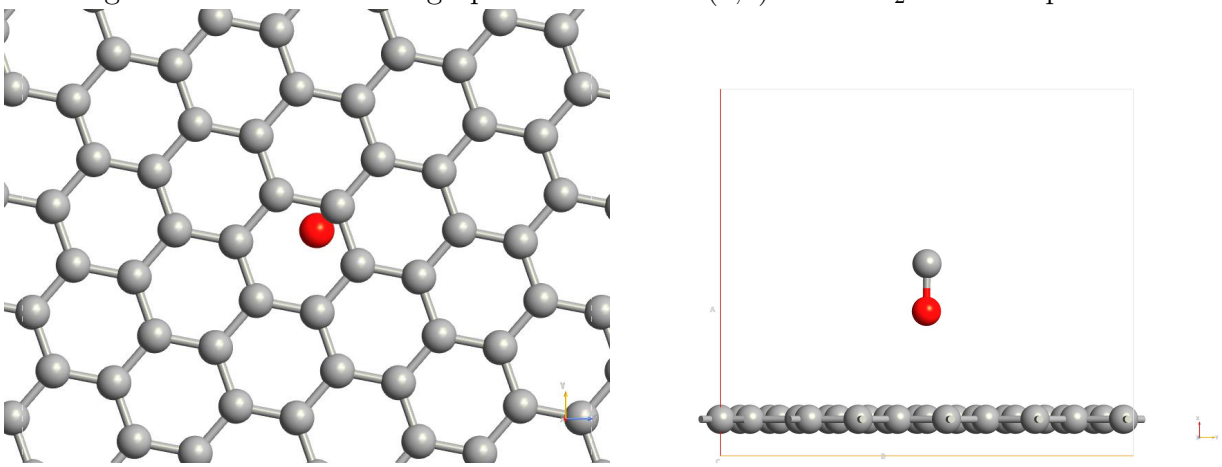

Figure 4.27: Armchained graphene nanosheet (4,1) and CO-molecule position

current response change (%)	W3	W8	NS
NH_3	6.0	0.0	-0.4
NO_2	6.1	10.0	1.5
CO	0.3	4.0	0.0

Table 4.6: Comparison of current response for graphene armchained nanoribbon W=3, W=8 and infinide nanosheet.

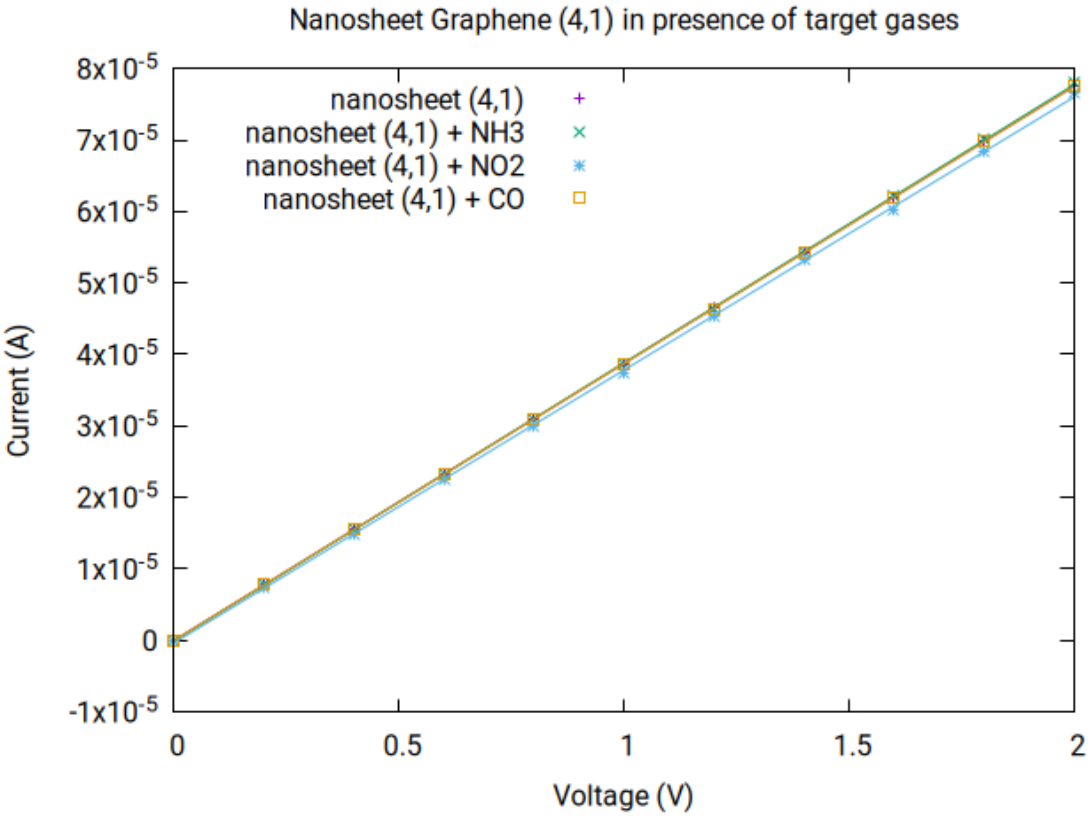

Figure 4.28: Nanosheet graphene (4,1) and gas response to CO, NH_3 and NO_2

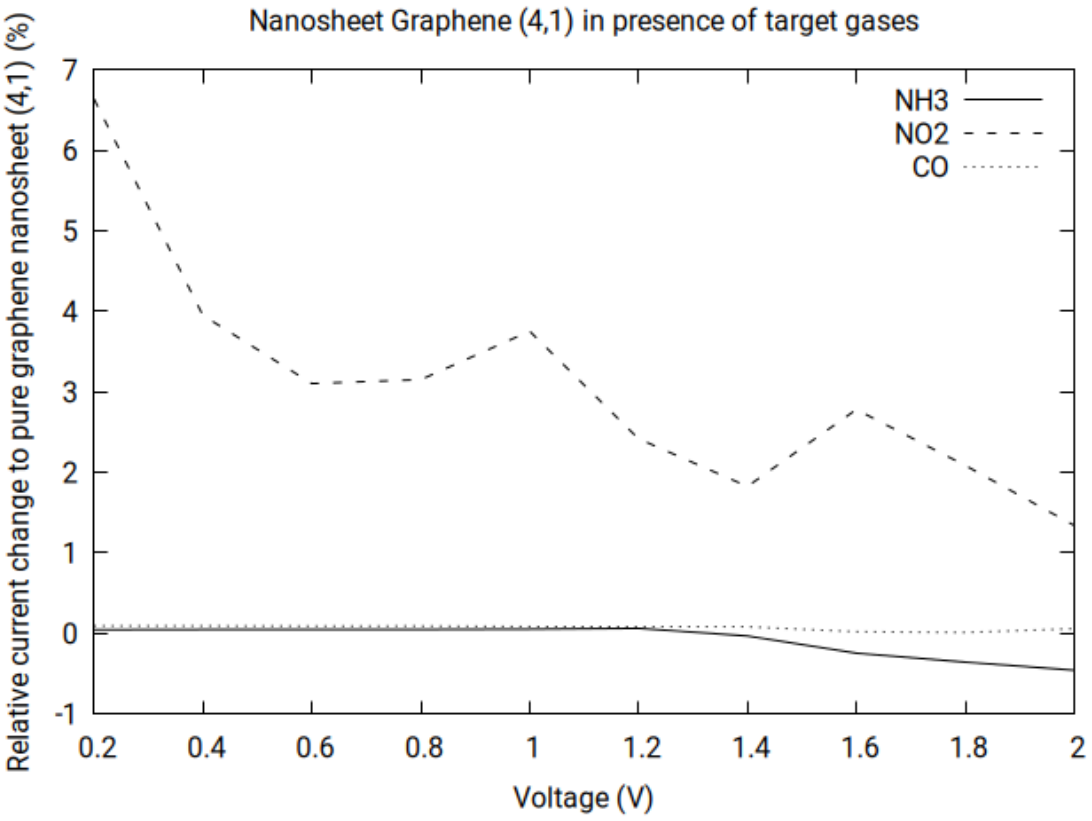

Figure 4.29: Nanosheet graphene (4,1) and gas response to CO, NH_3 and NO_2 - relative current change

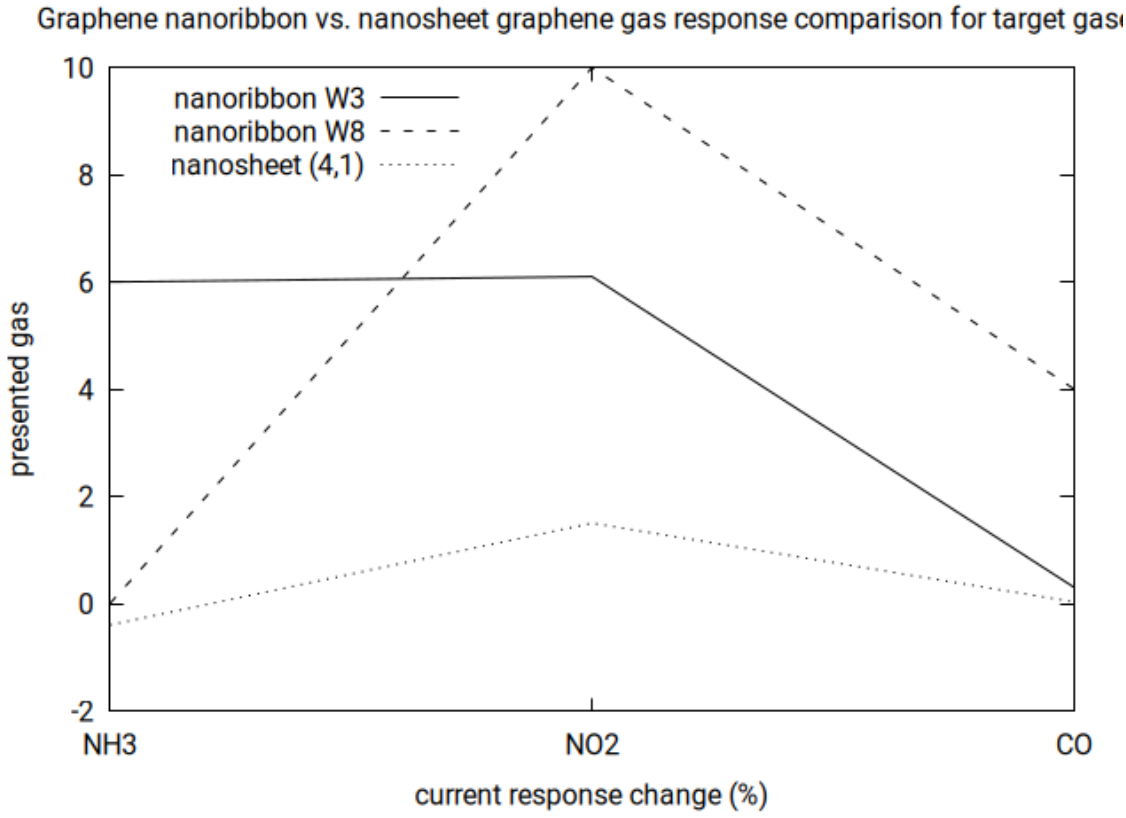

Figure 4.30: Graphene nanoribbon vs. nanosheet graphene gas response comparison for CO, NH_3 and NO_2

4.3 Polyaniline

The first step for a numerical simulation of PANI interacting with gas is a reliable construction of the PANI variation, emeraldine salt. This variation was modeled with known molecule parameters ([62]) and the density of states (DOS) and band structures were compared. After that, a device consisting of polyaniline was built, and its transmission spectra were computed.

Chain length optimization chose a 32-mer molecule as a basic device.

4.3.1 One-chain PANI in interaction with one NH_3 gas molecule

This section corresponds to the published article in Physica E: Low-dimensional Systems and Nanostructures [A]

In the emeraldine salt molecule, every second nitrogen is doped (in this computation, every upper nitrogen is doped, see Fig.4.31). The interacting gas molecule can be positioned

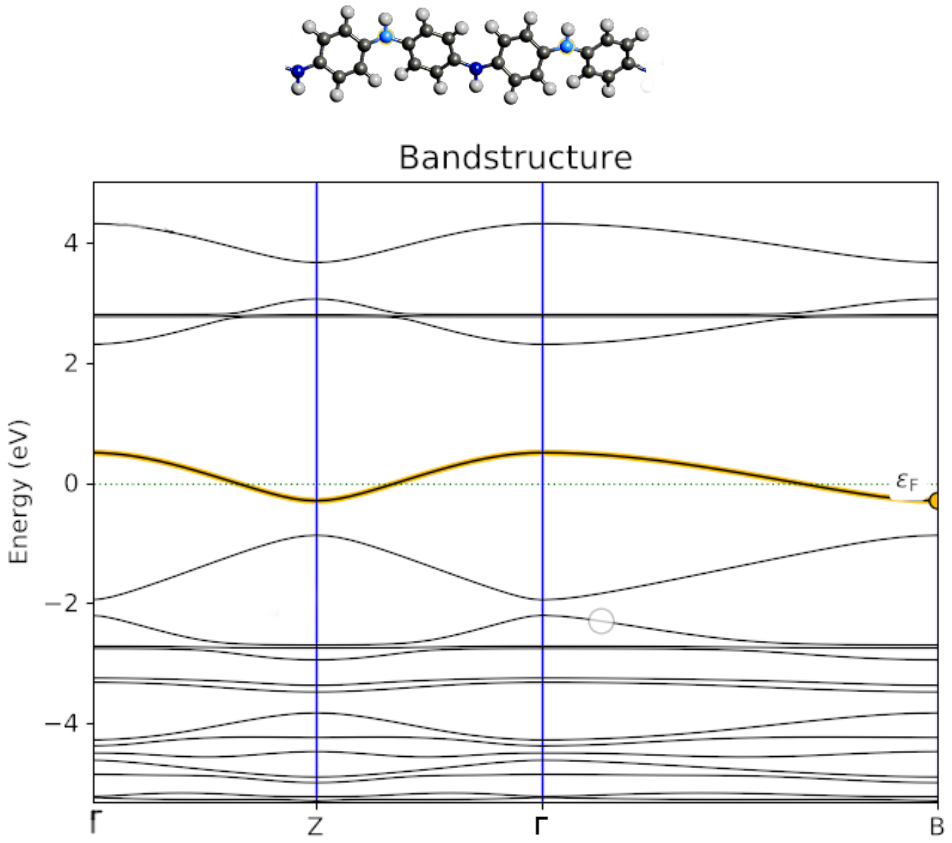

Figure 4.31: Above one mer of emeraldine salt with optimized angles between atoms, nearing the values from [62]. In the molecule, every upper nitrogen atom is doped (light blue color), and the lower is not (dark blue color). Below the molecule is the computed electronic band structure for the infinite PANI chain. On the x-axis, paths between essential points in the k-space, 1st Brillouin zone (1BZ), are chosen. Γ point is the middle of the 1BZ, Z, and B points are in the center of facets. The energy band about Fermi energy ϵ_F is emphasized as this band shows that there is no gap which means that the structure has free electrons and can conduct electric current.

near the doped nitrogen atom or the second, undoped nitrogen atom (Fig.4.32), near the benzene center in the middle (Fig.4.33), and somewhere else. Next, the gas molecule orientation was varied. These three space positions of the molecule, together with different molecule orientations, were computed, and also one position was chosen free from energy-minimizing optimization of position and orientation. For all of these numerical experiments, transmission spectra were computed. From these data, the I-V characteristics were derived.

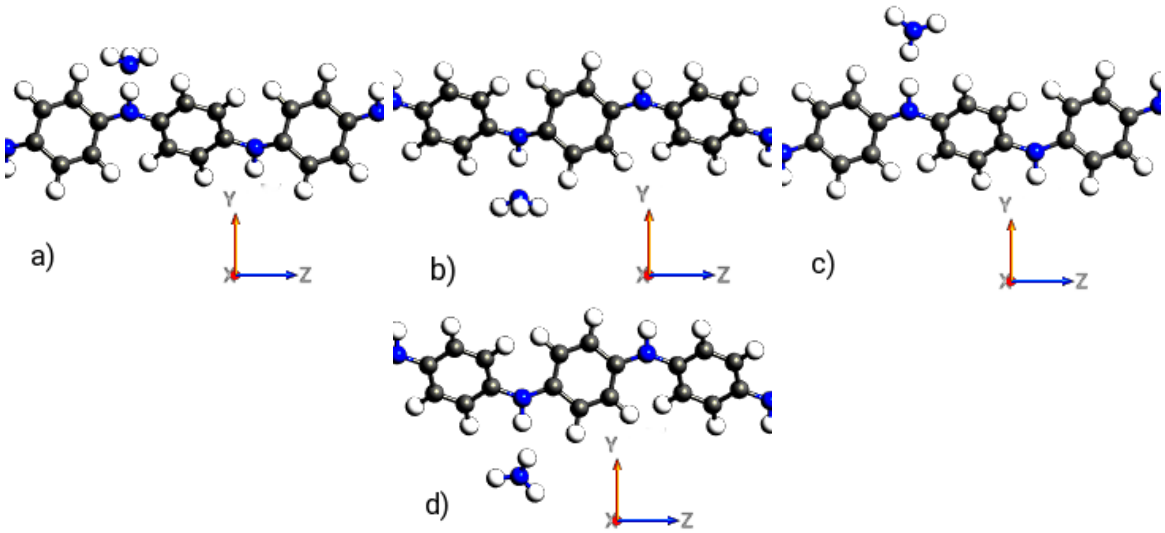

Figure 4.32: Four of modeled position and orientation of ammonia molecule: a) the NH_3 molecule near the doped nitrogen atom oriented with the nitrogen atom to the nitrogen atom of the PANI chain, b) the NH_3 molecule near the undoped nitrogen atom of the PANI chain, oriented with the nitrogen atom to the nitrogen atom of the PANI chain. c) the NH_3 molecule near the doped nitrogen atom, the ammonia molecule after minimum energy optimization of position and orientation, d) c) the NH_3 molecule near the doped nitrogen atom, the ammonia molecule, after minimum energy optimization of position and orientation.

Because of one molecule chain and only one gas molecule acting on a chain, a current saturation is expected - the amount of free charge carriers is limited and small beside to macroscopic PANI stripe. For the data discussion, the linear part (before saturation occurs) is important - for electric resistance estimation or measurable I-V characteristics of a polyaniline gas sensor.

At first, the fixed positions of the ammonia gas molecule without optimization were chosen. The orientation of the NH_3-a molecule with its nitrogen atom facing the doped nitrogen atom of the PANI chain was selected, and the distance was measured between the center of both atoms. As seen from the figure, there is no effect on the PANI conductivity for a distance 1.5 $\mathring{A}$ and more.

Corresponding I-V characteristics are shown in Fig. 4.34. A conductivity-lowering effect appears when the gas molecule is closer to the chain. This effect has a minimum for distances between 0.9 - 1.0 $\mathring{A}$ - the saturation current for 0.25 V reaches only 4 μA in opposition to PANI without any gas molecule, reaching for the same voltage 14.1 μA. Distances under 0.9 $\mathring{A}$ were not considered because, in this case, the nitrogen atom of NH_3 is very close to the hydrogen atom of NH-binding of the PANI chain.

Then, the local energy minima using molecular dynamics were computed, resulting in the

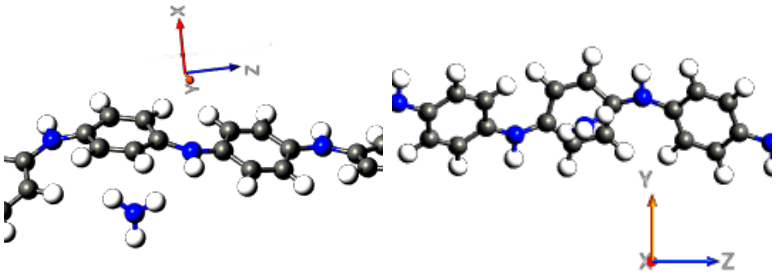

Figure 4.33: One of modeled position and orientation of ammonia molecule: the NH_3 molecule was placed on the axis of the benzene ring and its position and orientation were adjusted through minimum energy optimization. On the left from the point of view of the Y-plane, on the right from the point of view of the X-plane. The Z-plane is the plane of PANI chain length.

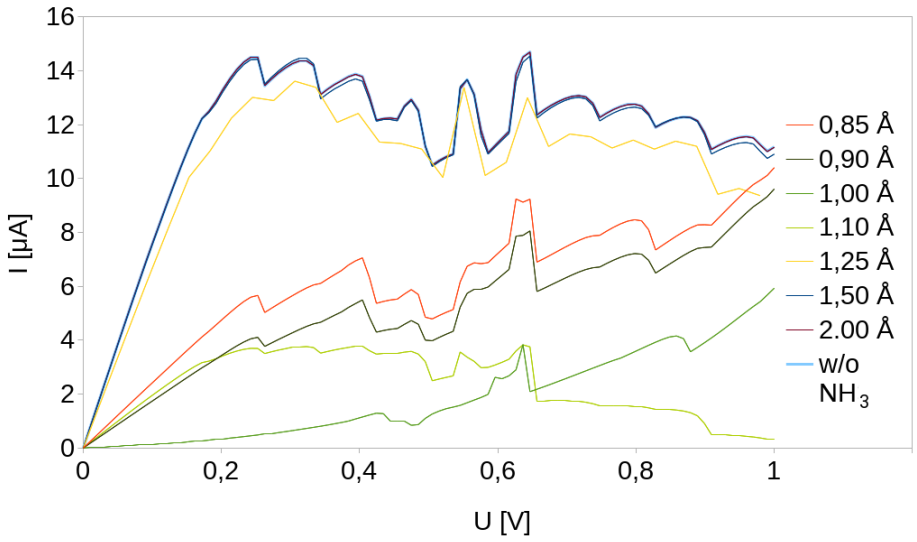

Figure 4.34: The set of I-V characteristics of the PANI chain without NH_3 molecule and for different distances of NH_3 molecule from the PANI chain is not optimized positions according to the Fig. 4.32 a)

ammonia gas molecule's optimized position and orientation. As shown in Fig. 4.35, different slope and asymptotic current values are visible for various ammonia molecule positions and orientations. Comparing the I-V characteristics of the PANI device without the gas molecule (green color) and with the optimized position and orientation of the gas molecule near the doped nitrogen atom (brown) and near the benzene center (light blue), the current value while reaching saturating voltage 0.25 V is for PANI with NH_3 more than 12% lower. Namely, PANI influenced by the optimized NH_3-molecule position near the doped nitrogen atom (the center-center distance of the nitrogen atoms is 1.9$\mathring{A}$) reaches a current of 12.4 μA, similar to PANI influenced by the optimized NH_3-molecule position near a benzene center (the distance of the nitrogen atom to the plane of the benzene center was 4.0$\mathring{A}$), reaching a current of 12.3 μA. Nevertheless, PANI without gas molecule reaches a current of 14.1 μA, see Tab. 4.8.

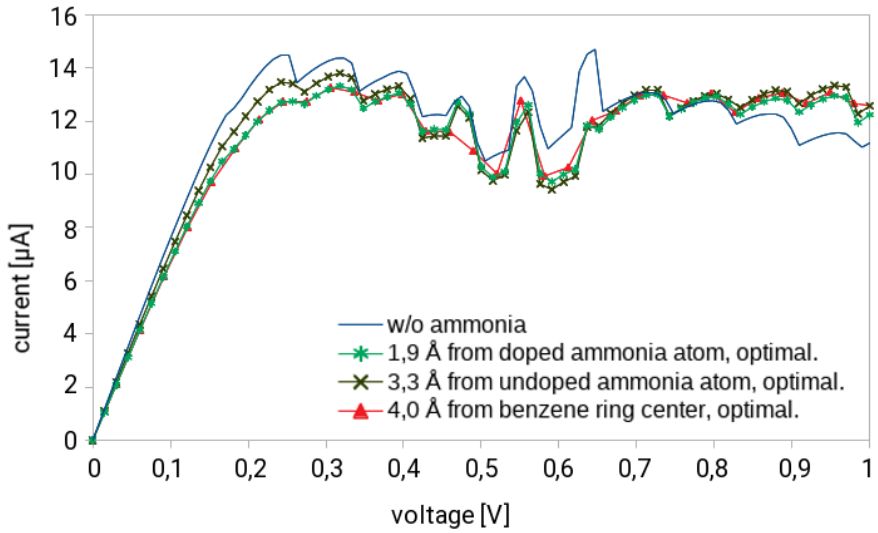

Figure 4.35: The I-V characteristics of PANI computed for PANI chain without ammonia molecule (solid blue line), PANI with the presence of ammonia near the doped nitrogen atom of PANI, optimized, see the position in Fig. 4.32 c) (green with a star), ammonia near the undoped nitrogen atom of PANI, optimized, see the position in Fig. 4.32 d) (black with a cross) and ammonia near the center of the benzene ring of PANI, optimized; see the position in Fig. 4.33 (red with a triangle).

NH_3**-position**	**voltage** $[V]$	**current** $[\mu A]$
without NH_3	0.25	14.1
1.9$\mathring{A}$ from doped N	0.25	12.4
4.0$\mathring{A}$ from ring center	0.25	12.3
1.0$\mathring{A}$ from doped N	0.25	10.5

Table 4.7: Saturation current for various positions of ammonia gas with respect to PANI chain.

As shown before, the numerical data introduced in this study were computed through Extended Hückel Method. To compare this model with real data, the computation conditions are fundamental.

First, the numerical model was computed for only one molecule of defined length (transmission area was 166 $\mathring{A}$ long) Moreover, acting with only one ammonia gas molecule. This condition determines the I-V characteristics strongly. Its slope in the first part of it and the resistance effect of ammonia molecule acting with PANI is based on it. Next, the current saturation occurring in I-V characteristics comes from the fact that only one relatively short chain was computed, meaning there is only a limited amount of charge carriers. Furthermore, the changing slope of the curve in the saturation part of the diagram is based on the Extended Hückel Method, namely, only one-particle ballistic charge carrier transport. Therefore, only the first part of the diagram carries important physical information on PANI resistance. Moreover, its value is influenced by the computed molecule's physical dimensions and surrounding.

Only the linear part of I-V characteristics was considered for data comparison with the

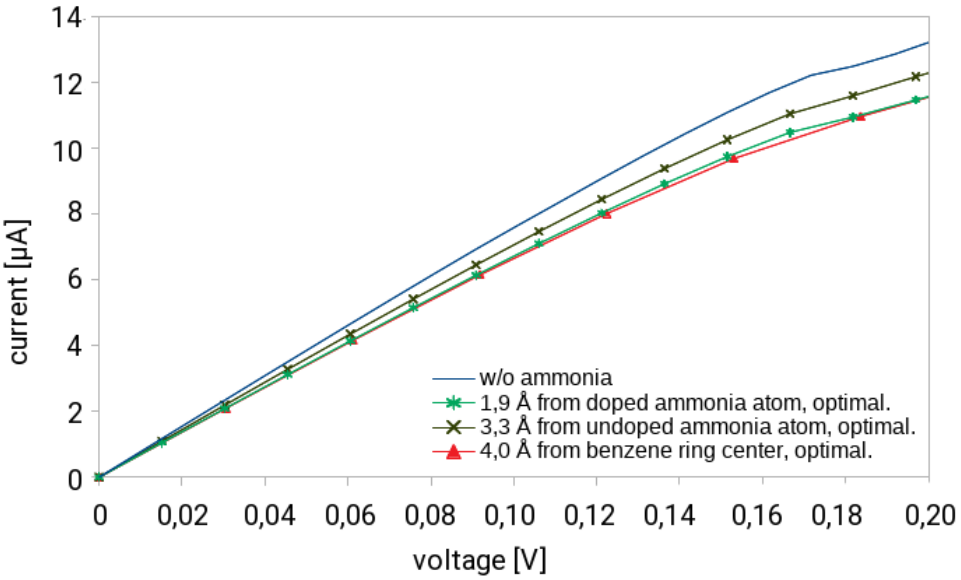

Figure 4.36: A detailed view of I-V characteristics of PANI from Fig. 4.35 - for voltages $0.00 - 0.20$ V, the current rises linearly.

experiment. Next, virtual ammonia gas concentration was computed through ppm (particle per million). Coming from the dimensions of the PANI molecule, in this case, the geometry responds to the concentration of about three ppm. However, as it was discussed here, the real resistance of PANI bulk would be slightly different: a lot of PANI molecules, charge carriers hopping, kinetic effects, inter-carrier influences, and so on.

Comparison with experimental data

A comparison with experimental data was executed to test the reliability of the numerical data presented in this study.

A flexible ammonia gas sensor based on polyaniline as an active sensing thin film layer was produced in [81]. This sensor was built from a thin film deposited on interdigitated electrodes by using the chemiresistive principle. Relative resistance change Res

$$Res = \frac{R - R_0}{R_0} \tag{4.6}$$

was estimated for R_0 electrical resistance of PANI without any gas presence and R electrical resistance of PANI in the presence of ammonia gas.

This ammonia gas sensor from [81] was periodically exposed to synthetic air containing NH_3 of increasing concentrations (10, 20, 30, 40, and 50 ppm) for 20 minutes and then cleared with synthetic air without NH_3 for the next 20 minutes. For experimental data, see Fig.4.37.

From this data, for the sake of this study, saturation values for each gas concentration were fitted. Comparison of these resistance values and the numerical one are depicted in Fig.4.38. This diagram shows that the computed resistance values match the experimental data rather right.

Experimental data for polyaniline acting as NH_3 gas sensor in [68] were also analyzed. Resistance Res was measured for several gas concentrations (25, 50, 75, and 100 pm) and

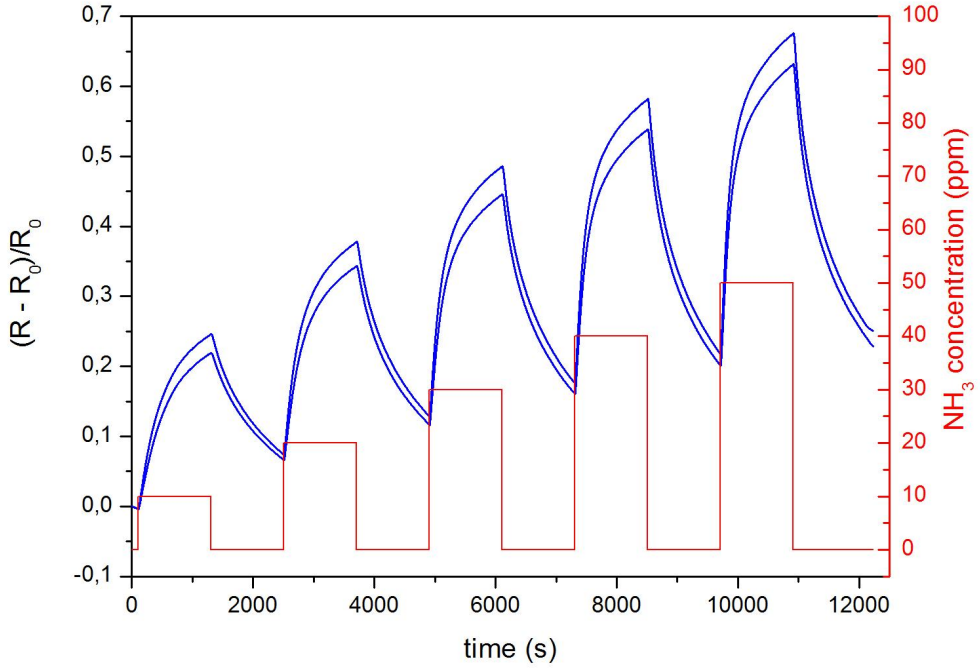

Figure 4.37: Experimental data of resistance $(R - R0)/R_0$ taken with permission from [81].

was compared with computed values from I-V characteristics (as seen in Fig.4.36). The numerical value lies slightly under the linear trend of experimental data; see Fig.4.38. This effect of resistance difference response of the material for the numerical case compared to the experimental one was expected and came from the limitation of computation, as explained before. In the experiment, a PANI sensor, 100 μm wide, consisting of overlaying molecules, sharing their charge carriers and allowing hopping of them, has another condition as the numerical experiment with only one, 166 $\mathring{A}$ long molecule with non-interacting charge carriers. From this point of view, the accuracy of the numerical model is good.

Different linear functions are found comparing two experimental results, Fig.4.38. This mismatch of absolute values come from diverse setups of experiments - different samples with different PANI resistance, which leads to, unlike resistance differences. For PANI as a gas sensor, precise calibration is a must.

4.3.2 One-chain PANI in interaction with more NH_3 and NO_2 gas molecules

This section corresponds to the published article in the Beilstein Journal of Nanotechnology [B]

Nextly, emeraldine salt molecules were modeled for one chain with or without several gas molecules. Every second of nitrogen in the chain was doped. For the gas molecule interacting with the chain, several positions were considered: close to the doped and undoped nitrogen (Fig.4.39), then in the vicinity of the benzene center, and, if more chains are modeled, between two chains (Fig.4.44). The position and the orientation of the gas molecule were considered as well and varied in several fashions. Apart from these variations, one gas molecule position and orientation were chosen utilizing energy-minimizing optimization. Furthermore, for all these situations, a computation of the transmission spectrum proceeded.

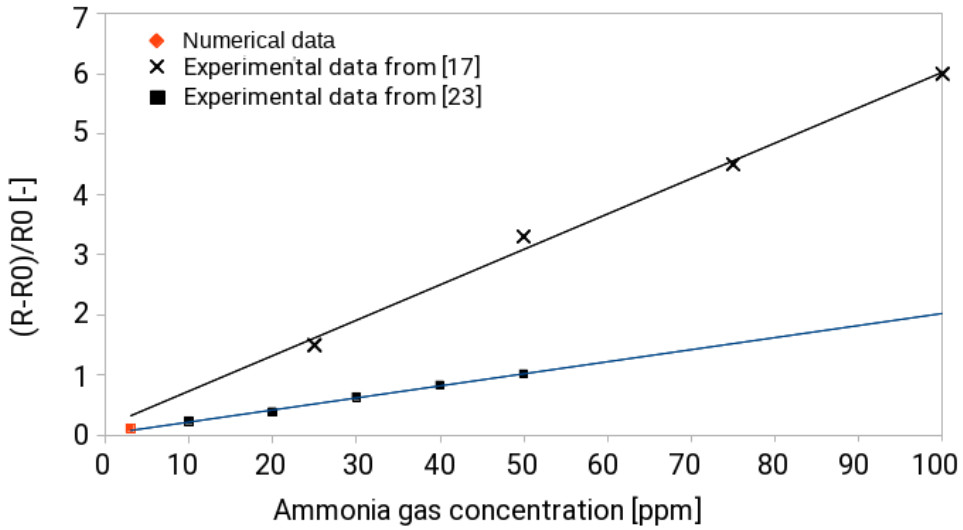

Figure 4.38: Comparison of resistance $(R - R0)/R_0$ for modelled PANI chain and experimental data from [81] and experimental data from [68].

Transmission spectra were used to obtain relevant I-V characteristics.

There was only one molecule chain in the calculation, and only several gas ammonia/nitrogen dioxide molecules affected the PANI molecule. Therefore, the quantity of free charge carriers is limited and even very small compared to macroscopic PANI media. This leads to current saturation. The electric resistance was estimated from the initial linear behavior of I-V characteristics before saturation.

We have chosen the fixed positions of ammonia and nitrogen dioxide molecules. We have computed the local energy minima through molecular dynamics, which results in the optimized position and orientation of the gas molecule. The spatial orientation of the gas molecules was estimated by these optimizations. Next, one or more molecules, up to four, were placed near the chain according to the optimization, and thus either to the doped nitrogen atom (D) or to the undoped one (U). Corresponding resistance values for:

- one gas molecule near the doped nitrogen on the whole chain (1D+0U),
- one gas molecule near the undoped one on the whole chain (0D+1U),
- one gas molecule near the doped and one gas molecule near the undoped nitrogen on one chain (1D+1U),
- one gas molecule near the doped and two gas molecules near each undoped nitrogen on one chain(1D+2U),

were estimated from the I-V characteristics.

Relative resistance change Res

$$Res = \frac{R - R_0}{R_0} \tag{4.7}$$

was estimated for R_0 electrical resistance of PANI without any gas presence and R electrical resistance of PANI in the presence of ammonia or nitrogen dioxide gas, respectively.

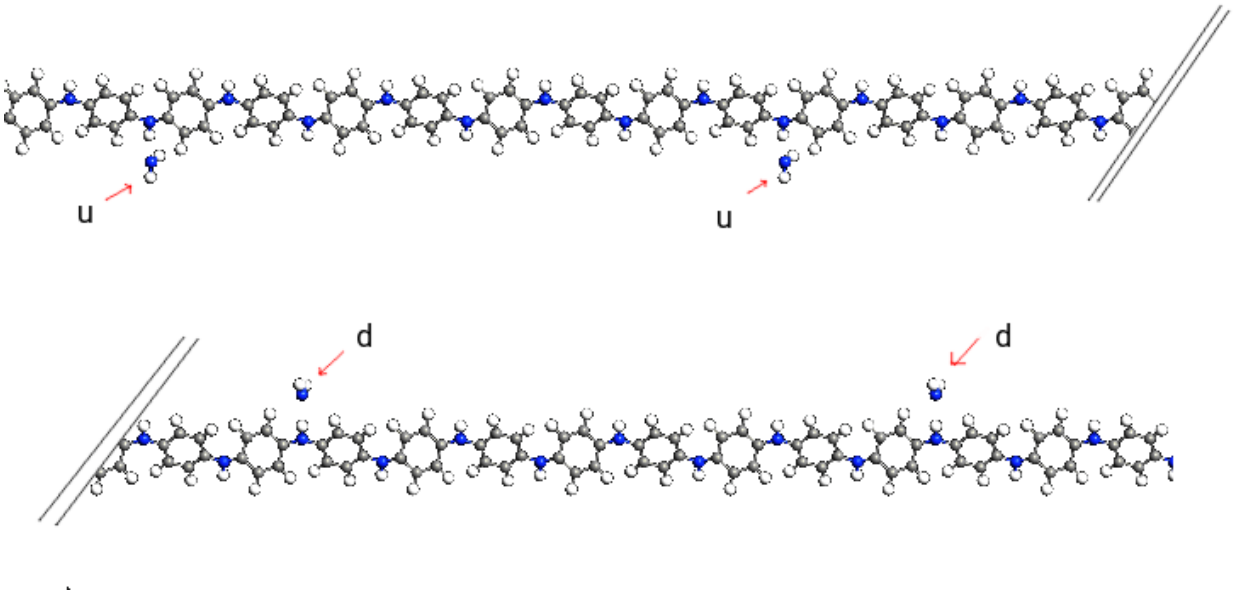

Figure 4.39: One chain PANI and 4 NO_2 molecules. Two in position 'd' (doped) and two in position 'u' (undoped), also 2D+2U.

This relative resistance change for ammonia gas molecules for one chain of emeraldine salt is shown in Fig. 4.40. One can see that the main part of the resistance change is due to the ammonia molecule near the doped nitrogen from the polyaniline chain and that the resistance change of more ammonia molecules on different positions (near the doped/undoped polyaniline nitrogen) is like the sum of the resistance changes of both positions. Further, the resistance grows linearly for the ammonia gas molecule positions.

By the same means, the relative resistance of the polyaniline chain with and without one or more nitrogen dioxide molecules was computed as well. The I-V characteristics were computed for several molecule positions near the doped and the undoped nitrogen atoms; see above; the molecule orientation was estimated through molecular dynamics optimization. The resistance from the linear part of the I-V characteristics was used to estimate the relative resistance, see Eq. 4.7 and was computed for all the sets, see Fig. 4.41.

As for the ammonia, the resistance change depends strongly on the nitrogen dioxide molecule position, a gas molecule near the doped nitrogen makes the polyaniline chain more sensitive than at the undoped position. The resistance change of more nitrogen dioxide molecules in different positions (near the doped/undoped polyaniline nitrogen) rather sums the resistance changes of both positions. The increasing linear resistance change for the gas molecule positions is also seen.

These two one-polyaniline-chain data were recalculated for ppm concentration (3, 6, 9, and 12 ppm, respectively), and we have compared them with experimental data, as seen below.

Limitations and validity of the model

The Extended Hückel Method is semi-empirical and cannot display reality completely. Considering the computational limits is crucial to compare this model with experimental results.

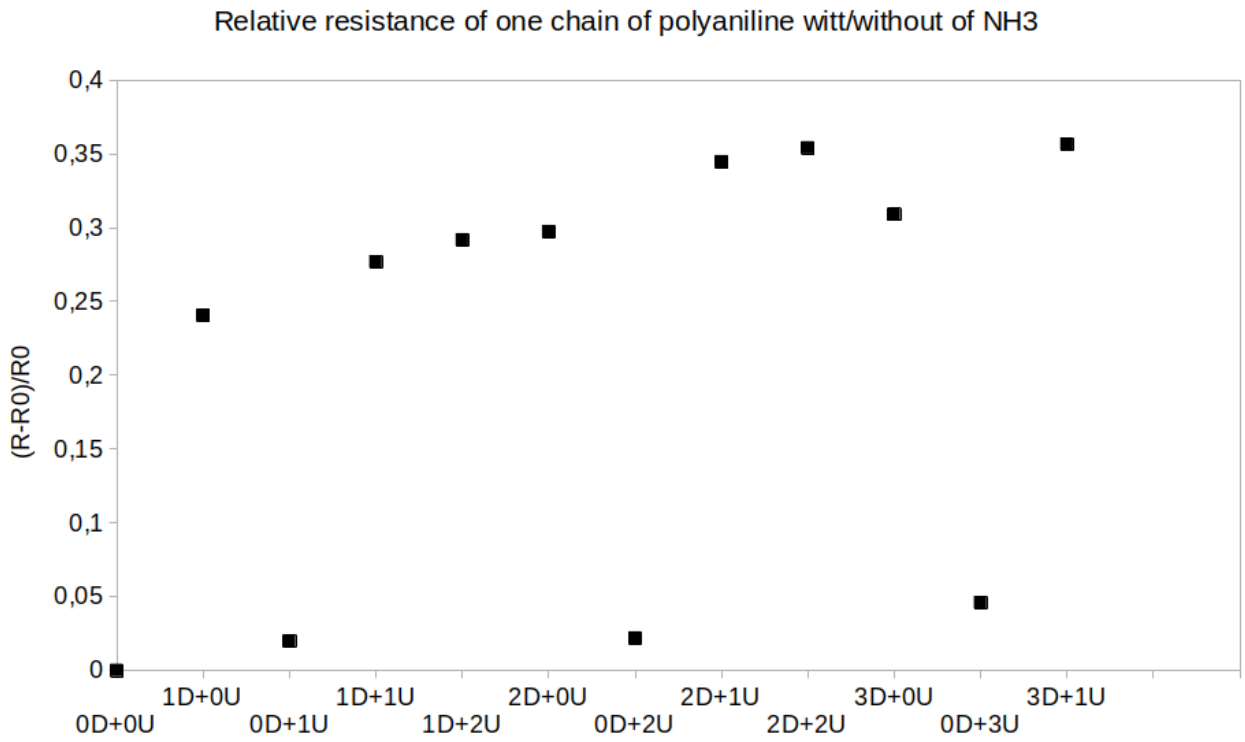

Figure 4.40: The relative resistance change of emeraldine salt - one-chain-molecule was taken into account - by the presence of several ammonia gas molecules near the chain, in the positions as described above.

These molecule models insist on only one or two PANI molecules with a transmission area of 166 $\mathring{A}$; next, they acted with only several gas molecules. These conditions affect the V-A characteristics. They affect its slope and the resistance effect of ammonia/nitrogen dioxide gas on polyaniline. Moreover, the current saturation in V-A characteristics, mentioned before, is based on one or two relatively short chains, which were taken in computation, meaning that only a small, restricted quantity of free charge carriers takes place. Furthermore, as seen in the I-V characteristic, obtained through the Extended Hückel Method, in the saturated part, one particle's ballistic charge career transport takes place. From this point of view, for the relative resistance change data, the initial part of the I-V diagram was only considered. Nevertheless, as well the numerical experiment was taken in the environment of a small region, and therefore, the results are influenced by the limitations of the modeled environment.

The gas concentration in particle per million (ppm) for the numerical experiment was calculated approximately as the next step. In this case, one gas molecule in the device's active area was computed concerning the dimensions of polyaniline polymer to correspond to about three ppm concentration.

Finally, this numerical model only considers a few effects; under others in bulk, a large amount of polymer chains take part; there are kinetic effects, inter-carrier influences, and others. Therefore, physical polyaniline bulk material would have different resistance than the computed model.

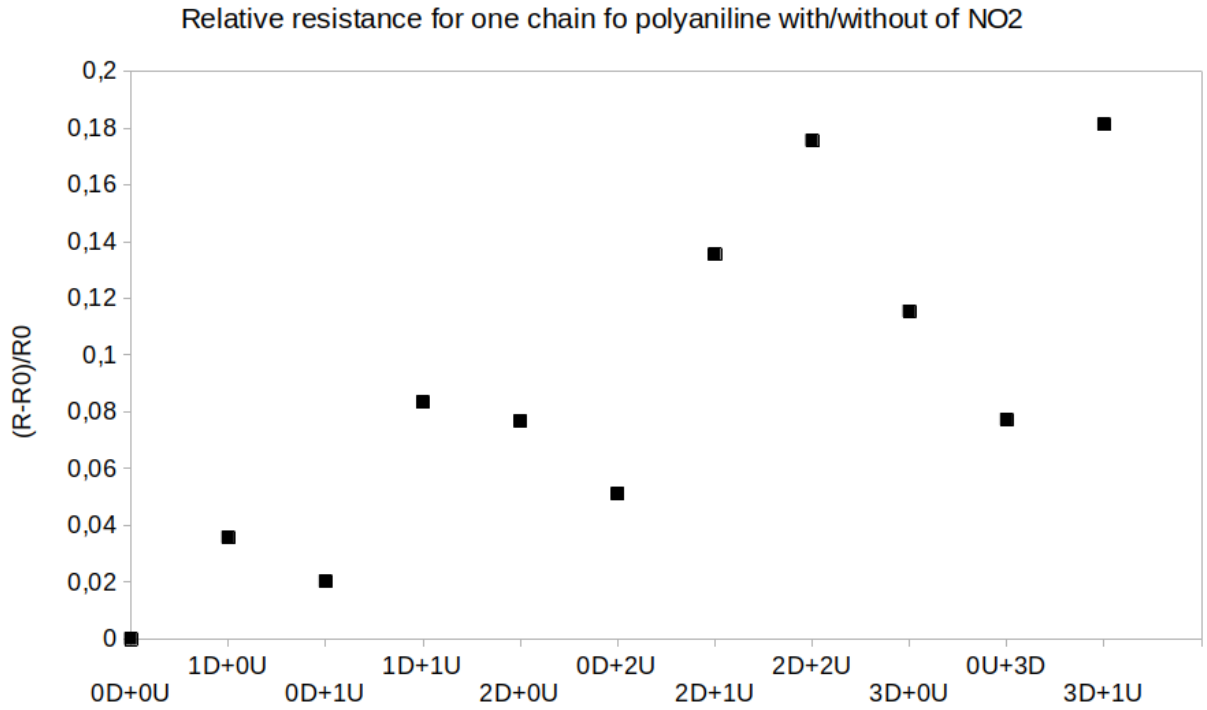

Figure 4.41: The relative resistance change of emeraldine salt - one-chain-molecule was taken into account - by the presence of several nitrogen dioxide gas molecules near the chain, as described above.

Experimental data comparison

For this work, numerical models for a one-chain polyaniline sensor were compared with several experimental data. Gas sensors for ammonia and nitrogen dioxide sustaining from flexible PANI thin film layer sensing area were produced by Posta *et al.* [81] and by Kroutil *et al.* [68]. This chemiresistive sensor is contained in a thin film deposited on interleaved electrodes.

In the experiments of Posta and Kroutil, the gas sensors for ammonia and nitrogen dioxide were exposed for 20 minutes to synthesized air with a given concentration of NH_3 and NO_2, respectively, and then were exposed for the next 20 minutes to clear synthesized air without gases.

The experimental results were fitted for saturated values and compared with computed resistance values - see Fig.4.42 and 4.43. The modeled resistance values of the polyaniline with several gases fit the experimental results rather well.

Comparing both experiments of Kroutil et al. and Posta et al., in Fig.4.42, unlike linear dependencies are found. The mismatch of the absolute values comes from the diversity of the experimental setups - using different samples with different polyaniline resistance leads to unequal resistance differences.

The numerical values of NO_2 at Fig. 4.43 have slightly stronger slopes than the linear trend of the experimental data. This effect yields from the limitation of the numerical model, as explained before. In the experiment, the PANI sensor 100 μm wide and overlaying molecules contributed to the conductivity, sharing their charge carriers and allowing hopping. In contrast, the numerical experiment consisted of only one 166 $\mathring{A}$ long molecule with

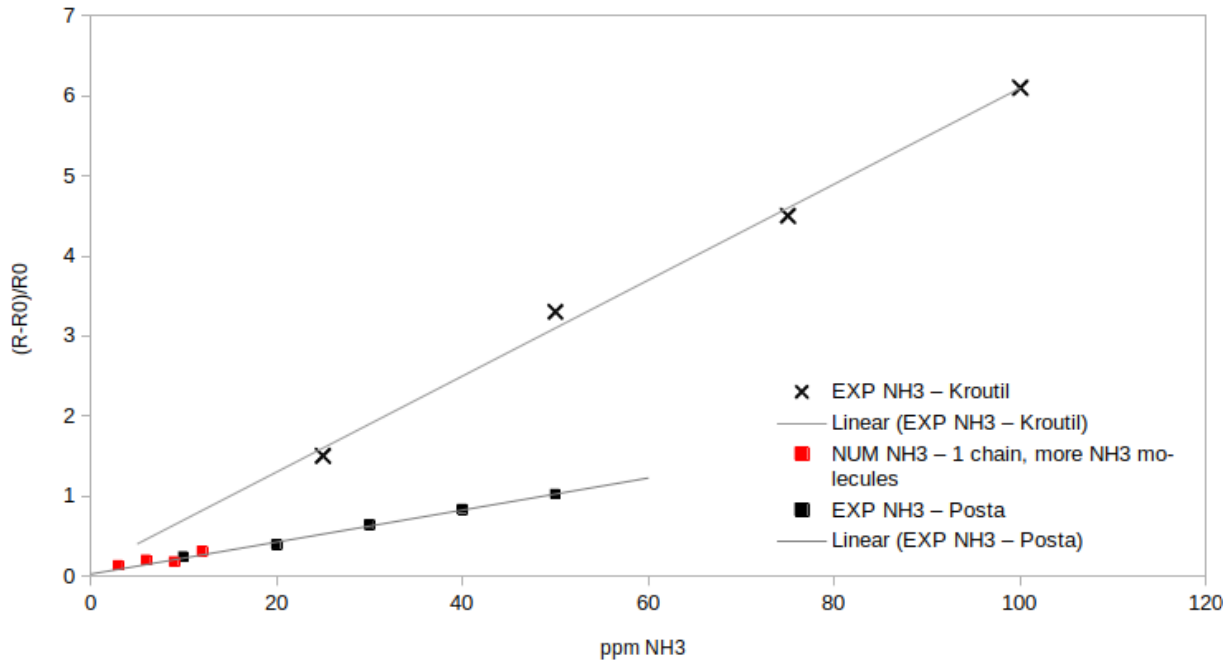

Figure 4.42: Relative resistance of nitrogen dioxide for several concentrations - red squares: computation, black crosses: experimental data [68], black squares: experimental data [81]

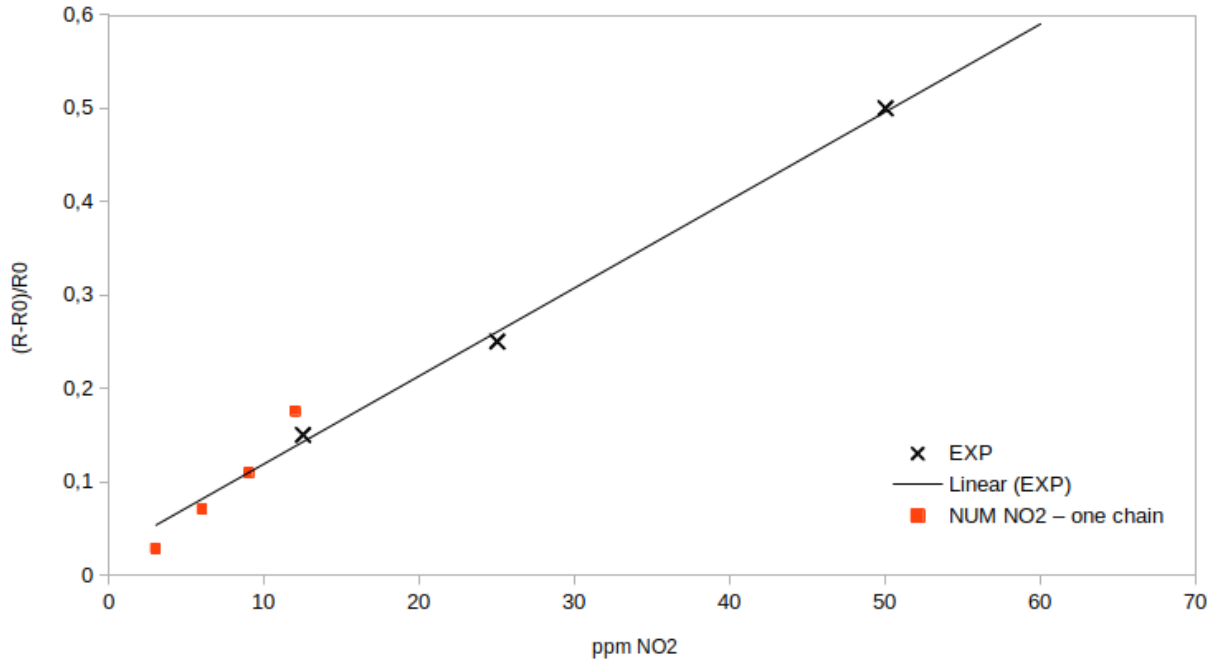

Figure 4.43: Relative resistance of nitrogen dioxide for several concentrations - red squares: computation, black crosses: experimental data [68]

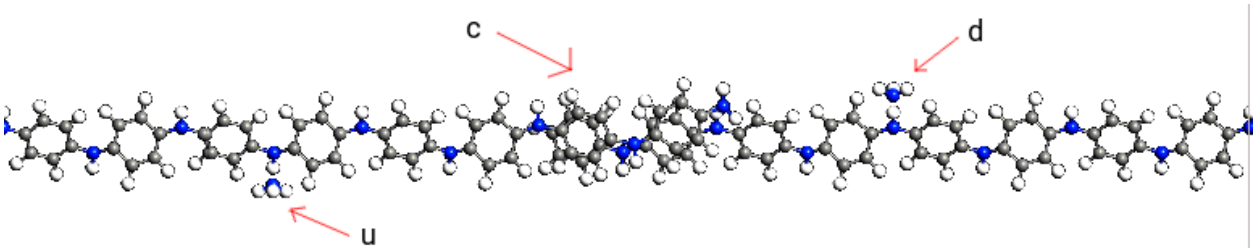

Figure 4.44: PANI two chains, overlapping in the middle (c) with distance gap of $3\mathring{A}$. There is position (c) for ammonia or nitrogen dioxide molecules. Further positions are doped (d) and undoped (d) with ammonia molecules.

non-interacting charge carriers. Considering these limitations, the agreement between the experiment and the numerical model is good.

4.3.3 More chain polyaniline in interaction with NH_3 and NO_2

This section corresponds to the published article in the Beilstein Journal of Nanotechnology [B]

As a next step, sets with two chains of polyaniline were calculated. With or without several gas molecules, this two-chain model has every second of nitrogen in the chain doped. Several positions were considered for the gas molecule interacting with the chain: close to the doped and undoped nitrogen, in the vicinity of the benzene center, and between two chains (Fig.4.44). In this experiment,

- no NH_3 gas molecule,
- one NH_3 gas molecule by the doped nitrogen (1D+0U+0C),
- one NH_3 gas molecule near the undoped nitrogen(0D+1U+0C),
- one NH_3 molecule between the chains in the central benzene circle region (see Fig. 4.45), (0D+0U+1C),
- and their combinations

were placed into the model. The relative resistance was estimated for one chain with ammonia and nitrogen dioxide above. There were only two molecule chains in the calculation, and only several gas ammonia/nitrogen dioxide molecules are affecting the PANI molecule, therefore the number of free charge carriers is limited and even very small in comparison with macroscopic PANI media. This leads to current saturation. The electric resistance was estimated from the initial linear behavior of I-V characteristics before saturation.

The effect of a discontinued polyaniline chain was studied as a first step. The gap between two chains was estimated using molecular dynamics - by looking for energy minima and yields in the distance about 3 $\mathring{A}$. The I-V characteristics were computed and compared with one-chain results for this geometry. From the linear part of this characteristic, the resistance and, thus, the resistance change concerning the one-chain case was computed. Next, the same geometry with one gas molecule was computed. The resistance change results are displayed in Fig. 4.46.

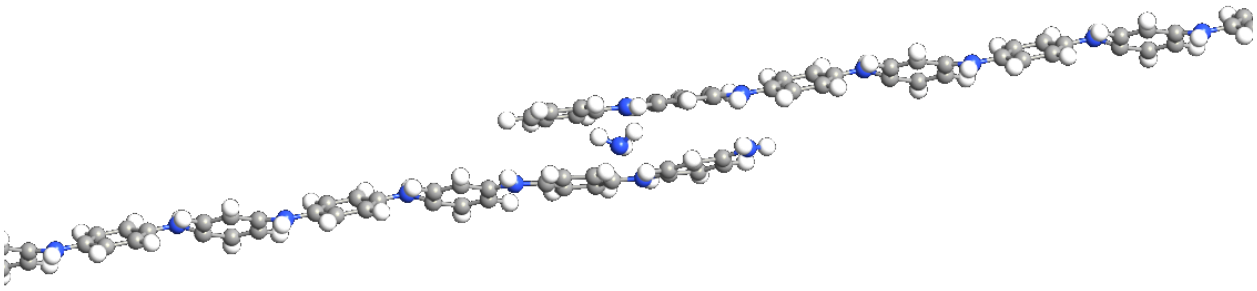

Figure 4.45: PANI two chains, overlapping in the middle with distance gap of $3\mathring{A}$, top view. Between the chain is located one ammonia molecule.

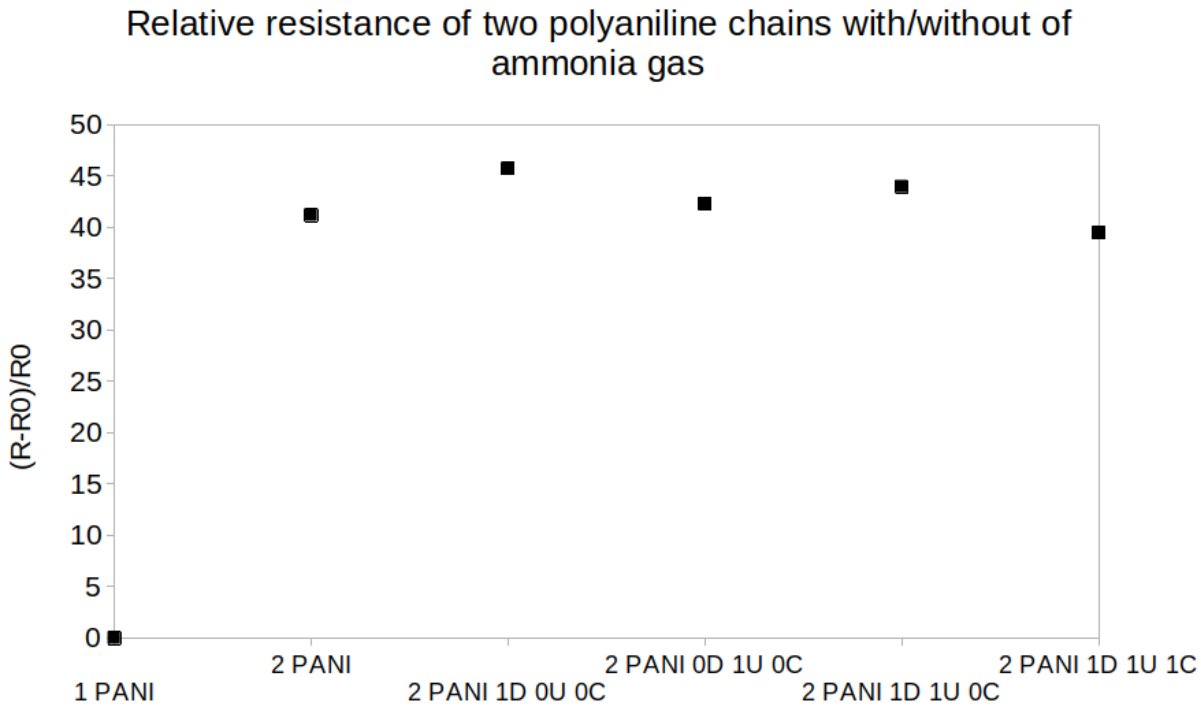

Figure 4.46: Relative resistance of emeraldine salt in the presence of NH_3 computed for two overlapping chains of polyaniline, see Fig. 4.45. The reference value for one polyaniline chain without any gas molecule is on the left.

As visible in the figure, the hopping resistance change is rather large compared to the resistance change due to the ammonia gas molecule presence. However, one can also see the ammonia gas molecule's effect. The resistance rise is higher for the ammonia position near the doped polyaniline nitrogen and lower at the undoped position.

Limitations and validity of the model

The Extended Hückel Method is semi-empirical and cannot display reality completely. Considering the computational limits is crucial to compare this model with experimental results.

These molecule models insist only on one or two PANI molecules with a 166 $\mathring{A}$ transmission area. Following, they acted with only several gas molecules. These conditions affect the V-A characteristics. They affect its slope and the resistance effect of ammonia/nitrogen dioxide gas on polyaniline. Furthermore, the current saturation in V-A characteristics, mentioned before, is based on one or two relatively short chains, which were taken in computation, meaning that only a small, restricted quantity of free charge carriers takes place. Moreover, as seen in the I-V characteristic, obtained through Extended Hückel Method, one particle's ballistic charge career transport takes place in the saturated part. From this point of view, for the relative resistance change data, the initial part of the I-V diagram was only considered. However, the numerical experiment was also taken in the environment of a small region, and therefore the results are influenced by the limitations of the modeled environment.

The gas concentration in particle per million (ppm) for the numerical experiment was calculated approximately as the next step. In this case, one gas molecule in the device's active area was computed concerning the dimensions of polyaniline polymer to correspond to about three ppm concentration.

Finally, this numerical model needs to take more effects into account. Under others that in bulk a big amount of polymer chains take part, there are kinetic effects, inter-carrier influences, and others. Therefore, physical polyaniline bulk material would have different resistance than the computed model.

4.3.4 Effect of dilutant on NH_3 sensoring

This section corresponds to the published article in the IEEE Sensor Letters [C]

Recently, experiments with ammonia gas sensors based on polyaniline have shown such resistance changes as well [81], [68]. In Kroutil et al. [68], the polyaniline gas sensor set-up was measured experimentally for several gases, including NH_3, and in the previous chapter, a numerical model of the ammonia sensor was made, which showed good accordance with the experimental data, see Chap. 4.3.

However, the sensors from other research show different sensibility. Therefore, gas sensor preparation can affect the sensor's sensibility, among other effects. As already said, emeraldine salt can be prepared using several dilutants (HCl, H_2SO_4), and this paper studies the effect of this dilutant on the end-produced polyaniline and its sensitivity towards ammonia.

In this chapter, the electrical conductivity of PANI molecules with ammonia gas molecules under the condition one of the dilutant HCl and H_2SO_4 will be studied utilizing numerical modeling.

Numerical model

Computation in this chapter was done by Synopsis QuantumATK ver. 2020.09 [34], using the benchmark results in Chap. 2.8.

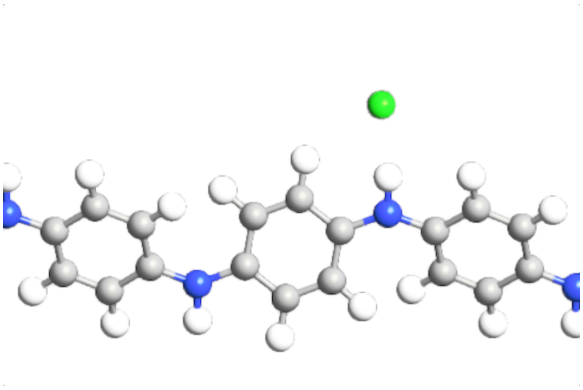

Figure 4.47: PANI chain and one Cl^- ion from HCl in optimized position.

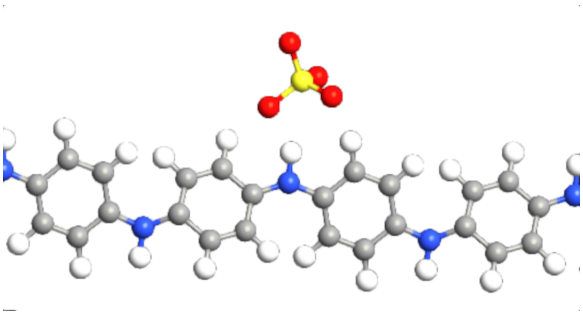

Figure 4.48: PANI chain and one SO_4^{2-} ion from H_2SO_4 in optimized position.

For the study, a 32-mer molecule as a basic device was chosen [82]. With this physically meaningful PANI model, I-V characteristics of PANI devices with and without the presence of dilutants HCl and H_2SO_4 were studied, and three types of the device were modeled:

- pure 32 mer PANI chain (see Fig. 3.2),
- 32 mer PANI chain and one Cl^- ion coming from the hydrochloric acid (see Fig. 4.47),
- and 32 mer PANI chain and one SO_4^{2-} ion coming from the sulfuric acid (see Fig. 4.48).

Coming from the dimensions of the simulated PANI molecule, the geometry with one molecule of HCl and H_2SO_4, respectively, corresponds to a concentration of about three ppm. The position of the ions was optimized through molecular dynamics.

Results

The I-V characteristics were computed for all of the device constellations described above (pure PANI, PANI with Cl^- ion, and PANI with SO_4^{2-} ion). As can be seen from the results (Fig. 4.49), the current difference is for these voltages minimal, and the curves lie almost over each other. However, the curves are not identical - the curve of HCl lies slightly lower than that of pure PANI, and the curve of H_2SO_4 lies lower than the HCl curve. Therefore, a small resistance difference occurred.

To make the I-V characteristic data more clear, from the I-V characteristics of PANI chain (pure, with HCl, and with H_2SO_4, see Fig. 4.49) the current differences were computed. From the nature of the computation (limited number of charge carriers), unlike in a real

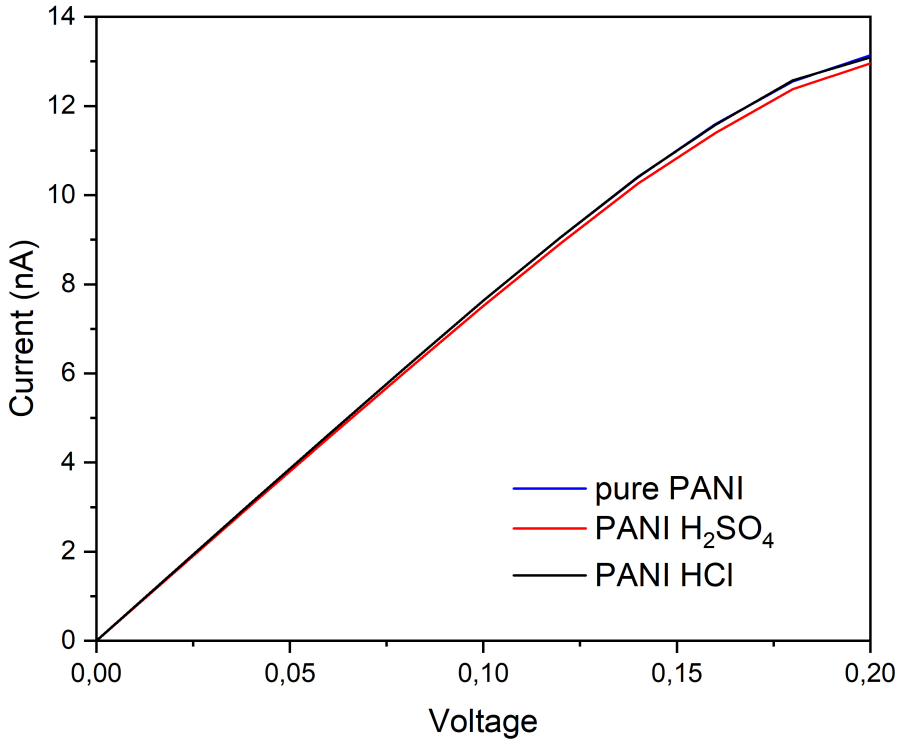

Figure 4.49: I-V characteristics of PANI chain (pure, with HCl and with H_2SO_4), current given in μA.

Table 4.8: Resistance of PANI chain with dilutants in a concentration of 3 ppm.

	R / $k\Omega$	$\frac{R-R_0}{R_0}$
pure PANI	13.094	
PANI w. HCl	13.095	0.008 %
PANI w. H_2SO_4	13.295	1.54 %

experiment, in a numerical experiment, a current saturation occurs. Therefore only the linear part of the diagram is further considered. The current I_{pure} corresponds to the current of pure PANI, I_{HCl} to the current of PANI with hydrochloric acid, and I_{H2SO4} the current of PANI with sulfuric acid. The figure 4.50, the relative current changes to pure polyaniline are depicted.

For the given hydrochloric and sulfuric acid concentrations of 3 ppm, the resistance from the slope of the I-V characteristics was computed. As can be read in the table Tab. 4.8, the resistance for PANI in dilutant presence rises. Nevertheless, the growth is small - in the case of hydrochloric acid, as small as 1 per mille, and in the case of sulfuric acid, below 2 percent.

Discussion

This numerical experiment was computed only for 1 PANI molecule and one "pollution" ion of Cl^- or SO_4^{2-}, respectively — only a small concentration of 3 ppm and minimal current

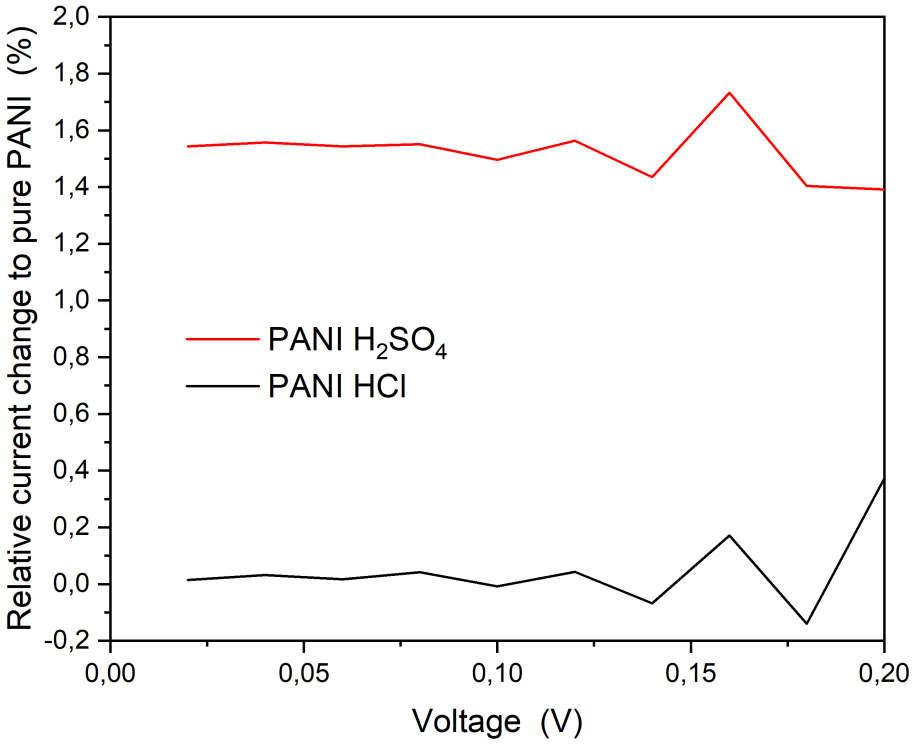

Figure 4.50: Relative current change of PANI with HCl and H_2SO_4 respectively, to pure PANI in %.

Table 4.9: PANI ammonia gas sensor sensitivity compared with PANI dilutant effect - relative resistance change for PANI with target ion and without it per ppm in percent

	$\Delta R/R_0$ per ppm in %
PANI sensing NH_3 Kroutil et al. [68]	6.00
PANI sensing NH_3 Posta et al. [81]	2.00
PANI sensing NH_3 numerical model [83]	1.71
PANI pure vs. PANI polluted w. H_2SO_4	0.51
PANI pure vs. PANI polluted w. HCl	0.002

differences in units up to hundreds of nA. Of course, such a small current would be difficult to measure in real life, and it would be difficult to discern it in the noise and other effects, like structural parameters of the sensor (electrodes, geometry, structure of the sensing layer, and others). The effect is negligible in the case of the rest of Cl^- ions. Nevertheless, we would like to emphasize the relative resistance change as in Table 4.9 - for higher dilutant concentrations, the relative resistance growth of about 0.5 % per ppm caused by sulfuric acid ions would be already measurable. So the sulfuric ions can make the sensor more insulating than needed, which can affect the sensor sensibility (by lowering its measurement range). However, this effect will still be measurable only for rather more polluted sensors than three ppm.

From the results, the sensor preparation shall be proceeded precisely, especially when washing the polymerizing mass with sulfuric acid. When this condition is not met, it can

lead to lowered sensor conductance and, thus, lowered sensibility to targeted gases. This effect may be why the different experiments lead to different sensor resistance; every sensor has to be calibrated precisely.

5. Conclusion

This thesis aims to analyze the function of various sensors, such as zinc oxide, graphene, and polyaniline, and their strengths and weaknesses, with the possibility of predicting their properties through numerical modeling. The numerical experiments proved that certain materials, like graphene and polyaniline, could be accurately studied through numerical analysis, reducing the need for time-consuming physical experiments. The study also showed that the choice of software is crucial for calculating nanoscale devices like gas sensors. QuantumATK from Synopsys was used in this study to model zinc oxide, graphene, and polyaniline devices with gas molecules. The results were compared with experimental data, providing important insights into the materials' behavior.

The study found that modeling ZnO sensors is challenging due to microstructure differences and the grain boundary effect, which is essential in the current growth with growing voltage. The models for graphene structures showed that the conductance is coupled with distortions, and the highest current growth has the tiniest graphene geometry. The study also found that PANI emeraldine salt can detect NH_3 and NO_2 in the air, and the relative resistance change caused by these gases is much lower. The study also analyzed the effect of dilutant pollution on PANI gas sensors and found that hydrochloric acid could be more suitable for PANI gas sensor preparation than sulfuric acid.

In detail, this thesis focused on the numerical modeling of nanostructures, specifically zinc oxide, graphene nanoribbons of width W=3, W=8, graphene nanosheets, and polyaniline, in their interactions with various gas molecules such as ammonia, nitrogen dioxide, and carbon monoxide. This work emphasizes the importance of choosing the appropriate software for calculating nanoscale devices like gas sensors. An overview of different nanostructure modeling software and packages was given, and the commercial software QuantumATK from Synopsys was used in this thesis.

The study utilized QuantumATK to compute the benchmark of the desired geometry with a zinc oxide device with zinc electrodes and graphene and polyaniline molecules without electrodes, which yielded relevant information about reliable numerical geometry to be chosen for the numerical experiments. The targeted materials acted with one or more gas molecules and the I-V characteristics were computed.

The electrical resistance of zinc oxide was computed using the LCAO method (LDU + U scheme). Graphene and chosen polyaniline variation, emeraldine salt, were calculated using semiempirical methods, all by the QuantumATK software. Transmission spectra and the I-V characteristics were obtained, and the change in relative resistance for various gas molecules, their position, orientation, and concentration, was calculated using those characteristics.

Finally, the obtained results were compared with experimental data from [79], [81], and from [68], which demonstrated the accuracy of the numerical modeling approach.

The numerical experiment showed that modeling zinc oxide sensors is challenging due to microstructure differences. The sensitivity of zinc oxide to ammonia was about six times lower in the numerical model than in the experiment, indicating that the numerical computation underestimates the material response. It is essential to note that the real ZnO bulk would be different from the numerical device as the modeled material was monocrystalline, whereas, in real life, ZnO is polycrystalline. Furthermore, kinetic effects, inter-carrier influences, and grain boundary conductance play a crucial role in the current growth with growing voltage, which was not included in the numerical model. Thus, the numerical model needs improvement, but it still demonstrated that the zinc oxide material reacts to NH_3 gas

molecules, with its sensitivity to ammonia having a mixed background of one-sixth influenced by pure ZnO material and five-sixths by other effects like grain boundary conductance.

The numerical modeling of graphene structures showed that the highest current growth had the tiniest graphene geometry, whereas the lowest current growth had the infinite nanolayer. The study found that the conductance is coupled with distortions in the graphene layer edge, and the armchained geometry had a higher response to disturbances than the zig-zag geometry. The W3 nanoribbon showed the most gas response where the gas molecules were positioned on the edge. However, the W8 nanoribbon showed high sensitivity to gases settled near its surface (NO_2 and CO) compared to NH_3 without affecting the current change. The pristine infinite graphene nanosheet showed no sensitivity to gases near its surface, and the most sensitivity was proven for NO_2 and the lowest for CO for all graphene sensor devices. These results provide important insights into the behavior of materials and pave the way for further numerical modeling of similar gas sensor materials while reducing the need for time-consuming physical experiments and improving the preparation and quality of gas sensors, especially PANI materials.

This thesis involved a core part numerical modeling of one or more polyaniline (PANI) chains, and several models were introduced for emeraldine salt with and without gas molecules, such as ammonia and nitrogen dioxide. From these I-V characteristics of emeraldine salt molecules in several configurations, including hopping, the relative resistance $(R - R_0)/R_0$ was computed, and then the comparison with data retrieved experimentally by [81] and [68] was proceeded. These one-chain and two-chain systems provide data about the importance of the gas molecule position concerning the conducting chain, the contribution of hopping effects for the conductivity, and how far the resistance depends on the geometry of the polymer molecule.

One pure PANI molecule reaches a saturation current of 14.1μA at 0.25 V. In the presence of the studied gas, NH_3, the saturation currents are 12.3 - 12.5 μA. This value is 12 - 13 % lower than the saturation current of pure PANI. The resistances of PANI with and without ammonia gas presence were calculated from the linear part of I-V characteristics. These resistance values were computed for an approximative ammonia gas concentration of 3 ppm and were compared with experimental data. The numerical and experimental data showed good consistency.

The relative change of emeraldine salt conductivity was found for pure polyaniline (PANI) and PANI with adsorbed ammonia and nitrogen dioxide molecules corresponding to approximative gas concentrations of 3, 6, 9, and 12 ppm. The two-chain model proceeded with only one gas molecule, and thus, the concentration was not varied.

First, the system's resistance with the adsorbed NH_3 and NO_2 molecules rises. The discontinuity has the main effect of resistance growth, much smaller but still significant is the relative resistance growth for the system with the ammonia molecule compared to the system without ammonia, where the largest effect was found for ammonia molecules placed near the doped nitrogen atom from the emeraldine salt chain. The presence of nitrogen dioxide molecules has a smaller impact on resistance rise. Nevertheless, like for ammonia, the resistance change depends strongly on the nitrogen dioxide molecule position: a gas molecule near the doped nitrogen makes the polyaniline chain more resistant and sensitive than at the undoped position, and the resistance change of more nitrogen dioxide molecules on different places (near the doped/undoped polyaniline nitrogen) rather sums the resistance changes of both positions.

The relative resistance rises for a one-chain system, and several gas molecules were set compared to experiments for NH_3 and NO_2, and the values are comparable. The values

fit the experimentally gained resistivities well. Polyaniline emeraldine salt seems usable for detecting NH_3 and NO_2 in the air, although the resistance change caused by this gas is much lower.

Finally, polyaniline variety emeraldine salt was studied as an ammonia gas sensor in the presence of hydrochloric and sulfuric acid ions, present in the sensor as a residue of the dilutant used in the production. The dilutant residue concentration corresponded to 3 ppm. The resulting I-V characteristics of PANI polluted by acid ions lie slightly below the values of pure polyaniline. Hence the dilutant pollution leads to an increase in PANI resistance. While the resistance of a PANI ammonia gas sensor in the presence of target gas grows, a sensor with low initial resistance is suitable. The effect of the dilutant residue is therefore disadvantageous even though it is only small: for Cl^- ion for fewer than 0.1 % only, for SO_4^{2-}, the resistance increased by about 1.5 %. These resistance changes are, in this concentration, rather small. Therefore, small dilutant pollution of polymerized emeraldine salt is not of concern, especially in the case of hydrochloric acid. On the other hand, pure production of PANI gas sensors is still necessary because higher pollution, especially sulfuric acid, would negatively affect the device's sensitivity. Results show that hydrochloric acid could be more suitable for the PANI gas sensor preparation than sulfuric acid.

Regarding the thesis goals fullfilment:

1. The first goal, which was to test the ability of the simulation models to describe the electrical characteristics of resistive gas sensors based on different nanostructures and detected gases, was achieved by using the chosen atomistic simulation system, Synopsys Quantum ATK. The study showed that the numerical model effectively predicted V-I characteristics for well-described materials, such as graphene, and physically simple structures, such as polyaniline. However, the numerical experiment could not achieve the desired sensitivity for the bulk semiconductor ZnO because it omitted important features, such as the grain boundary effect in the case of the nanoparticle structure of the film.

2. Therefore, the PANI structure was chosen to compare the simulation results with the experimental data. Good agreement was obtained, as reported in the publication in Physica E: Low-dimensional Systems and Nanostructures [A]. Thus, the second goal was fulfilled.

3. Finally, the third objective was achieved by simulating the more complex PANI structure, which consists of two separate polymer wires connected by the hopping mechanism. The results have been published in the Beilstein Journal of Nanotechnology [B]. The improvement of the polyaniline preparation process was enabled by the simulation in the presence of two different acids used in the PANI polymerisation process. Based on these results, the study recommends considering the impact of dilutant contamination on the sensitivity of gas sensors using emeraldine salt. This result has been published in IEEE Sensor Letters [C].

Contrary to graphene nanoribbons, whose simulations have appeared frequently in the literature in recent years (due to the existence of good numerical models adapted to the given situation), simulations of PANI are rarely published, due to the greater generality of the physical nature of such a model. The articles published so far tend to deal with the analysis of the properties of PANI itself, or the simulation of sensory layers of PANI in combination with other materials, basically without comparison with experimental results. Only the article by Ullah et al. [13] from 2013 talks about comparing the results of the simulation of the interaction of PANI with CO, CO_2 and NH_3 with the experiment, but compared to the work presented in this thesis it is only a general observation of the trend. Ullah states that PANI interacts best with NH_3, which is in agreement with the experimental results, but without any relation to the order of magnitude estimate of the given sensitivity. Thus, in comparison to the work published so far, this work presents a direct quantitative comparison of the sensitivity of the sensor calculated numerically and measured in vivo. This is the main contribution of this work in the field of numerical modelling of gas sensor nanostructures. In addition, this work provides a comparison of the numerical model with the experiment, even for more complex, multiple chains, which has not been published elsewhere. Furthermore, the thesis provides insight into the influence of the fabrication process on the sensitivity of the sensor. This is also not present in other existing literature.

In summary, the scientific contribution of this thesis is a new insight into the potential of numerical modelling for different sensors, such as zinc oxide, graphene and polyaniline, for gas sensing applications, allowing more efficient design and production of sensors. The interaction with multiple PANI chains and the effect of chemical synthesis of PANI on sensor properties has not been published by any previous study, let alone a quantitative comparison with experimental data. The numerical modelling approach proved to be effective in predicting the behaviour of materials and reducing the need for time-consuming physical experiments. Furthermore, it is recommended to consider the effect of dilutant contamination on the sensitivity of gas sensors using emeraldine salt.

The future plan of this research is to improve the numerical model for ZnO sensors by including important features such as the grain boundary effect. Additionally, further numerical modeling of similar gas sensor materials could be conducted to improve the preparation and quality of gas sensors. Finally, the impact of dilutant pollution on the sensitivity of gas sensors utilizing emeraldine salt could be further explored to improve the physical experiments.

References

[1] Mariane A. Franco, Patrick P. Conti, Rafaela S. Andre, and Daniel S. Correa. A review on chemiresistive zno gas sensors. *Sensors and Actuators Reports*, 4:100100, 2022.

[2] N.E. Agbor, M.C. Petty, and A.P. Monkman. Polyaniline thin films for gas sensing. *Sensors and Actuators B: Chemical*, 28(3):173–179, 1995.

[3] Mistutoshi Hirata and Liangyan Sun. Characteristics of an organic semiconductor polyaniline film as a sensor for nh3 gas. *Sensors and Actuators A: Physical*, 40(2):159–163, 1994.

[4] Ilaria Fratoddi, Iole Venditti, Cesare Cametti, and Maria Vittoria Russo. Chemiresistive polyaniline-based gas sensors: A mini review. *Sensors and Actuators B: Chemical*, 220:534–548, 2015.

[5] V. M. Aroutiounian. Zinc oxide gas sensors. *J. Contemp. Phys.*, 55:323–333, 2020.

[6] M. Spasenović, S. Andrić, and T. Tomašević-Ilić. Graphene-based chemiresistive gas sensors. In *2021 IEEE 32nd International Conference on Microelectronics (MIEL)*, pages 25–28, 2021.

[7] Yung Cheng Wong, Bee Chin Ang, A. S. M. A. Haseeb, Aainaa Aqilah Baharuddin, and Yew Hoong Wong. Review—conducting polymers as chemiresistive gas sensing materials: A review. *Journal of The Electrochemical Society*, 167(3):037503, sep 2019.

[8] Rajesh Kumar, O. Al-Dossary, Girish Kumar, and Ahmad Umar. Zinc oxide nanostructures for no2 gas–sensor applications: A review. *Nano-Micro Letters*, 7:97–120, 2015.

[9] Rajesh Ghosh, Mohammed Aslam, and Hemen Kalita. Graphene derivatives for chemiresistive gas sensors: A review. *Materials Today Communications*, 30:103182, 2022.

[10] Golnoush Zamiri and A. S. M. A. Haseeb. Recent trends and developments in graphene/conducting polymer nanocomposites chemiresistive sensors. *Materials*, 13(15), 2020.

[11] Juanito Raphael F Foronda, Lugas Gada Aryaswara, Gil Nonato C Santos, Swathi NV Raghu, and Muhammad Akhsin Muflikhun. Broad-class volatile organic compounds (vocs) detection via polyaniline/zinc oxide (pani/zno) composite materials as gas sensor application. *Heliyon*, 9(2), 2023.

[12] Qiuhua Liang, Junke Jiang, Xiang Sun, Miao Cai, Yiping Huang, Daoguo Yang, Xianping Chen, and Tianling Ren. Molecular modeling design of polyaniline as carbon dioxide sensor. In *2015 16th International Conference on Electronic Packaging Technology (ICEPT)*, pages 148–152, 2015.

[13] Habib Ullah, Anwar-ul-Haq Ali Shah, Salma Bilal, and Khurshid Ayub. Dft study of polyaniline nh3, co2, and co gas sensors: Comparison with recent experimental data. *The Journal of Physical Chemistry C*, 117(45):23701–23711, 2013.

[14] Deepak Punetha, Rashmi Ranjan, and Saurabh Kumar Pandey. Numerical modeling and performance analysis of zinc oxide (zno) thin-film based gas sensor. *AIP Conference Proceedings*, 1966(1):020008, 05 2018.

[15] Fatemeh Mollaamin and Majid Monajjemi. Graphene-based resistant sensor decorated with mn, co, cu for nitric oxide detection: Langmuir adsorption & dft method. *Sensor Review*, 2023.

[16] Sadanand Pandey. Highly sensitive and selective chemiresistor gas/vapor sensors based on polyaniline nanocomposite: A comprehensive review. *Journal of Science: Advanced Materials and Devices*, 1(4):431–453, 2016.

[17] Wei Wei, Wei Li, and Lili Wang. High-selective sensitive nh3 gas sensor: A density functional theory study. *Sensors and Actuators B: Chemical*, 263:502–507, 2018.

[18] Zhi Guo, Ningbo Liao, Miao Zhang, and Aixin Feng. Enhanced gas sensing performance of polyaniline incorporated with graphene: A first-principles study. *Physics Letters A*, 383(23):2751–2754, 2019.

[19] Lianjia Zhao, Kang Wang, Wei Wei, Lili Wang, and Wei Han. High-performance flexible sensing devices based on polyaniline/mxene nanocomposites. *InfoMat*, 1(3):407–416, 2019.

[20] Zengyuan Pang, Erol Yildirim, Melissa A. Pasquinelli, and Qufu Wei. Ammonia sensing performance of polyaniline-coated polyamide 6 nanofibers. *ACS Omega*, 6(13):8950–8957, 2021.

[21] Anja Korent, Kristina Žagar Soderžnik, Sašo Šturm, Kristina Žužek Rožman, Nathalie Redon, Jean-Luc Wojkiewicz, and Caroline Duc. Facile fabrication of an ammonia-gas sensor using electrochemically synthesised polyaniline on commercial screen-printed three-electrode systems. *Sensors*, 21(1), 2021.

[22] Jinmei Liu, Nuangyang Cui, Qi Xu, Zheng Wang, Long Gu, and Wei Dou. High-performance pani-based ammonia gas sensor promoted by surface nanostructuralization. *ECS Journal of Solid State Science and Technology*, 10(2):027007, 2021.

[23] Kevin M. Scotland, Oliver K.L. Strong, J. Mark Parnis, and Andrew J. Vreugdenhil. Dft modeling of polyaniline: a computational investigation into the structure and band gap of polyaniline. *Canadian Journal of Chemistry*, 100(2):162–167, 2022.

[24] Sukanya Das, Niharika Kashyap, Sangeeta Kalita, Debanga Bhusan Bora, and Ruli Borah. Chapter one - a brief insight into the physicochemical properties of room-temperature acidic ionic liquids and their catalytic applications in cc bond formation reactions. volume 54 of *Advances in Physical Organic Chemistry*, pages 1–98. Academic Press, 2020.

[25] Gabriel P. Oliveira, Bruno H. Barboza, and Augusto Batagin-Neto. Polyaniline-based gas sensors: Dft study on the effect of side groups. *Computational and Theoretical Chemistry*, 1207:113526, 2022.

[26] Hemalatha Parangusan, Jolly Bhadra, Razen Amer Al-Qudah, Elhassen Cheikh Elhadrami, and Noora Jabor Al-Thani. Comparative study on gas-sensing properties of 2d (mos2, ws2)/pani nanocomposites-based sensor. *Nanomaterials*, 12(24), 2022.

[27] Chonghui Zhu, Tingting Zhou, Hong Xia, and Tong Zhang. Flexible room-temperature ammonia gas sensors based on pani-mwcnts/pdms film for breathing analysis and food safety. *Nanomaterials*, 13(7), 2023.

[28] Hasanuddin, N.H., Wahid, M.H.A., Shahimin, M.M., Hambali, N.A.M.A., Nazir, N.S., Khairuddin, N.Z., Ramli, M.M., and Isa, S.S.M. Design and development of zno based gas sensor for fruit ripening detection. *MATEC Web Conf.*, 78:01109, 2016.

[29] K Arun, MS Lekshmi, and KJ Suja. Design and simulation of zno based acetone gas sensor using comsol multiphysics. In *2020 7th International Conference on Signal Processing and Integrated Networks (SPIN)*, pages 659–662. IEEE, 2020.

[30] Roniyus Marjunus, Daffa Cedri Kekalenteu, Agus Riyanto, and Wahyu Widanarto. Simulation of no2 work function-based sensor signal on zno. In *Journal of Physics: Conference Series*, volume 1751, page 012078. IOP Publishing, 2021.

[31] Artem Chizhov, Pavel Kutukov, Alexander Gulin, Artyom Astafiev, and Marina Rumyantseva. Uv-activated no2 gas sensing by nanocrystalline zno: Mechanistic insights from mass spectrometry investigations. *Chemosensors*, 10(4), 2022.

[32] Grazia Lo Sciuto, Piotr Kałużyński, and Salvatore Coco. 3d finite element simulation model of a chemiresistor gas sensor based on zno and graft comb copolymer integrated in a gas chamber. *Journal of Materials Science: Materials in Electronics*, 33(8):5037–5048, 2022.

[33] Rafaela S. Andre, Flávio M. Shimizu, Celina M. Miyazaki, Antonio Riul, Danilo Manzani, Sidney J.L. Ribeiro, Osvaldo N. Oliveira, Luiz H.C. Mattoso, and Daniel S. Correa. Hybrid layer-by-layer (lbl) films of polyaniline, graphene oxide and zinc oxide to detect ammonia. *Sensors and Actuators B: Chemical*, 238:795–801, 2017.

[34] Quantumatk. https://www.synopsys.com/silicon/quantumatk.html.

[35] Quantum dot, 2018. https://nanohub.org/resources/qdot/about.

[36] Quantum espresso, v6.4.1. http://www.quantum-espresso.org.

[37] Nemo5. https://engineering.purdue.edu/gekcogrp/software-projects/nemo5.

[38] Siesta 4.0. http://www.icmab.es/siesta.

[39] Vasp. http://www.vasp.at.

[40] Yasara. http://www.yasara.org.

[41] K. Stokbro, D.E. Petersen, S. Smidstrup, A. Blom, M. Ipsen, and K. Kaasbjerg. Semiempirical model for nanoscale device simulations. *Physical Review B Condensed Matter*, 82:075420, 2010.

[42] M. Brandbyge, J.L. Mozos, P. Ordejon, J.P. Taylor, and K. Stokbro. Density-functional method for nonequilibrium electron transport. *Physical Review B Condensed Matter*, 65:165401–165418, 2002.

[43] Dongwook Kwak, Yu Lei, and Radenka Maric. Ammonia gas sensors: A comprehensive review. *Talanta*, 204:713–730, 2019.

[44] Xunbo Hu, Mei Wang, Jianfeng Deng, Syed ul Hasnain Bakhtiar, Zhiping Zheng, Wei Luo, Wen Dong, and Qiuyun Fu. Sensing properties and mechanism of gas sensors based on zinc oxide quantum dots. *IEEE Sensors Journal*, 21(18):19722–19730, 2021.

[45] M.A. Chougule, Shashwati Sen, and V.B. Patil. Fabrication of nanostructured zno thin film sensor for no2 monitoring. *Ceramics International*, 38(4):2685–2692, 2012.

[46] S. V. Morozov, K. S. Novoselov, M. I. Katsnelson, F. Schedin, D. C. Elias, J. A. Jaszczak, and A. K. Geim. Giant intrinsic carrier mobilities in graphene and its bilayer. *Phys. Rev. Lett.*, 100:016602, Jan 2008.

[47] C. Lee, X. Wei, J.W. Kysar, and J. Hone. Measurement of the elastic properties and intrinsic strength of monolayer graphene. *Science*, 321:385–388, 2008.

[48] X. Tang, M. Debliquy, D. Lahem, Y. Yan, and J.P. Raskin. A review on functionalized graphene sensors for detection of ammonia. *Sensors*, 21:1443, 2021.

[49] Giuseppe Luongo, Antonio Di Bartolomeo, Filippo Giubileo, Carlos Alvarado Chavarin, and Christian Wenger. Electronic properties of graphene/p-silicon schottky junction. *Journal of Physics D: Applied Physics*, 51(25):255305, jun 2018.

[50] F. Schedin, A. K. Geim, S. V. Morozov, E. W. Hill, P. Blake, M. I. Katsnelson, and K. S. Novoselov. Detection of individual gas molecules adsorbed on graphene. *Natural Materials*, 6:1476–4660, 2007.

[51] Hui-Fen Zhang, Dong-Ping Wu, and Xi-Jing Ning. Atomistic mechanism for graphene based gaseous sensor working. *Applied Surface Science*, 470:448–453, 2019.

[52] Filiberto Ricciardella, Sten Vollebregt, Tiziana Polichetti, Mario Miscuglio, Brigida Alfano, Maria L. Miglietta, Ettore Massera, Girolamo Di Francia, and Pasqualina M. Sarro. Effects of graphene defects on gas sensing properties towards no2 detection. *Nanoscale*, 9:6085–6093, 2017.

[53] H.D. Tran, D. Li, and R.B. Kaner. One-dimensional conducting polymer nanostructures: Bulk synthesis and applications. *Advanced Materials*, 21:1487–1499, 2009.

[54] C. Nylabder, M. Armgrath, and I. Lundstrom. An ammonia detector based on conducting polymers. In *Proc. Int. Meeting on Chemical Sensors*, page 203–207, Fukuota, Japan, 1983.

[55] V.V Chabukswar, Sushama Pethkar, and Anjali A Athawale. Acrylic acid doped polyaniline as an ammonia sensor. *Sensors and Actuators B: Chemical*, 77(3):657–663, 2001.

[56] Ningning Song, Wucong Wang, Yue Wu, Ding Xiao, and Yaping Zhao. Fabrication of highly ordered polyaniline nanocone on pristine graphene for high-performance supercapacitor electrodes. *Journal of Physics and Chemistry of Solids*, 115:148–155, 2018.

[57] Michael Smirnov, Vitaly Vorobiov, Igor Kasatkin, Elena Vlasova, Maria Sokolova, and Natalia Bobrova. Long-term electrochemical stability of polyaniline- and polypyrrole-based hydrogels. *Chemical Papers*, 75, 02 2021.

[58] Meng Yang, Xianfa Zhang, Chuanyu Guo, Xiaoli Cheng, Chonghui Zhu, Yingming Xu, Zoltán Major, and Lihua Huo. Resistive room temperature dma gas sensor based on the forest-like unusual n-type pani/tio2 nanocomposites. *Sensors and Actuators B: Chemical*, 342:130067, 2021.

[59] Dongzhi Zhang, Zhenling Wu, and Xiaoqi Zong. Metal-organic frameworks-derived zinc oxide nanopolyhedra/s, n: graphene quantum dots/polyaniline ternary nanohybrid for high-performance acetone sensing. *Sensors and Actuators B: Chemical*, 2019.

[60] Dongzhi Zhang, Zhenling Wu, and Xiaoqi Zong. Flexible and highly sensitive h2s gas sensor based on in-situ polymerized sno2/rgo/pani ternary nanocomposite with application in halitosis diagnosis. *Sensors and Actuators B: Chemical*, 289:32–41, 2019.

[61] N.R. Tanguy, M. Thompson, and N. Yan. A review on advances in application of polyaniline for ammonia detection. *Sensors and Actuators B: Chemical*, 257:1044–1064, 2017.

[62] C. Aleman, C.A. Ferreira, J.Torras, A. Meneguzzi, M. Canales, M.A.S. Rodrigues, and J.Casanovas. On the molecular properties of polyaniline: A comprehensive theoretical study. *Polymer*, 49:5169–5176, 2008.

[63] W. S. Huang, B. D. Humphrey, and A. G. MacDiarmid. Polyaniline, a novel conducting polymer. morphology and chemistry of its oxidation and reduction in aqueous electrolytes. *Journal of the Chemical Society, Faraday Transactions 1: Physical Chemistry in Condensed Phases*, 82(8):2385–2400, 1986.

[64] S. Mandal, S. Kumar Saha, and P. Chowdhury. Synthesis and characterization of polyaniline based materials: their biological relevance - an overview. *International Journal of Current Microbiology and Applied Sciences*, 6:2309–2321, 2017.

[65] Z. Guo, N. Liao, M. Zhang, and W. Xue. Theoretical approach to evaluate graphene/pani composite as highly selective ammonia sensor. *Applied Surface Science*, 453(Suppl. S3):336 – 340, 2018.

[66] N.R. Tanguy, M. Thompson, and N. Yan. A review on advances in application of polyaniline for ammonia detection. *Sensors and Actuators B: Chemical*, 257:1044 – 1064, 2018.

[67] Lalit Kumar, Ishpal Rawal, Amarjeet Kaur, and S. Annapoorni. Flexible room temperature ammonia sensor based on polyaniline. *Sensors and Actuators B: Chemical*, 240:408–416, 2017.

[68] J. Kroutil, A. Laposa, J. Voves, M. Davydova, J. Nahlik, P. Kulha, and M. Husak. Performance evaluation of low-cost flexible gas sensor array with nanocomposite polyaniline films. *IEEE Sensors Journal*, 18:3759–3766, 2018.

[69] J. Romanova, J. Petrova, A. Ivanova, A. Tadjer, and N. Gospodinova. Theoretical study on the emeraldine salt – impact of the computational protocol. *Journal of Molecular Structure: THEOCHEM*, 954:36 – 44, 2010.

[70] A.S. Reis, E.A. Sanches, and H.O. Frota. Energy band structure and electronic transport properties of chlorine-doped polyaniline from ab initio calculations. *Chem. Rev. (Washington, DC, U. S.)*, 231:89 – 94, 2017.

[71] G. Zwicker and K. Jacobi. Experimental band structure of zno. *Solid State Communications*, 54(8):701–704, 1985.

[72] A. R. H. Preston, B. J. Ruck, L. F. J. Piper, A. DeMasi, K. E. Smith, A. Schleife, F. Fuchs, F. Bechstedt, J. Chai, and S. M. Durbin. Band structure of zno from resonant x-ray emission spectroscopy. *Phys. Rev. B*, 78:155114, Oct 2008.

[73] Rajbanul Akhond and Ahmed Sharif. Role of hydrogen co-doping on opto-electronic behaviors of na-h co-doped zinc oxide: A first principle study. *Journal of Physics Communications*, 4, 11 2020.

[74] Kristin Persson. Materials data on zno (sg:186) by materials project, 11 2014.

[75] M. C. Payne, M. P. Teter, D. C. Allan, T. A. Arias, and J. D. Joannopoulos. Iterative minimization techniques for ab initio total-energy calculations: Molecular dynamics and conjugate gradients. *Reviews of Modern Physics*, 64(4):1045–1097, 1992.

[76] Kausar Harun, Nor Azmira Salleh, Bahri Deghfel, Muhamad Kamil Yaakob, and Ahmad Azmin Mohamad. Dft + u calculations for electronic, structural, and optical properties of zno wurtzite structure: A review. *Results in Physics*, 16:102829, 2020.

[77] Jorlandio Felix, F. Eronides, Elder De Vasconcelos, and Walter De Azevedo. Tailoring the electrical properties of zno/polyaniline heterostructures for device applications. *Journal of the Korean Physical Society*, 58:1256, 05 2011.

[78] Aleksander Recnik, S. Bernik, and Nina Daneu. Microstructural engineering of zno-based varistor ceramics. *Journal of Materials Science*, 47:1655–1668, 02 2012.

[79] G.S.Trivikrama Rao and D Tarakarama Rao. Gas sensitivity of zno based thick film sensor to nh3 at room temperature. *Sensors and Actuators B: Chemical*, 55(2):166–169, 1999.

[80] Ulf Seifert. *Oberflächenmodifizierung keramischer Werkstoffe mittels Laserstrahlung*. PhD thesis, Ingeneurhochschule Mittweida, 1989.

[81] A. Posta, J. Nahlik, A. Laposa, and J. Voves. Flexible ammonia gas sensor based on polyaniline. In *Proc. of 1Oth International Conference on Nanomaterials - Research & Application*, Nanocon 2018, pages 272–275, Brno, Czech Republic, 2018.

[82] Hana Šustková, Alexandr Pošta, and Jan Voves. Polyaniline emeraldine salt as an ammonia gas sensor - comparison of quantum-based simulation with experiment. *Physica E: Low-dimensional Systems and Nanostructures*, 114:113621, 2019.

[83] Hana Šustková and Jan Voves. Modeling a multiple-chain emeraldine gas sensor for NH_3 and NO_2 detection. *Beilstein J. Nanotechnol.*, 13:721–729, 2022.

List of Author´s Publications

Journals (Impact)

[A]. Hana Šustková, Alexandr Pošta, and Jan Voves. Polyaniline emeraldine salt as an ammonia gas sensor - comparison of quantum-based simulation with experiment. *Physica E: Low-dimensional Systems and Nanostructures*, 114:113621, 2019

The paper has been cited in:

- Ehab E. Khozemey, Mohamed M. Ghobashy, and Tarek M. Mohamed. Radiation synthesis of gas sensor based on polyaniline nanoflake-poly vinyl alcohol film for four hazardous gases (nh3, co2, h2s and phenol). *Arab Journal of Nuclear Sciences and Applications*, 53(3):210 – 221, 2020
- E. D. Roida and N. P. Putri. Aplikasi polianilin sebagai bahan aktif pendeteski alkohol. *Jurnal Inovasi Fisika Indonesia*, 6(2), 2020
- M. Sh Zoromba, M.H. Abdel-Aziz, M. Bassyouni, Abdullah M. Abusorrah, A. At- tar, Neazar Baghdadi, and Numan Salah. Polypyrrole sheets composed of nanopar- ticles as a promising room temperature thermo-electric material. *Physica E: Low- dimensional Systems and Nanostructures*, 134:114889, 2021
- S. Kamarudin, Z.A.A. Rahman, and M.S.A. et al. Rani. Acrylic acid-grafted polyaniline fibers for nickel ion removal from water: synthesis, characterization and adsorption kinetics. *Polymer Bulletin*, 2022
- D. S. Upadhye, A. S. Dive, R. B. Birajadar, S. B. Bagul, K. P. Gattu, and R. Sharma. Low-concentration ammonia gas sensing using polyaniline nanofiber thin film grown by rapid polymerization technique. *Journal of Materials Science: Materials in Electronics*, 2022
- Xuerui Wan, Hairong Dai, Huayin Zhang, Huan Yang, Feng Li, and Qian Xu. Emerald-based polyaniline-modified polyacrylonitrile nanofiber mats based solid-phase extraction for efficient and simple detection of sudan dyes in poultry feed. *Microchemical Journal*, 181:107824, 2022

[B]. Hana Šustková and Jan Voves. Modeling a multiple-chain emeraldine gas sensor for N H3 and N O2 detection. *Beilstein J. Nanotechnol.*, 13:721–729, 2022

The paper has been cited in:

- M. Oliveira, A. Melo, K. Abreu, Marilia M. Oliveira, R. Furtado, A. Biswas, H. Cheng, P. Gonzalez, and C. Alves. Polyaniline/cashew gum composite electrosynthesized on gold surface in aqueous acid medium for ammonia colorimetric detection. *Journal of the electrochemical society*, 170(6), June 1 2023

[C]. Hana Šustková and Jan Voves. Effect of HCl and H2 SO4 dilutant on emeraldine gas sensor for ammonia - numerical model. *IEEE Sens. Lett.*, pages 1–4, 2022

Conferences

[D]. Hana Šustková. Polyaniline electric conductivity in the presence of ammonia molecules. In *22nd International Student Conference on Electrical Engineering Poster 2019*, Praha 2019. České vysoké učení technické v Praze, Fakulta elektrotechnická

Other candidate's works

Conferences

[E]. Hana Šustková and Jan Jan Voves. Analysis of finfet characteristics with gate length scalling. In *NANOCON 2014, 6th international conference*, pages 814 – 819, Ostrava, CZ, 2015. Technická universita Ostrava - Vysoká škola báňská

The paper has been cited in:

- Sudhansu Mohan Biswal, Biswajit Baral, Debashis De, and Angsuman Sarkar. Study of effect of gate-length downscaling on the analog/rf performance and linearity investigation of inas-based nanowire tunnel fet. *Superlattices and Microstructures*, 91:319–330, 2016
- Chetan Chugh. The effects of variation in geometry parameters on sub-50 nm finfet and their direct impact on finfet performance. In *2018 International Conference on Intelligent Circuits and Systems (ICICS)*, pages 177–183, 2018

[F]. Hana Šustková. Home lighting approaching sunlight daily variations for greater home comfort and work performance. In *Proceedings of 3rd Conference on Innovations in Assistive Technologies and Health Care*, Praha, CZ, 2014. České vysoké učení technické v Praze, Fakulta elektrotechnická

Applied results

[G]. Ulf Seifert and Hana Šustková. Einsatz von mikrocontrollern in der leistungelektronik. In *Scientific Reports*, volume 3 of IWKM, Mittweida, 2014. Hochschule Mittweida, University of Applied Sciences

List of Figures

List of Tables

List of Abbreviations

+U	plus potential
1BZ	1st Brillouin zone
2D	two-dimensional
3D	three-dimensional
ABINIT	software suite to calculate properties of materials
ACFDT	adiabatic-connection-fluctuation-dissipation theorem
AM1	Austin Model 1
AM1BCC	Austin Model 1 bond charge corrections
Au	gold
AutoSMILES	automatic Simplified molecular-input line-entry system
CGA	conjugated gradient approximation
CO	carbon monoxide
CPU	central processing unit
DFT	Density Functional Theory
DOS	density of states
EMT	Effective Medium Theory
FET	field effect transistor
FFT	Fast Fourier Transform
FHi	Trouiller–Martins type pseudopotential
FIRE	Fast Inertial Relaxation Engine
GGA	generalized gradient approximation
GPU	graphics processor unit
GUI	graphical user interface
GW	single particle Green's function G, screened Coulomb interaction W
H_2SO_4	sulfuric acid
HCl	hydrochloric acid
HF	hybrid functional
I-V	current - voltage
LCAO	local atomic orbital
LDA	local density approximation
LDOS	local density of states
LSD	local spin density
MKL	Math Kernel Library
MNDO	Modified Neglect of Diatomic Overlap
MOPAC	Molecular Orbital PACkage
MPI	Message Passing Interface
MPICH	implementation of Message Passing Interface
MPSH	molecular projected self-consistent Hamiltonian
MXenes	metal carbides and nitrides
nanoHUB	science and engineering gateway
NEB	nudged elastic bands
NEGF	non-equilibrium Green's function
NEMO	NanoElectronics MOdelling Tools
NH_3	ammonia
NMR	nuclear magnetic resonance
NO_2	nitrogen dioxide
OpenMP	Open Multi-Processing

PANI	polyaniline
PAW	Projector Augmented Waves
PA6	polyamid 6
PBE	Perdew-Burke-Ernzerhof
PM3	parametric method
PME	Particle Mesh Ewald
ppb	particle per billion
ppm	particle per million
QDL	Quantum Dot Lab
QE	Quantum Espresso
R	electrical resistance of target material
R_0	electrical resistance of pure material
RDF	radial distribution function
Res	relative resistance change
RMSD	Root-mean-square deviation of atomic positions
RMSF	Root-mean-square fluctuation of atomic positions
SEM	scanning electron microscope
SIESTA	Spanish Initiative for Electronic Simulations with Thousand of Atoms
SMO	semiconducting metal oxide
SPE	screen-printed electrodes
TD	time-dependent
TMD	two-dimensional transition-metal dichalcogenide
UV	ultra violet
VASP	Vienna Ab initio Simulation Package
VdW	Van der Waals
VNL	Virtual NanoLab
W	width
YASARA	Yet Another Scientific Artificial Reality Application
ZnO	zinc oxide